12-1-2014

Spectroscopic Investigation of the Chemical and Electronic Properties of Chalcogenide Materials for Thin-film Optoelectronic Devices

Kimberly Horsley
University of Nevada, Las Vegas, horsley.kim@gmail.com

SPECTROSCOPIC INVESTIGATION OF THE CHEMICAL AND ELECTRONIC PROPERTIES OF CHALCOGENIDE MATERIALS FOR THIN-FILM OPTOELECTRONIC DEVICES

by

Kimberly Anne Horsley

Bachelor of Science – Biology
University of Nevada, Las Vegas
2009

Bachelor of Arts – Chemistry
University of Nevada, Las Vegas
2009

A dissertation submitted in partial fulfillment
of the requirements for the

Doctor of Philosophy – Chemistry

Department of Chemistry
College of Sciences
The Graduate College

University of Nevada, Las Vegas
December 2014

UNLV | GRADUATE COLLEGE

We recommend the dissertation prepared under our supervision by

Kimberly Anne Horsley

entitled

Spectroscopic Investigation of the Chemical and Electronic Properties of Chalcogenide Materials for Thin-Film Optoelectronic Devices

is approved in partial fulfillment of the requirements for the degree of

Doctor of Philosophy - Chemistry

Department of Chemistry

Clemens Heske, Ph.D., Committee Chair

Kathleen Robins, Ph.D., Committee Member

Dong-Chan Lee, Ph.D., Committee Member

Rama Venkat, Ph.D., Graduate College Representative

Kathryn Hausbeck Korgan, Ph.D., Interim Dean of the Graduate College

December 2014

ABSTRACT

Spectroscopic Investigation of the Chemical and Electronic Properties of Chalcogenide Materials for Thin-Film Optoelectronic Devices

by

Kimberly Anne Horsley

Dr. Clemens Heske, Examination Committee Chair
Professor of Chemistry
University of Nevada, Las Vegas

Chalcogen-based materials are at the forefront of technologies for sustainable energy production. This progress has come only from decades of research, and further investigation is needed to continue improvement of these materials.

For this dissertation, a number of chalcogenide systems were studied, which have applications in optoelectronic devices such as LEDs and Photovoltaics. The systems studied include $Cu(In,Ga)Se_2$ (CIGSe) and $CuInSe_2$ (CISe) thin-film absorbers, CdTe-based photovoltaic structures, and CdTe-ZnO nanocomposite materials. For each project, a sample set was prepared through collaboration with outside institutions, and a suite of spectroscopy techniques was employed to answer specific questions about the system. These techniques enabled the investigation of the chemical and electronic structure of the materials, both at the surface and towards the bulk.

$CdS/Cu(In,Ga)Se_2$ thin-films produced from the roll-to-roll, ambient pressure, Nanosolar industrial line were studied. While record-breaking efficiency cells are usually prepared in high-vacuum (HV) or ultra-high vacuum (UHV) environments, these samples demonstrate competitive mass-production efficiency without the high-cost deposition environment. We found relatively low levels of C contaminants, limited Na and Se

oxidation, and a S-Se intermixing at the CdS/CIGSe interface. The surface band gap compared closely to previously investigated CIGSe thin-films deposited under vacuum, illustrating that roll-to-roll processing is a promising and less-expensive alternative for solar cell production.

An alternative deposition process for $CuInSe_2$ was also studied, in collaboration with the University of Luxembourg. $CuInSe_2$ absorbers were prepared with varying Cu content and surface treatments to investigate the potential to produce an absorber with a Cu-rich bulk and Cu-poor surface. This is desired to combine the bulk characteristics of reduced defects and larger grains in Cu-rich films, while maintaining a wide surface band gap, as seen in Cu-poor films. A novel absorber was prepared Cu-rich with a final In-Se treatment to produce a Cu-poor surface, and compared directly to Cu-poor and Cu-rich produced samples. Despite reduced Cu at the surface, the novel absorber was found to have a surface band gap similar to that of traditional, Cu-poor grown absorbers. Furthermore, estimation of the near-surface bulk band gap suggests a narrowing of the band gap away from the surface, similar to highly efficient, Cu-poor grown absorbers.

Long-term degradation is another concern facing solar cells, as heat and moistures stress can result in reduced efficiencies over time. The interface of the back contact material and absorber layer in (Au/Cu)/CdTe/CdS thin-film structures from the University of Toledo were investigated after a variety of accelerated stress treatments with the aim of further understanding the chemical and/or electronic degradation of this interface. Sulfur migration to the back contact was observed, along with the formation of Au-S and Cu-S bonds. A correlation between heat stress under illumination and the formation of Cu-Cl bonds was also found.

Nanocomposite materials hold promise as a next-generation photovoltaic material and for use in LED devices, due in part to the unique ability to tune the absorption edge of the film by adjusting the semiconductor particle size, and the prospective for long-range charge-carrier (exciton) transport through the wide band gap matrix material. Thin films of CdTe were sputter deposited onto ZnO substrates at the University of Arizona and studied before and after a short, high temperature annealing to further understand the effects of annealing on the CdTe/ZnO interface. A clumping of the CdTe layer and the formation of Cd- and Te-oxides was observed using surface microscopy and photoelectron spectroscopy techniques. These findings help to evaluate post-deposition annealing as a treatment to adjust the final crystallinity and optoelectronic properties of these films.

Through publication and/or discussion with collaborators, each project presented in this dissertation contributed to the understanding of the chemical and electronic properties of the material surface, near-surface bulk, and/or interfaces formed. The information gained on these unique chalcogenide materials will assist in designing more efficient and successful optoelectronic devices for the next generation of solar cells and LEDs.

ACKNOWLEDGEMENTS

While my graduate studies involved a significant amount of UHV work, the overarching education, research, data acquisition, and analysis was not done in a vacuum! I am strongly indebted to many people for their knowledge, support, and assistance:

- **The original and only Herr Vater Professor, Dr. Clemens Heske.** Thank you for accepting me into your science family! Thank you for insisting (and persisting) on quality and greatness in my professional endeavors, while exuding patience and genuine care for my progress and wellbeing.

- **Step-Herr Vater Professors, Marcus Bär and Lothar Weinhardt.** Thank you for your insights, your high-pace energy, and the limitless stream of quality papers! Marcus, thank you especially for hosting me at the HZB, and not being (too) upset when the sputter gun died the third time (it wasn't my fault!!!).

- **Dr. Moni Blum** is recognized here for her patience, knowledge, and expertise, and for setting a superb example of what a postdoc and leader should be. And, of course, for being an amazing cook! Thank you!

- **Members of the Heske Group past:** Drs. Timo Hofmann, Stefan Krause, Yufeng Zhang, Sujitra Pookpanratana, and Mr. Kyle George - thank you for introducing me to the Heske lab and the world of spectroscopy, and your patience as you taught me your ways. A special thanks to Stefan for not allowing me to go homeless in Berlin! Thank you also to Dr. Michael Weir, and our talented undergraduates Michael Folse, Sarah Alexander, Yu Liu, and Ryan Bugni.

- **Members of the Heske Group present:** Doug Hanks, Michelle Mezher, Lynette Kogler, Dr. Marc Häming, Dr. Samantha Rosenberg, and Manuela Wallesch. Thank you for your assistance and companionship both in the laboratory and out, and the occasional mental imagery of lab unicorns, intent on derailing our best research efforts (the war continues!).

- **Berlin group members:** Dr. Regan Wilks, Dr. Dominic Gerlach, and Dr. (or soon-to-be) Roberto Felix-Duarte. I am grateful for the experience of learning a new UHV system, your insight with data acquisition and analysis both at the HZB and at the beamline, and for helping me to navigate my way around Berlin.

- **Collaborators**: I am immensely indebted to my external collaborators, without which I would have had no samples to measure, and with which I had many meaningful

exchanges. At Nanosolar, thank you to Drs. David Jackrel and Jeroen Van Duren. Thank you to Prof. Susanne Siebentritt and Dr. Valérie Depredurand at the University of Luxembourg. Thank you to Prof. Alvin Compaan and Dr. Naba Paudel at the University of Toledo, Ohio. And thank you to Prof. B. G. Potter, Jr., and Dr. Russell Beal at the University of Arizona.

- **My family:** recognized for their unconditional and never-ending love and support; my mother, Gayle Horsley, thank you for listening to me and comforting me in my most stressful times, and for making an honest effort to understand what I do at work. My father, Dr. George Horsley, thank you for frequently offering your time and resources, and providing thoughtful discussion on topics outside the world of physical chemistry. My sister, Dr. Jennifer Horsley, thank you for being my competition, my best friend, and in times of trial, my collaborator and partner. Finally, my brother-in-law, Richard Silva, thank you for showing me a good work ethic, and being a fantastic big brother.

- **Nesley Orochena,** thank you for your support, love, and companionship, and for putting up with my often trying work schedule and weekend-long measurement campaigns. I am thankful for our intellectual discussions, your insight in realms both scientific and not, and, of course, your occasional help with math. ☺

DEDICATION

To current and future students and intellectuals in the spectroscopy community, and to the passing of knowledge between generations.

What would you do if you weren't afraid? – Sheryl Sandberg

TABLE OF CONTENTS

LIST OF TABLES

LIST OF FIGURES

CHAPTER 1

INTRODUCTION

1.1 Motivation

The discovery of the photoelectric effect in 1839 was the first step towards the production of photovoltaic (PV) devices.[1] The first PV devices to demonstrate significant efficiency were produced in the 1950s using a silicon-based p-n junction as the photon-absorbing material.[2] These first generation solar cells quickly reached efficiencies of over 10%, and were followed shortly by reports of chalcogenide-based devices, which used sulfur-, selenium-, or tellurium-containing compounds for the absorber material. Cadmium telluride (CdTe) solar cells were first demonstrated in the late 1950s,[3] and chalcopyrite-based solar cells derived from $CuInSe_2$ (CISe) compounds followed in the mid-1970s.[4] Chalcogenide-based PV devices, however, lagged behind Si in production for many years, in part due to their lower efficiencies and the less abundant materials used (thus higher costs). Continued research over the last decade has seen thin-film chalcogenide efficiencies greatly improved, and in the last year, match that of multi-crystalline and thin-film silicon. Current laboratory-cell record efficiencies are 21.7 % for thin-film $Cu(In,Ga)Se_2$,[5] and 21.0 % for thin-film CdTe.[6]

While efficiencies have been steadily increasing, thin-film devices are yet to reach the theoretical efficiency limit. The Shockley-Queisser model devised in 1961 predicts the efficiency limit for a single p-n junction solar cell to be ~ 30%.[7] This limit is in part due to the fact that only photons of energy equal to or greater than the band gap are absorbed. Lower energy photons do not produce electron-hole pairs, and higher energy photons are excited beyond the conduction band minimum (CBM), so that only a portion

of their energy is converted to electricity. With laboratory-based cells around 20% efficient, and full solar cell modules reliably reaching efficiencies of ~ 13-17%,[8] there is still much space for continued improvement of single-junction devices. Further, there are a number of ways to achieve efficiencies beyond the theoretical limit described by Shockley-Queisser through non-conventional junctions. These include tandem solar cells, which employ multiple p-n junctions with varying band gaps to absorb a wider range of energies from the solar spectrum, and intermediate-band solar cells, which have delocalized radiative recombination centers located within the band gap that allows for absorption of photon energies less than the band gap. Nanostructures have also been studied for their potential incorporation into PV devices; they have been placed at interfaces to increase surface area, or within films to scatter light.[9] Varying the size of the nanostructures also allows for tuning of the band gap due to quantum effects, and a variety of particle sizes embedded in the material would theoretically allow for a wider range of photon energies to be absorbed. These "third generation" solar cells may be able to reach efficiencies well above that of single junction devices – for example, a theoretical efficiency as high as 68.5% for a multi-junction cell has been calculated.[9,10]

Efficiency is also not the only route for improvement of photovoltaic devices. Improvements are also desired that reduce the initial costs involved in device production, and that maintain the device efficiencies over a longer lifetime. Many factors play into the production costs of solar cells, such as raw materials, equipment, energy input, and time. Production methods that require less expensive environments (e.g., ambient pressure or low temperature treatments), or use reduced amounts of raw materials or cheaper materials (e.g., thinner films, nanoparticles, more abundant elements), are

attractive due to their potential to reduce the final solar cell cost. Long-term device degradation is also a concern which plays into the full system cost, and further understanding of the degradation processes currently effecting solar cells will help to develop methods to combat them, such as adjusting the materials used, or new encapsulation techniques. Understanding and reducing solar cell degradation over time would extend the lifetime of devices, and result in higher conversion efficiencies years after installation.

1.2 Dissertation Structure

Each project encompassed in this dissertation investigates one of these potential areas for improvement in thin-film, chalcogenide-based optoelectronic devices. To lead into the material, Chapter 1 gives an introduction into the motivations for the research and organization of the dissertation. Chapter 2 provides relevant background information on the materials studied, and Chapter 3 provides a description of the measurement techniques used. Note that a separate reference list is give at the end of each chapter.

In Chapter 4, investigation of a $Cu(In,Ga)Se_2$ absorber and a $CdS/Cu(In,Ga)Se_2$ material stack taken from the Nanosolar, ambient-pressure, roll-to-roll industrial manufacturing process is presented. The samples are compared to high-efficiency CIGSe absorbers produced in-vacuum, to investigate the effects of the unique production method. This chapter also gives some overview of common characteristics of $Cu(In,Ga)Se_2$ absorber materials.

Chapter 5 continues the discussion of $Cu(In,Ga)Se_2$-based absorbers, by investigating an alternative deposition method currently being developed. The novel absorbers are grown with first a Cu-rich layer, followed by a separately deposited Cu-

poor surface layer. Here, it is hoped to combine the beneficial bulk characteristics of Cu-*rich* $CuInSe_2$ with the beneficial surface characteristics of Cu-*poor* $CuInSe_2$. The surface and near-surface bulk chemical and electronic properties are studied, and compared to two Cu-poor and Cu-rich absorbers, deposited by standard methods.

In Chapter 6 we transition to CdTe-based absorbers, to study the degradation mechanisms at play at the back contact/CdTe interface. A series of (Au/Cu)/CdTe/CdS stack samples were prepared, and underwent rapid thermal degradation treatment in a variety of ambient environments. Special attention is given to the chemical environment at the (Au/Cu)/CdTe back contact interface to investigate the chemical processes at play. Increased understanding of this interface and the degradation processes involved may help to direct adjustments in deposition parameters and/or materials used, in order to improve solar cell lifetimes.

Chapter 7 is associated with a next-generation optoelectronic device design, which utilizes CdTe/ZnO nanocomposite materials. Here, thin CdTe layers deposited on ZnO were investigated before and after an annealing treatment. The surface morphology and chemical composition are presented in detail, showing the effects of the annealing process on the CdTe/ZnO interface.

1.3 References

(1) Becquerel, A. E. *Comptes Rendus* **1839**, *9*, 561.

(2) Chapin, D. M.; Fuller, C. S.; Pearson, G. L. *J. Appl. Phys.* **1954**, *25*, 676–677.

(3) Goldstein, B. *Phys. Rev.* **1958**, *109*, 601–603.

(4) Shay, J. L.; Wagner, S.; Kasper, H. M. *Appl. Phys. Lett.* **1975**, *27*, 89–90.

(5) New efficient world record from exclusive research partner ZSW substantiates the technological advantage of CIGS thin film technology http://www.manz.com/investor-relations/publications/corporate-news/manz-ag-

neuer-wirkungsgrad-weltrekord-des-exklusiven-forschungspartners-zsw-untermauert-technologisc-570 (accessed Sep 25, 2014).

(6) First Solar builds the highest efficiency thin film PV cell on record http://investor.firstsolar.com/releasedetail.cfm?ReleaseID=864426 (accessed Aug 18, 2014).

(7) Shockley, W.; Queisser, H. J. *J. Appl. Phys.* **1961**, *32*, 510.

(8) Green, M. A.; Emery, K.; Hishikawa, Y.; Warta, W.; Dunlop, E. D. *Prog. Photovolt. Res. Appl.* **2014**, *22*, 701–710.

(9) Razykov, T. M.; Ferekides, C. S.; Morel, D.; Stefanakos, E.; Ullal, H. S.; Upadhyaya, H. M. *Sol. Energy* **2011**, *85*, 1580–1608.

(10) Tobías, I.; Luque, A. *Prog. Photovolt. Res. Appl.* **2002**, *10*, 323–329.

CHAPTER 2

LITERATURE OVERVIEW AND CURRENT STATUS

Chapter 2 discusses the basic structure of a thin-film solar cell, focusing on the p-n junction and the semiconductor-to-metal interface. This is followed by more detailed discussion of $Cu(In,Ga)Se_2$-based (hereafter referred to as CIGSe) and CdTe-based solar cells. The absorber deposition of CIGSe solar cells is discussed, followed by the role of Na, and S/Se intermixing at the CdS/CIGSe interface. For CdTe-based solar cells, the $CdCl_2$ treatment, S diffusion, and the role of Cu in the back contact formation is discussed, along with the methods for, and utility of, stress treatments. The chapter ends with a brief discussion of nanocomposite materials, starting with the quantum confinement effect, nanocomposite material structure, and the metal oxide/semiconductor interface.

2.1 Chalcogenide Solar Cell Structure

The materials structure for a CIGSe and CdTe thin-film solar cell (top) and energy band alignment of the p-n junction and semiconductor-to-metal interface (bottom) is shown in Fig. 2.1. CIGSe thin-film solar cells are grown in a substrate configuration (from right to left in Fig. 2.1) on a soda-lime glass substrate, while CdTe cells achieve their highest efficiencies when grown in the superstrate configuration (left to right).[1]

Both cell structures consist of a metal back contact, such as Cu and Au in CdTe-based solar cells or Mo in CIGSe-based solar cells. A p-type semiconductor layer follows, called the “absorber” layer (CdTe or CIGSe), where the majority of the photons

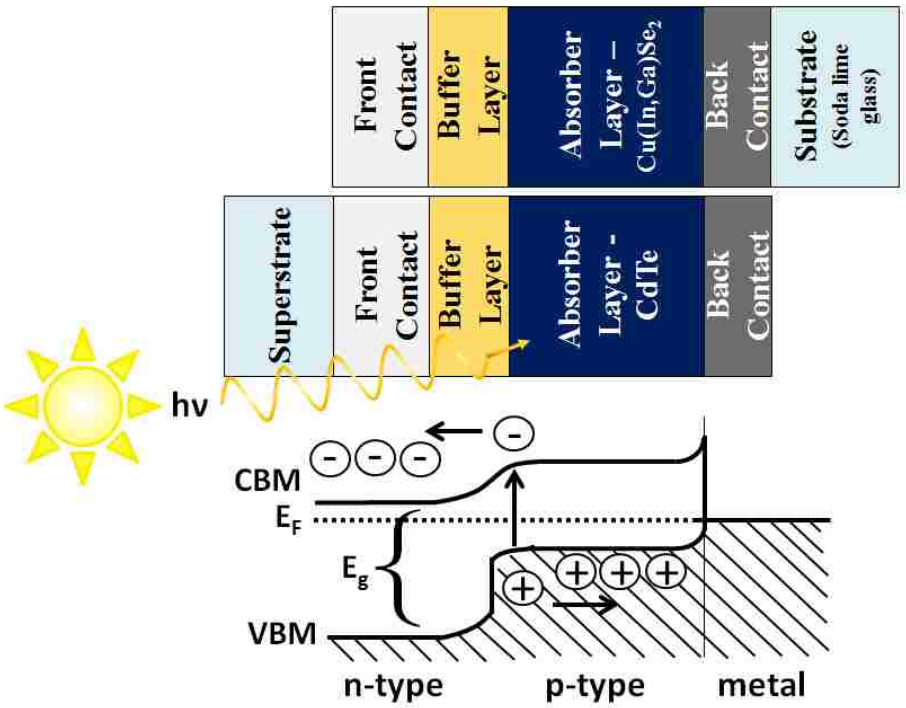

Fig. 2.1: General material structure (top) and band alignment of the p-n junction and semiconductor to metal interface (bottom) of a thin-film chalcogenide-based solar cell. Band diagram modeled after Ref. 3.

are absorbed to create electron-hole pairs. This is followed by the n-type "buffer" layer (generally CdS, also Zn(OH,S) or $In(OH,S)^2$), forming the other half of the p-n junction. The "front contact" follows, which generally consists of a transparent conductive oxide (TCO) such as ZnO, or SnO:F. The buffer layer, front contact, and superstrate (if present, usually glass) are wide band gap materials, designed to absorb a minimal amount of the solar spectrum.

Solar cells are diodes, built from the interface of a p-type and n-type material. An n-type material has electrons as the majority carrier, meaning a large number of electrons will be in the CB at room temperature due to the prevalence of donor dopant sites. Because of this, in an n-type material the Fermi Energy (E_F; at temperatures approaching

zero, E_F is the energy below which all states are filled, and above which all states are empty[3]) will be located closer to the conduction band minimum (CBM) than the valence band maximum (VBM), as shown on the left of the band diagram in Fig. 2.1. The inverse is correct for a p-type material shown in the center of the Fig. 2.1, in which holes (the absence of an electron) in the VB are the majority carriers due to a predominance of acceptor dopant sites. The p-n junction is shown here at equilibrium, as seen from the flat E_F across both materials. To reach equilibrium conditions, a diffusion of charge carriers occurs during interface formation. Recombination of the charge carriers creates a depletion region or space-charge region at the interface, which produces the band bending and built-in voltage at the p-n junction.[3]

2.2 The Semiconductor-to-Metal Interface

The semiconductor-to-metal interface on the right of the band diagram in Fig. 2.1 depicts an ohmic contact at equilibrium. The interface is ohmic if there is no barrier to majority charge carrier transport between the semiconductor and metal. Alternatively, a Schottky barrier, i.e., a barrier to charge transport, may form at the metal-semiconductor contact. The ideal metal-to-semiconductor interface is often modeled by the Schottky-Mott method, in which the work function of the metal (Φ_M) and the semiconductor (Φ_{SC}) determine the potential energy barrier, V_{bi}, (and by relation the presence or absence of a Schottky barrier) through equation 2.1:

$$V_{bi} = \Phi_M - \phi_{SC} \tag{2.1}$$

where V_{bi}, Φ_M and Φ_{SC} are shown in Fig.2.2.

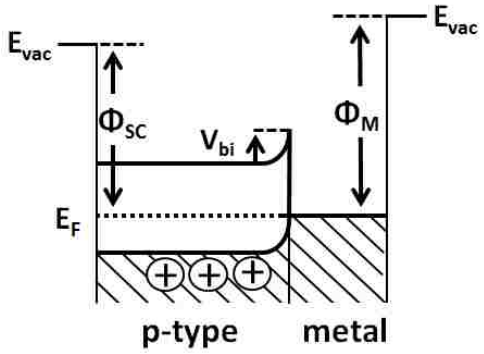

Fig. 2.2: Metal-semiconductor contact. An ohmic contact is depicted between a p-type semiconductor and a metal. Adapted from images in Ref. 3.

Based on this model, an ohmic contact is formed with a p-type semiconductor when $\Phi_M > \Phi_{SC}$, and a Schottky barrier will form if $\Phi_M < \Phi_{SC}$. Therefore, metals with high Φ_M values would be expected to form ohmic contacts to the p-type absorber layers, CdTe and CIGSe. While this model is a useful starting point to predict the characteristics of a metal-semiconductor contact, interface formation is a complex process, and this rule does not hold true for many materials and situations. This is, in part, because the model is based on work function values of the material, which 1) are surface properties, 2) will vary between samples of the same material based on the crystal surface orientation and impurities, and 3) do not exist at the interface, or in the bulk of the material. The work function is dependent on the surface dipole, which on interface formation is replaced by an (unknown) interface dipole. Further still, Fermi level pinning, in which a high dopant density saturates the effects of the metal at the very interface and prevents the expected band bending, may also produce "real-world" results different from those expected from the model. Thus, measurements of the true interface are needed to understand the metal-to-semiconductor interface, as well as other interfaces.

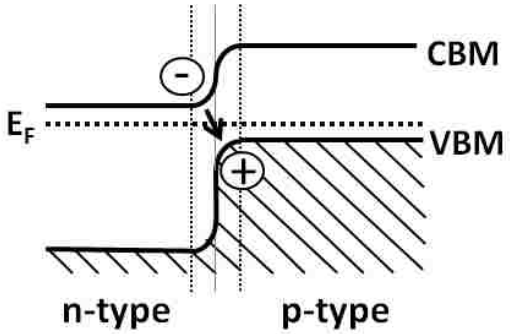

Fig. 2.3: A conceptual depiction of a p-n junction formed between two highly doped p- and n-type materials. The solid vertical line denotes the junction location, while the dashed vertical lines denote the depletion region to either side of the junction.

2.3 Charge Carrier Concentration and Recombination

Charge carrier concentration is the number of carrier atoms per unit volume, and describes the density of charges within the material. Carrier concentration plays an important role in interface formation. The width of the depletion region created at the p-n junction is directly affected by the density of charge carriers in each material.[3] This translates to the sloping of the bands at the interface, such that a shorter depletion width and thus steeper band bending occurs with a higher doping density.

The more abrupt band bending at the junction causes the CB of the n-type material to come into close proximity of the VB in the p-type material. This makes recombination, the relaxation of an excited electron in the CB into a hole in the VB, statistically more probable due to the close proximity of the charges. Fig. 2.3 depicts the band alignment for two highly doped p- and n-type materials, and recombination at the interface.

2.4 $Cu(In,Ga)Se_2$

The CIGSe section begins with a broad discussion of absorber deposition techniques, since Chapters 4 and 5 investigate two uniquely deposited absorbers. Some of the main

details of CIGSe-based absorbers follow, such as the role of Na and the presence of S/Se intermixing at the CdS/CIGSe interface.

2.4.1 CIGSe Absorber Deposition Methods

A number of techniques for deposition of the CIGSe absorber have been developed. In recent years, the most progress has been achieved with co-evaporation, sputtering, and non-vacuum "printing" with ink-based precursors.[4]

The most successful and thus most common method of CIGSe absorber deposition is co-evaporation, by which efficiencies of at least 20.5% have been achieved.[5] The NREL 3-stage co-evaporation process is most prevalent, the first variation of which was originally patented in 1995.[6,7] This absorber deposition consists of three stages, all of which are performed in a Se vapor environment. After the deposition chamber is pumped down (for example, to less than 3×10^{-6} torr[6]), In and/or Ga are evaporated along with Se onto the substrate, which is held around 400 °C. The Se evaporation is then continued as the substrate temperature is ramped up to near 600 °C for the second stage, when only Cu and Se are evaporated. In the third and final stage, the sample is kept near 600 °C while In and/or Ga are again deposited, in the absence of further Cu deposition.[8] By this method, a Cu-rich bulk stoichiometry (Cu > 25 at.%) is achieved after the Cu deposition, followed by a conversion to Cu-poor stoichiometry (Cu < 25 at.%) when the final In and/or Ga layer is deposited, providing that less than a stoichiometric amount of Cu was deposited in the second stage.[6] Cu-poor absorbers have previously yielded higher efficiencies compared to Cu-rich absorbers, with the record efficiencies all stemming from Cu-poor devices. This is predominantly due to the

beneficial electronic properties of the Cu-poor surface, which are not seen in Cu-rich films. A detailed discussion of these effects is presented in Chapter 5.

Non-vacuum, ink-based printing is an attractive deposition technique for solar cell production, due to the lower equipment costs and the ability to deposit rapidly on a moving substrate. The highest efficiency achieved with these deposition parameters is 17.1 %, as reported by Nanosolar in 2012.[9] Their manufacturing process included a number of novel techniques, such as a rapid, nanoparticle-ink printing of the absorber layer, depositing this absorber layer at ambient pressure, and depositing on a flexible foil substrate. This allowed for a roll-to-roll type production line for efficient and inexpensive manufacturing, the practicality of which was supported by the record efficiencies they achieved. Further discussion of their production method, and a detailed study of the CdS/CIGSe interface is presented in Chapter 4.

2.4.2 Sodium in CIGSe

CIGSe thin-film solar cells typically achieve their highest efficiency when grown in a substrate configuration (i.e., from right to left in Fig. 2.1).[1] When a soda-lime glass substrate is used, this growth configuration allows for Na migration from the glass, through the metal back contact, and into the CIGSe absorber layer during processing.[1] Sodium was realized to be beneficial in CIGSe thin-films as early as 1993, when the use of soda-lime glass was shown to improve cell efficiencies, possibly by increasing the grain sizes in the absorber layer, and resulted in a Na signal at the film surface.[10] Na has since been shown to reside predominantly at the surface and grain boundaries of the absorber layer.[11] A reduced but significant (and self-limiting[12]) portion of this Na can also remain at the CdS/CIGSe interface after CdS deposition.[13] Na has a large effect on

the electronic properties of the CIGSe grain surfaces, and thus the CdS/CIGSe interface, contributing to the valence band DOS, and reducing the surface dipole.[14,15] Na is also known to increase the overall doping density of the absorber layer,[16] and thus Na would be expected to play a large role in the p-n junction formation in CIGSe. In more recent years, the role of K in CIGSe has also been investigated.[17]

Alternative methods of Na incorporation have been developed, which often include the addition of a Na barrier at the surface of the glass, followed by an intentional Na precursor layer, such as NaF, Na_2Se, or Na_2S, deposited either below the absorber layer, during absorber deposition, or on the surface.[1] Alternative methods are more often used in industrial manufacturing, because they allow increased control over Na distribution.[1]

2.4.3 S/Se Intermixing at the Buffer/Absorber Interface

Along with the presence of Na at the CdS/CIGSe interface, intermixing of elements from the two layers can also occur. At the CdS/CIGSe interface, intermixing of In and Se from the CIGSe into the CdS layer, and S from the CdS into the CIGSe layer, has been observed,[18] with the potential formation of $(In_{1-x}Ga_x)_yS_z$ species at the interface.[19] An intermixing of Se from the absorber into the CdS layer has also been observed at the CdS/Cu(In,Ga)$(S,Se)_2$ interface, and shown to vary depending on the S concentration in the absorber.[20] These intermixing effects were demonstrated in high efficiency cells, and might be expected to produce a more beneficial band alignment at this interface.

2.5 CdTe

A brief discussion of the materials and processes used in CdTe production is given here, with a focus on the back contact / CdTe interface and lifetime testing of CdTe-based solar cells, which is relevant for Chapter 6.

2.5.1 Deposition Characteristics of CdTe

CdTe is an ideal material for solar cell applications. The optical direct band gap of 1.44 eV[21] puts it close to the theoretically ideal band gap for the absorption of sunlight,[22] and CdTe is easily converted between p-type and n-type based on the prevalence of Cd vacancies (V_{Cd}) and/or the presence of dopants.[23] CdTe-based solar cells achieve their highest efficiencies when grown polycrystalline (which generally makes deposition both quicker and less expensive) and in a superstrate configuration (i.e., depositing onto the glass and TCO).[1] After deposition of the TCO, CdS, and CdTe layers, $CdCl_2$ "activation" is performed on the CdTe surface, which produces a dramatic increase in the cell conversion efficiency. Cl from the $CdCl_2$ treatment diffuses through the CdTe layer, predominantly at the CdTe grain boundaries,[24] and to the CdS layer. The $CdCl_2$ treatment has been shown to cause an n- to p-type conversion in the CdTe layer,[23] an enlargement and/or recrystallization of the grains in the CdTe layer,[25] and to cause the diffusion of S from the CdS buffer into the CdTe layer, which has also been shown to accumulate at the CdTe/metal interface after back contact deposition and final annealing treatment.[24,26]

The final interface formed in CdTe-based solar cell is between the semiconductor and the metal back contact, where, as discussed in Section 2.2, an Ohmic contact is desired. This is difficult to achieve for the CdTe/metal interface, in part due to the large band gap (1.44 eV) and commonly high electron affinity (~ 4.5 eV) at the surface of

CdTe.[27] Treatment of the CdTe surface prior to back contact deposition (e.g., chemical etching) and the inclusion of Cu in the back contact are commonly employed, both of which help to produce a lower energy barrier at the metal-to-semiconductor interface.[28] Cu also readily diffuses into the CdTe, beneficially altering the doping levels in the absorber. In the bulk, Cu predominantly forms Cu antisites at Cd locations (Cu_{Cd}), often by filling Cd vacancies (V_{Cd}).[28–30] These defects act as shallow acceptors (making the material more p-type).[31] Directly at the CdTe/back contact interface, Cu can also form $Cu_{2-x}Te$ compounds, which would form a more n-type region at this boundary of the CdTe layer.[28,31] This would be expected to reduce and narrow the barrier often present at the back contact,[28] which would allow tunneling through the Schottky barrier and produce an improved cell efficiency.

2.5.2 Accelerated Lifetime Testing

While Cu provides an initial increase in cell efficiency, Cu from the back contact is also known to play a major role in CdTe solar cell degradation over time. Accelerated lifetime treatments, also known as stress treatments, have been developed to speed up the chemical and physical mechanisms at play as the solar cell ages with time. These treatments are performed on non-encapsulated solar cells, meaning the material layers are not physically isolated from the ambient environment by a final sealing layer. Common stress treatment parameters include elevated temperatures (50-200 °C), illumination or dark conditions, in air, N_2, or vacuum, and the electrical connection of the cell, such as open- or short-circuit, or under bias.[32] These stress treatments are performed for a variety of durations (e.g., 1,000 hours, 1 week, etc.), with 1000 hours of stress under certain conditions corresponding to an estimated 100 years in the field.[32]

2.5.3 Degradation Mechanisms in CdTe

Heat stress treatments have shown a reversal of the positive benefits realized from Cu inclusion. An increased diffusion of Cu to the CdS layer, and accumulation at the CdTe/CdS and CdS/ITO interfaces, has been observed after heat stress treatment.[30,33,34] Cu is therefore thought to be responsible for the degradation of the p-n junction, which manifests as a decrease in the open circuit voltage,[32] or V_{OC} (the built-in voltage, or voltage drop over the solar cell junction when measured in an open circuit). The formation of a Cu oxide layer at the CdTe/metal interface has also been suggested, which would form a barrier to charge transport at the metal-semiconductor interface. This manifests as a "rollover," or limited current at higher forward bias values, in the I-V curve of the solar cell.[34] Evidence for S oxidation under the back contact after stress treatment has also been found.[26]

2.6 Photosensitized Nanocomposite Materials

The optoelectronic properties of nanocomposite materials have been discussed and studied as a concept for many years,[35,36] and have been successfully demonstrated in light-emitting diodes (LEDs)[37] and solar cell materials.[38,39] A brief discussion of the nanoparticle band gap, and the nanocomposite structure and interfaces is given here, as relevant to the CdTe/ZnO nanocomposites investigated in Chapter 7.

2.6.1 Quantum Band Structure

In quantum mechanics, the allowed energy states for a particle confined in a system are given by:[40,41]

$$E_n = \frac{h^2 n^2}{8mL^2} \tag{2.2}$$

where h is Planck's constant, n is an integer number, m is the mass of the particle, and L is the distance (or area) in which the particle is confined. From this simple equation, it can be seen that as L becomes smaller (more specifically, in the range of the particle wave function), the energy of the particle, E_n, and the separation of the energy states become larger. In large-scale solids, L is sufficiently large such that the change in energy between adjacent states is small, and the allowed energy levels become essentially continuous. However, in the quantum regime, the change in energy between consecutive states is greater, and the quantization of the energy states becomes apparent.[40] This, in turn, affects the E_g of the nanoparticle such that as the particle decreases in size, the energy between the VBM and CBM increases. This is particularly interesting for semiconductor materials, for which the exciton energy can be tuned based on the nanoparticle dimensions, and in fact, the exciton energy can be modeled to again show an increasing exciton energy with decreasing particle size.[40] In recent years, models

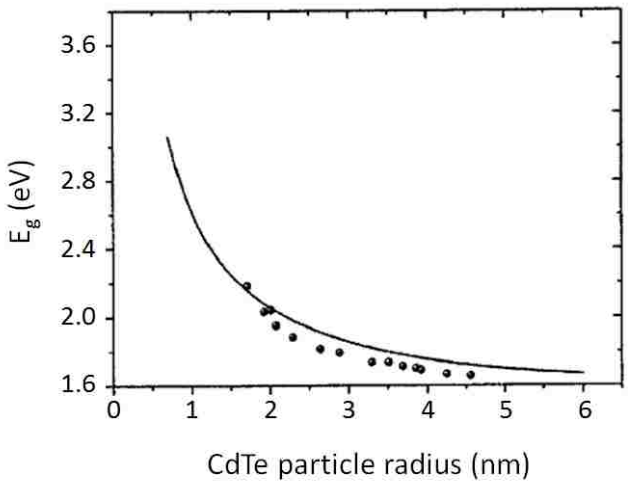

Fig. 2.4: Experimental data (black dots) and calculated values (solid line) of the band gap energy vs. particle radius for CdTe quantum dots. Figure adapted from Ref. 42.

predicting the E_g of semiconductor quantum dots have shown good agreement with experimental data, as seen in Fig. 2.4, which shows calculated and experimental data by Baskoutas et al.[42] As expected from Eq. 2.2 and the squared length term in the denominator, the E_g follows a reciprocal curve as the particle radius increases.

2.6.2 Nanocomposite Structure

Nanocomposite materials are a unique material class which aims to monopolize on the unique properties of nanoparticles for photosensitization and photoabsorption. Here, a wide band gap material is used as a matrix in which semiconductor nanoparticles are embedded. The wide band gap material serves two purposes: while this matrix material can absorb higher energy photons (potentially creating electron-hole pairs), it allows lower energy photons to pass through. These lower energy photons are then available to be absorbed by the semiconductor nanoparticles, which can efficiently absorb a wide range of energies depending on the nanoparticle size. Second, the matrix material offers a long diffusion length for exciton transport, due to the wide band gap, which reduces the probability of electron-hole recombination.

As might be expected, one of the main hurdles to the use of nanocomposites as a photovoltaic material is the efficient transport of photoexcited carriers over the semiconductor-to-matrix interface. A continuous CBM and the absence of an energy barrier at this interface would be desired to facilitate electron transport between the nanoparticle and matrix material. As described for $Cu(In,Ga)Se_2$ and CdTe-based thin-film solar cells, interfaces are most often not abrupt and not simple. This is exemplified for nanocomposites in the work by Shih et al., in which Ge:ITO and Ge:ZnO nanocomposites were investigated.[43] Here, Raman spectroscopy revealed the presence of

a GeO_x interfacial species in the Ge-ITO nanocomposite materials after annealing, and the presence of an energy barrier at the Ge-ZnO interface was predicted based on the shift to higher energy of the absorption onset. The ultimate utility of this material class may depend on a deeper understanding of the electronic properties of the matrix/nanoparticle interface.

2.7 References

(1) Romeo, A.; Terheggen, M.; Abou-Ras, D.; Bätzner, D. L.; Haug, F.-J.; Kälin, M.; Rudmann, D.; Tiwari, A. N. *Prog. Photovolt. Res. Appl.* **2004**, *12*, 93–111.

(2) Rau, U.; Schock, H. W. In *Practical Handbook of Photovoltaics*; Elsevier Ltd., 2012; pp. 323–371.

(3) Pierret, R. F. *Semiconductor Device Fundamentals*; Addison-Wesley Publishing Company, 1996.

(4) Reinhard, P.; Buecheler, S.; Tiwari, A. N. *Sol. Energy Mater. Sol. Cells* **2013**, *119*, 287–290.

(5) Osborne, M. Hanergy's Solibro has 20.5% CIGS solar cell verified by NREL http://www.pv-tech.org/news/hanergys_solibro_has_20.5_cigs_solar_cell_verified_by_nrel (accessed Sep 29, 2014).

(6) Noufi, R.; Gabor, A. M.; Tuttle, J. R.; Tennant, A. L.; Contreras, M. A.; Albin, D. S.; Carapella, J. J. Method of fabricating high-efficiency Cu(In,Ga)(SeS)2 thin films for solar cells. US5441897 A, August 15, 1995.

(7) Albin, D. S.; Carapella, J. J.; Tuttle, J. R.; Contreras, M. A.; Gabor, A. M.; Noufi, R.; Tennant, A. L. Recrystallization method to selenization of thin-film Cu(In,Ga)Se2 for semiconductor device applications. US5436204 A, July 25, 1995.

(8) Repins, I.; Contreras, M. A.; Egaas, B.; DeHart, C.; Scharf, J.; Perkins, C. L.; To, B.; Noufi, R. *Prog. Photovolt. Res. Appl.* **2008**, *16*, 235–239.

(9) Brown, G.; Stone, P.; Woodruff, J.; Cardozo, B.; Jackrel, D. In *2012 38th IEEE Photovoltaic Specialists Conference (PVSC)*; 2012; pp. 003230–003233.

(10) Hedstrom, J.; Ohlsen, H.; Bodegard, M.; Kylner, A.; Stolt, L.; Hariskos, D.; Ruckh, M.; Schock, H. In *, Conference Record of the Twenty Third IEEE Photovoltaic Specialists Conference, 1993*; 1993; pp. 364–371.

(11) Niles, D. W.; Al-Jassim, M.; Ramanathan, K. *J. Vac. Sci. Technol. A* **1999**, *17*, 291–296.

(12) Heske, C.; Eich, D.; Groh, U.; Fink, R.; Umbach, E.; van Buuren, T.; Bostedt, C.; Franco, N.; Terminello, L. J.; Grush, M. M.; Callcott, T. A.; Himpsel, F. J.; Ederer, D. L.; Perera, R. C. C.; Riedl, W.; Karg, F. *Thin Solid Films* **2000**, *361–362*, 360–363.

(13) Heske, C.; Eich, D.; Fink, R.; Umbach, E.; Kakar, S.; Buuren, T. van; Bostedt, C.; Terminello, L. J.; Grush, M. M.; Callcott, T. A.; Himpsel, F. J.; Ederer, D. L.; Perera, R. C. C.; Riedl, W.; Karg, F. *Appl. Phys. Lett.* **1999**, *75*, 2082–2084.

(14) Heske, C.; Fink, R.; Umbach, E.; Riedl, W.; Karg, F. *Appl. Phys. Lett.* **1996**, *68*, 3431–3433.

(15) Heske, C.; Richter, G.; Chen, Z.; Fink, R.; Umbach, E.; Riedl, W.; Karg, F. *J. Appl. Phys.* **1997**, *82*, 2411–2420.

(16) Siebentritt, S.; Guetay, L.; Regesch, D.; Aida, Y.; Depredurand, V. *Sol. Energy Mater. Sol. Cells* **2013**, *119*, 18–25.

(17) Chirilă, A.; Reinhard, P.; Pianezzi, F.; Bloesch, P.; Uhl, A. R.; Fella, C.; Kranz, L.; Keller, D.; Gretener, C.; Hagendorfer, H.; Jaeger, D.; Erni, R.; Nishiwaki, S.; Buecheler, S.; Tiwari, A. N. *Nat. Mater.* **2013**, *12*, 1107–1111.

(18) Heske, C.; Eich, D.; Fink, R.; Umbach, E.; van Buuren, T.; Bostedt, C.; Terminello, L. J.; Kakar, S.; Grush, M. M.; Callcott, T. A.; Himpsel, F. J.; Ederer, D. L.; Perera, R. C. C.; Riedl, W.; Karg, F. *Appl. Phys. Lett.* **1999**, *74*, 1451–1453.

(19) Pookpanratana, S.; Repins, I.; Bär, M.; Weinhardt, L.; Zhang, Y.; Félix, R.; Blum, M.; Yang, W.; Heske, C. *Appl. Phys. Lett.* **2010**, *97*, 074101.

(20) Weinhardt, L.; Bär, M.; Pookpanratana, S.; Morkel, M.; Niesen, T. P.; Karg, F.; Ramanathan, K.; Contreras, M. A.; Noufi, R.; Umbach, E.; Heske, C. *Appl. Phys. Lett.* **2010**, *96*, 182102.

(21) Gebhardt, W. *Mater. Sci. Eng. B-Solid State Mater. Adv. Technol.* **1992**, *11*, 1–9.

(22) Shockley, W.; Queisser, H. J. *J. Appl. Phys.* **1961**, *32*, 510.

(23) Basol, B. M.; Ou, S. S.; Stafsudd, O. M. *J. Appl. Phys.* **1985**, *58*, 3089.

(24) Terheggen, M.; Heinrich, H.; Kostorz, G.; Romeo, A.; Baetzner, D.; Tiwari, A. N.; Bosio, A.; Romeo, N. *Thin Solid Films* **2003**, *431–432*, 262–266.

(25) Qi, B.; Kim, D. W.; Williamson, D. L.; Trefny, J. U. *J. Electrochem. Soc.* **1996**, *143*, 517–523.

(26) Liu, X.; Paudel, N.; Compaan, A.; Sun, K.; Weinhardt, L.; Bär, M.; Pookpanratana, S.; Heske, C.; Fuchs, O.; Yang, W.; Denlinger, J. D. In *2009 35th IEEE Photovoltaic Specialists Conference (PVSC)*; 2009; Vol. 35th, pp. 02107–02110.

(27) Durose, K.; Edwards, P. R.; Halliday, D. P. *J. Cryst. Growth* **1999**, *197*, 733–742.

(28) Corwine, C. R.; Pudov, A. O.; Gloeckler, M.; Demtsu, S. H.; Sites, J. R. *Sol. Energy Mater. Sol. Cells* **2004**, *82*, 481–489.

(29) Balcioglu, A.; Ahrenkiel, R. K.; Hasoon, F. *J. Appl. Phys.* **2000**, *88*, 7175–7178.

(30) Grecu, D.; Compaan, A. D. *Appl. Phys. Lett.* **1999**, *75*, 361–363.

(31) Wei, S.-H.; Zhang, S. B.; Zunger, A. *J. Appl. Phys.* **2000**, *87*, 1304–1311.

(32) Dobson, K. D.; Visoly-Fisher, I.; Hodes, G.; Cahen, D. *Sol. Energy Mater. Sol. Cells* **2000**, *62*, 295–325.

(33) Asher, S. E.; Hasoon, F. S.; Gessert, T. .; Young, M. R.; Sheldon, P.; Hiltner, J.; Sites, J. In *Conference Record of the Twenty-Eighth IEEE Photovoltaic Specialists Conference, 2000*; 2000; pp. 479–482.

(34) Visoly-Fisher, I.; Dobson, K. D.; Nair, J.; Bezalel, E.; Hodes, G.; Cahen, D. *Adv. Funct. Mater.* **2003**, *13*, 289–299.

(35) Chatterjee, S.; Goyal, A.; Shah, S. I. *Mater. Lett.* **2006**, *60*, 3541–3543.

(36) Zaban, A.; Micic, O. I.; Gregg, B. A.; Nozik, A. J. *Langmuir* **1998**, *14*, 3153–3156.

(37) Kim, Y.-K.; Choi, K.-C.; Baek, Y.-K.; Shin, P.-W. *Mater. Lett.* **2014**, *124*, 129–132.

(38) Sacco, A.; Porro, S.; Lamberti, A.; Gerosa, M.; Castellino, M.; Chiodoni, A.; Bianco, S. *Electrochimica Acta* **2014**, *131*, 154–159.

(39) O'Regan, B.; Grätzel, M. *Nature* **1991**, *353*, 737–740.

(40) Atkins, P.; de Paula, J. In *Atkin's Physical Chemistry*; Oxford University Press: Oxford, 2006.

(41) Levine, I. N. In *Quantum Chemistry*; Pearson Prentice Hall: New Jersey, 2009; pp. 24–30.

(42) Baskoutas, S.; Terzis, A. F. *J. Appl. Phys.* **2006**, *99*, 013708.

(43) Shih, G. H.; Allen, C. G.; Potter Jr., B. G. *Nanotechnology* **2012**, *23*, 075203.

CHAPTER 3

MEASUREMENT TECHNIQUES

This chapter presents the equipment and measurement techniques utilized in this dissertation, especially the nuances of these techniques that must be understood to accurately interpret the data. The chapter begins with discussions relevant to Photoelectron Spectroscopy (PES), which includes the more specific techniques of X-ray Photoelectron Spectroscopy (XPS), Ultraviolet Photoelectron Spectroscopy (UPS), and Hard X-ray Photoelectron Spectroscopy (HAXPES). Included in this section is an overview of sample handling, ion stimulated desorption as a surface cleaning technique, and sample grounding and the surface photovoltage effect, all of which pertain strongly to PES and related surface-sensitive techniques. This discussion is followed by an overview of Inverse Photoemission Spectroscopy (IPES), which is a unique, electron-in, photon-out process. The synchrotron-based techniques of X-ray Emission Spectroscopy (XES) and X-ray Absorption Spectroscopy (XAS) are then covered, both of which are photon-in, photon-out processes.

3.1 Introduction

The photoelectron spectroscopy techniques included in this dissertation involve single-excitation perturbations of atoms from initial to final state. These processes follow Fermi's golden rule for a time-dependent perturbation. Fermi's golden rule states:[1,2]

$$\omega_{i\to f} \propto \frac{2\pi}{\hbar}|\langle f|r|i\rangle|^2\delta(E_f - E_i - h\nu), \tag{3.1}$$

which describes the probability (ω) of a transition to occur from the initial state, *i*, to the final state, *f*. The transition is governed by a matrix element including the perturbation, *r* (e.g., the incoming photon, *hν*, or electron). The delta function originates from the density of energy states around the final state, which becomes more narrow (approaching a δ-function), as $t \rightarrow \infty$ (derived elsewhere[2,3]). The delta term ensures that the conservation of energy is maintained.

3.2 Photoelectron Spectroscopy (PES)

PES is based on the photoionization of atomic core levels, and the measurement of the energy of the emitted photoelectrons. The energy of the incoming photon, and the energy of the outgoing electron are related by the equation:[4]

$$h\nu = E_K + |E_B| \tag{3.2}$$

This states that the Kinetic Energy (E_K, or KE) of the emitted electron is equal to the energy of the photon (hν) minus the absolute value of the Binding Energy (E_B, or BE) of the electron to the atom. The energy scale is referenced to E_F for this equation, such that the work function of the sample is included in the E_K term. The XPS process and these two energies are depicted on the left of Fig. 3.1 (a). Reference to E_F is achieved by putting the sample in electrical contact with the detector (i.e., grounded). The energy axis is regularly calibrated by following an ISO standard[5] in which the KE of photoelectron peaks from pure Cu, Ag, and Au foils are compared to the accepted literature values.

Along with XPS, a second process also occurs which gives rise to X-ray-excited Auger Emission Spectroscopy (XAES). Here, an electron in an outer (lower BE) state relaxes into the hole created by the photoemission process. The involved change in

energy can be transferred to a second electron (the Auger electron) which, if sufficient, can be excited out of the sample. This is depicted on the right of Fig. 3.1. (a). The KE of the Auger electron is dependent on the energy difference between the state of the relaxing electron and the hole (designated in Fig. 3.1 (a) as E_A). Auger spectra are therefore independent of the photon energy used, and are plotted as intensity vs. KE. Auger emission is also independent of charging effects, if adequate grounding of the sample is not achieved, since both states involved are equally affected. Conversely, the KE of photoelectrons is directly related to the photon energy through Eq. 3.2, while the BE of a particular state will be the same regardless of the photon energy. As such, photoelectron peaks are plotted as intensity vs BE.

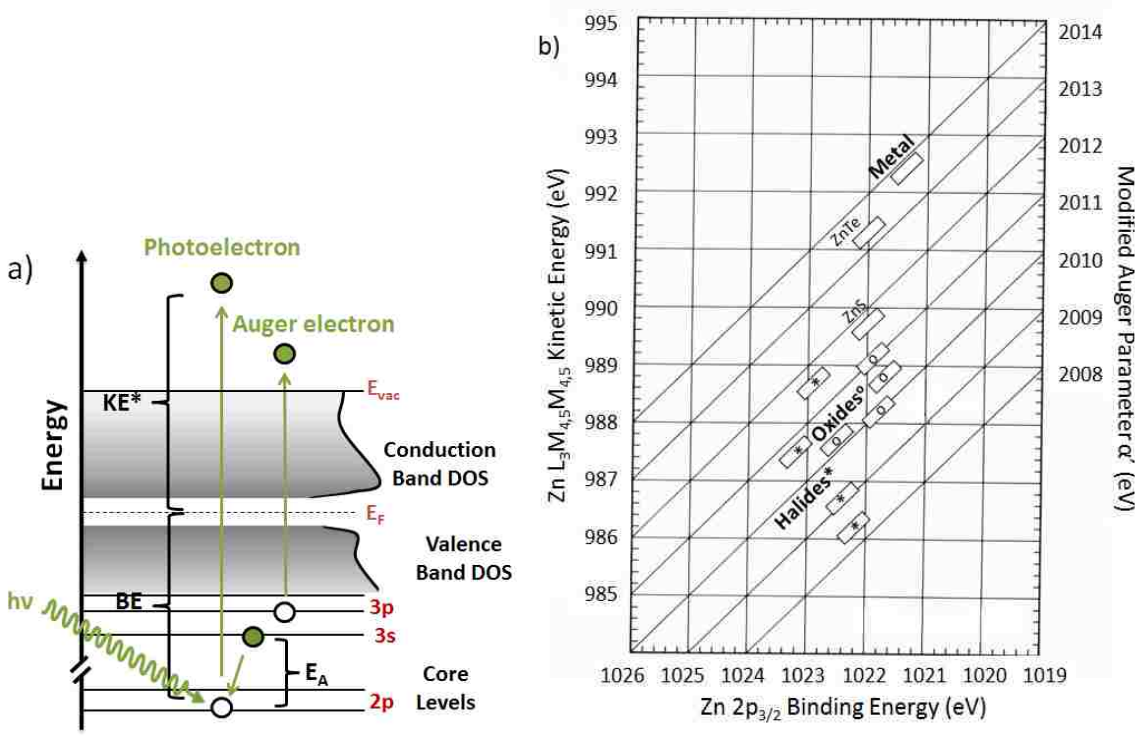

Fig 3.1: a) Schematic of X-ray Photoelectron (XPS) and Auger Emission (XAES) spectroscopy transitions. KE* includes the KE of the emitted electron with respect to E_{vac}, as well as the work function of the surface. b) 2-D α' plot of Zn, adapted from Ref. 7.

This also makes it more straightforward to determine the Modified Auger Parameter, α', which is calculated by adding the BE of the most prominent photoelectron peak and the KE of the most defined Auger emission line:

$$\alpha' = KE_{Auger} + BE_{Photoelectron} \quad . \tag{3.3}$$

This yields a positive energy value, independent of the photon energy used, that is easily calculated and compared to reference values.[6] The α' is a powerful tool for determining the chemical environment of a given element. While the energy position of just the photoelectron peak can often distinguish between different chemical bonding and local environments, additional and more dramatic variation in the Auger emission energy is often seen, in part because the Auger transition involves: 1) lower BE core-levels closer to the VB, which are more strongly affected by bonding environment, 2) the energetic spacing between *two* electron orbitals, each of which may respond differently to changes in the electron potential surrounding the element, and 3) final state effects, such as hole-hole interactions, extra-atomic screening, or hole lifetimes. In some situations, a shift of the photoelectron peak may be small or absent, while the Auger peak shows a strong shift. This can be seen in the 2-D α' plot for Zn, shown as an example in Fig. 3.1 (b),[7] where the Zn $2p_{3/2}$ peak energies are plotted along the x-axis, the Zn LMM peak energies along the left y-axis, and the calculated α' is listed on the right y-axis. Here, only a small shift (< 0.5 eV) in the Zn $2p_{3/2}$ binding energy is seen between metallic Zn and ZnO, while a more dramatic shift of almost 3 eV is seen for the Zn LMM peak. This also results in a change in the α' value by a full 2.5 eV. This easily illustrates the utility of plotting α' in some situations, to help identify the chemical environment of an element.

3.2.1 Line Width and Peak Fitting

The peak width, or full width at half maximum (FWHM), of the peaks in an XPS spectrum are affected by a number of factors. The minimum peak width is the natural line width of the transition, which is governed by the lifetime of the created core hole (the time between excitation of the electron out of the atom and relaxation of the atom to fill the electron vacancy). This is based on the uncertainty principle for energy and time,

$$\Delta E \Delta t \geq \frac{\hbar}{2} \ . \tag{3.4}$$

The uncertainty principle shows that as the lifetime, Δt, decreases (approaches zero), the change in energy, ΔE (peak width), increases and approaches ∞, demonstrating complete uncertainty in the energy as certainty in the time is established.[8] Typical lifetimes in XPS are between 10^{-13} and 10^{-15} seconds,[9] corresponding to a minimum theoretical line width of 0.003 to 0.3 eV.

The line width of the photon source also adds to the width of the XPS peaks. The most commonly used x-ray lines, Mg and Al K_α, are used due to both their sufficiently high photon energy, which allows excitation of a large number of core levels, and their sufficiently small emission line width, which is the limiting factor for peak width. The line width of Mg and Al K_α emission are approximately 0.7 and 0.85 eV, respectively.[9]

Lastly, the analyzer and its settings also affect resolution. XPS measurements are usually performed in Fixed Analyzer Transmission (FAT) mode, which retards the emitted electrons to a constant energy (the pass energy, PE), prior to entering the hemisphere. The electrons are retarded so that a smaller hemisphere radius is needed to achieve a higher resolution, and the electrons are measured at a constant energy so that a constant absolute resolution is achieved over the full energy range.[9,10]

These three factors combined give the full resolution for an XPS measurement as:

$$\Delta E = \left(\Delta E_n^2 + \Delta E_p^2 + \Delta E_a^2\right)^{\frac{1}{2}} \quad (3.6)$$

where ΔE_n is the natural line width, ΔE_p is the photon source line width, and ΔE_a is the analyzer resolution.[9] These factors are "built-in" to the experiment and the equipment being used.

Another aspect of resolution, which the user has control over, is the positioning of the sample relative to the analyzer entrance cone. The analyzer is designed to "focus" at an exact working distance (40 mm for the SPECS PHOIBOS 150 used here[11]). To ensure the proper working distance is used, consecutive measurements are taken of a given peak while varying the sample height relative to the analyzer. The FWHM of the peak will reach a minimum at the proper working distance. Alignment of the sample with respect to the axis of the analyzer must also be ensured, and is especially important when measuring with a small-spot excitation sources (e.g., at the synchrotron).

Aside from the experimental broadening discussed so far, the peak FWHM may also vary due to the presence of multiple chemical species or a less defined chemical environment, such as multiple closely spaced peaks overlapping within a single peak. For these situations, fitting of the peak in question may be useful to distinguish chemical species and/or to determine the intensity of an individual species. The fits presented in this dissertation were performed with the program Fityk,[12] and primarily involve a description of the background and a description of the peak.

Proper choice and positioning of the background is important, since it will strongly affect the peak shape and area. A Shirley background is often used in XPS to describe the background signal.[13] It is well-suited for materials with a small or absent E_g,

such as metals, due to the tail of inelastic scattered electrons that extends from the photoelectron peak to higher BE, contributing to the background. An example of metal peaks (Ag 3d) and the calculated Shirley background is shown in Fig.3.2 (a). A linear background is more suited for the fits present in this dissertation, however, since the materials being investigated are semiconductors with band gap values of 1 eV or greater. The relatively wide band gap of these material results in a tail of scattered electrons that is offset from the main peak by the energy of the band gap, such that a step function under the peak is not justified to describe the spectrum. The positioning of the linear background relative to the data points is also significant, such that if the background is set too high it may artificially reduce the Lorentzian portion of the peak broadening (described below). Thus the background should still be slightly below the data at the edges of the fit region.

For the peak fits performed here, a Voigt profile was chosen to describe the peak

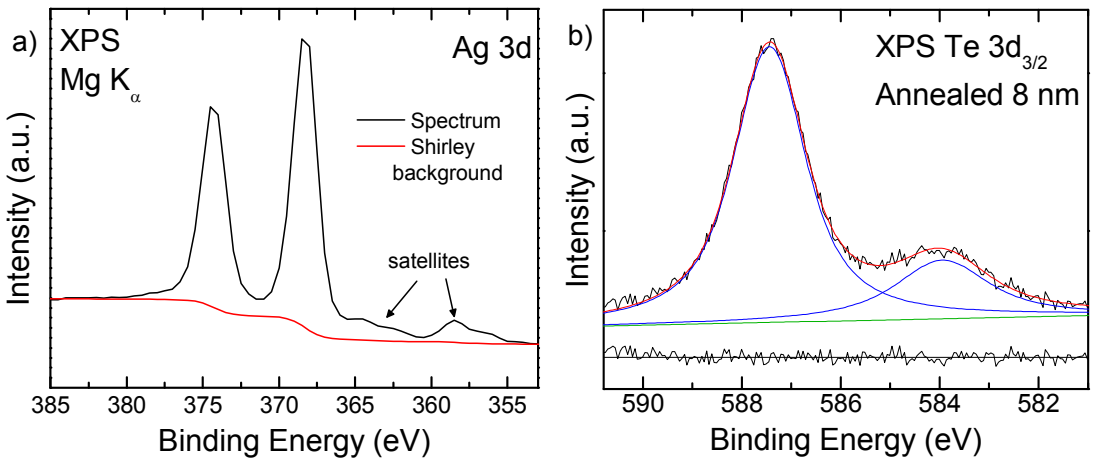

Fig. 3.2 a) An example of a Shirley background, calculated for the Ag 3d metal peaks. b) A fit of a semiconductor material using a linear background and Voigt profiles.

shape. The Voigt profile is a convolution of Lorentzian (from the lifetime broadening) and Gaussian (from the instrumental broadening) functions. The "VoigtA" profile option in fityk was used, which also allows the peak area variable to be specified by the user (e.g., as a fraction of another peak area). An example of a two-peak fit using a linear background and two Voigt profiles, taken from Chapter 7, is shown in Fig. 3.2 (b).

When fitting a spectrum or a set of spectra, as many parameters as possible should be fixed or constricted in order to reduce the number of variables. For example, the Gaussian broadening can be set equal for all peaks, since the instrumental broadening would be expected to be constant, while the Lorentzian broadening can be set equal for peaks of the same transition (e.g. all Cu $2p_{3/2}$ peaks), since the transition lifetime should be approximately the same. The peak area ratios for doublet peaks (from the spin-orbit splitting of orbitals with a quantum number, $\ell > 0$) and the spacing between these peaks are also known, and can be fixed in the fit.

3.2.2 Factors Affecting Line Intensity

PES is often used to gain information not only of the elements present in the sample, but also the amount of each element. A large number of factors contribute to the intensity of a peak, and in complex ways. Taking from the discussions by M. P. Seah,[14] and Moulder and Stickle,[4] a simplified relationship between these factors is given below:

$$I_A = \sigma_A \, y \phi f T n_A \lambda_A \qquad (3.7)$$

where σ_A is the cross section of the electron orbital of element A being measured, y is the detection efficiency for the transmitted electrons, ϕ is the angle between the photon source and detected electron (usually the "Magic Angle", discussed below), f is the photon flux (photons/cm^2-sec), T is the transmission function of the hemisphere, n_A is the

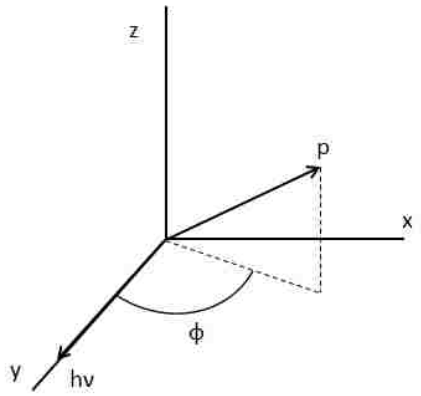

Fig. 3.3: Photoemission angle geometry, adapted from Ref. 17. Here, Φ is the angle between the vector of the photon source, shown along the y-axis, and the vector p, of the emitted photoelectron reflected onto the x-y plane.

number of atoms of element A per unit volume, and λ_A is the Inelastic Mean Free Path (IMFP) of the produced photoelectrons.

The emitted electrons in PES have an angular distribution that must be accounted for to determine the expected intensity for a given orbital. For laboratory-based XPS with a non-polarized photon source, the angle (Φ in Fig. 3.3) between the source (hν) and the vector of the detected electrons (p) projected onto the x-y plane is 54.7°. This is the "Magic Angle", at which the maximum photoelectron intensity is emitted, and the asymmetry parameters (from the dipole approximation), which alter the transition cross section, cancel. The cross sections for all elements with this set-up and either a Mg and Al K_α photon source have been calculated and are available in the literature.[15,16] It must be noted that these calculations require simplified approaches, which necessitate substantial error bars. The asymmetry parameters for measurements performed in different geometries and with different photon energies are also available.[16–18]

The IMFP describes the distance electrons of a certain KE can travel through a material before 1/e of the original signal intensity is lost due to inelastic scattering.[9] The IMFP is affected by the material properties and, more predictably, the KE of the electron, approximately following the "universal curve" shown in Fig. 3.4.[19] This model gives a

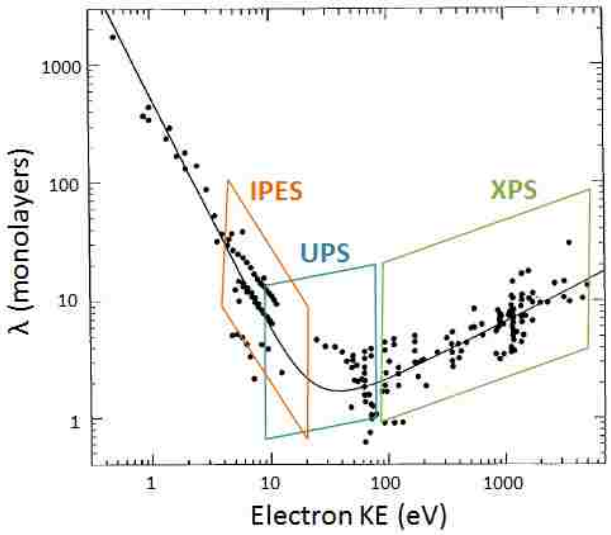

Fig 3.4 Experimental data (dots) and the resulting universal curve (solid line) showing the relationship between the Inelastic Mean Free Path, λ, and the KE of the electron. The KE of electrons in IPES, UPS, and XPS are indicated. The universal curve plot was taken from Ref. 19.

good approximation of the IMFP over a wide energy range, including the electron energy range for laboratory XPS, UPS, and IPES. From this curve, a minimum in the IMFP is seen for electrons around 20-50 eV, with higher KE electrons following a linear, increasing trend, roughly equal to $\sqrt{KE}$. From the universal curve it can be seen that, while the IMFP does change with the KE of the emitted electron, above ~ 50 eV the changes are minor over small variations in the KE, and thus two peaks 100 eV or so separated can be expected to originate from electrons with comparable IMFP values. Further experiment and calculation has more recently lead to the TPP-2M model, by which the IMFP of an electron is calculated for a given KE based on the material density, band gap, atomic mass, and number of valence electrons.[20] This model has been shown to match well to experimental data,[21,22] and multiple software applications are available for users to calculate more precise IMFP values.[23,24]

The full intensity relationship can be simplified by deriving ratios of two elements, or of the same element for two samples. For a given measurement, it can be reasonably assumed that the photon flux (f) and the measurement geometry, and thus ϕ, will not change. While the detection efficiency (y), IMFP (λ_A), and the transmission function (T) *will* vary with the electron KE, these changes are relatively small over small variations in energy. Thus, when comparing photoelectron peaks close to one another in KE and measured in the same measurement set-up (especially in the same spectrum), equation 3.7 simplifies and the ratio of the elemental composition can be estimated from:

$$\frac{n_A}{n_B} = \frac{I_A}{I_B} \cdot \frac{\sigma_B}{\sigma_A} \tag{3.8}$$

where I is the intensity of the peak, σ the cross section, and n the number of atoms. A sufficient error bar is required with this calculation, to account for the small changes to the y, λ_A, and T values, which were not accounted for, and the uncertainty in the cross sections.

3.2.3 XPS and UPS Set-up

X-ray photoelectron spectroscopy (XPS) was performed at UNLV on the "Andere ESCA" chamber, equipped with a dual-anode Mg (1253.6 eV) and Al K_α (1486.6 eV) SPECS XR50 x-ray source, and a SPECS PHOIBOS 150 multi-channel detector (MCD) hemispherical analyzer. The spectra presented in this dissertation were measured in FAT mode at a typical PE of 50 eV for large-energy-range surveys, and 20 eV for detailed spectra. The ultra-high vacuum (UHV) chamber was consistently at a pressure $< 5\times10^{-10}$ Torr. A similar XPS set-up was also used at the Helmholtz-Zentrum Berlin für Materialien und Energie GmbH, which also consisted of a SPECS dual-anode x-ray

source and a SPECS PHOIBOS hemispherical analyzer, with pressures consistently in the 10^{-9} Torr range.

Ultraviolet Photoelectron Spectroscopy (UPS) was also measured in the "Andere ESCA" chamber, with the analyzer described above. A UV gas discharge lamp was used, capable of emitting both He I (21.2 eV) and He II (40.8 eV) radiation, depending on the He pressure administered. A much lower PE (1-4 eV) and a smaller entrance slit relative to XPS were used for the analyzer due to the high intensity of the photon source, resulting in a higher overall resolution for these measurements. To measure the work function, a constant bias voltage was applied to the sample, which ensures a sufficient KE for the low-energy cut-off electrons to escape from the sample surface (i.e., vacuum level) and be detected. The voltage bias was subtracted from the final energy scale by calibrating relative to the E_F measured from a clean Au foil.

While both UPS and XPS can probe the valence band states, UPS is generally better suited for this task. The lower photon energy used in UPS has a significantly higher cross section for valence orbitals (e.g., He I σ is 7.5 for the Cu 3d valence level, compared to 0.021 for Mg K_α[16]). UPS also yields a higher resolution than XPS, due to the narrower line width (in the range of a few meV)[9] and the higher intensity of the photon source, which allows for a lower PE and slit setting on the analyzer. Finally, for non-monochromatic photon sources, Mg and Al K_α both have satellites that are ~ 10 % of the relative intensity and at ~ 10 eV higher KE from the main emission line.[4] This can be problematic if the satellites occur in the region of the VB and VBM, especially, for example, in samples containing elements with strong electron levels at ~10 eV BE (e.g., Cd 4d at 11 eV, and Zn 3d at 10 eV[4]). The satellites associated with He I are lower in

relative intensity and closer to the main emission line (~2 % and 2-3 eV higher KE), and energetically variant from the satellites of He II (~ 8-13 eV higher KE).[25] The ability to excite with either He I or II allows the experimenter to shift the satellite contributions as needed, and more accurately determine the VBM.

3.2.4 HAXPES

Hard X-ray Photoelectron Spectroscopy (HAXPES) was performed at the high brilliance, high resolution KMC-1 beamline at the BESSY II synchrotron. This linearly polarized bending magnet beamline is equipped with a double crystal monochromator including three sets of crystals, which enable the production of photon energies through the most of the soft and hard x-ray range, from 1.7 to 12 keV.[26]

The high kinetic energy electron (HIKE) endstation located on this beamline is equipped with a SCIENTA R4000 hemispherical electron analyzer with a 2-D digital CCD-micro channel plate.[27] The analyzer is oriented with the entrance slit positioned 90° from the photon source and the sample at grazing incidence to the beam. This geometry sets the vector of the detected electrons normal to the sample surface for maximum information depth, and minimizes the inelastic photoemission background.[27] Because $\phi \neq 54.7°$, additional correction factors are needed when determining the cross sections of measured electron levels. Overall, smaller cross sections are realized for these higher photon energy measurements, but this effect is offset by the high brightness of the synchrotron source. The electrons emitted in HAXPES have a longer IMFP than laboratory-based PES due to their higher KE, resulting in an overall enhanced bulk sensitivity. The tunable nature of the photon source also allows for a broad choice of

excitation energies, and the ability to perform a series of measurements with varying depth sensitivity.

3.3 Inverse Photoemission Spectroscopy (IPES)

IPES is an electron-in, photon-out process which probes the unoccupied electronic states at the surface of a material. It can be modeled similar to PES by Fermi's golden rule and the energy and momentum conservation laws. As shown in Fig. 3.5,[28] low-energy electrons (E_i) are inserted above the vacuum level, E_{vac}, and relax, radiatively or non-radiatively, to an unoccupied state in the material (E_f) above the Fermi energy (E_F). The radiatively emitted photons are of the energy $h\nu = E_i - E_f$.

The IPES system at UNLV uses a STAIB low-energy electron gun, which produces electrons by thermionic emission from a BaO-coated emitter ($\phi \sim 2.75$ eV). The

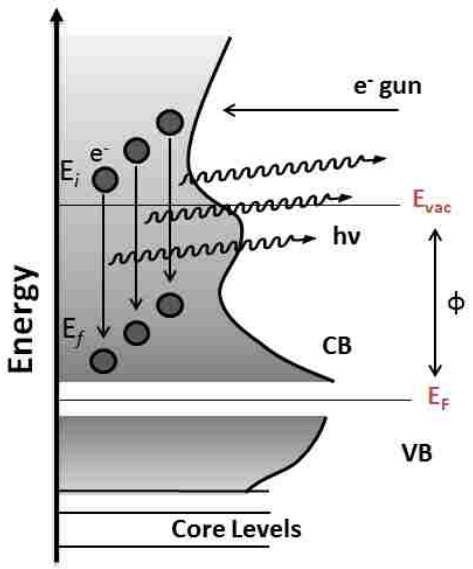

Fig 3.5. The transition in Inverse Photoemission Spectroscopy, in which a low-energy electron relaxes from an energy above the vacuum level (E_{vac}) to an unfilled state above E_F, emitting a photon, hν. The image was modeled after images in Ref. 28.

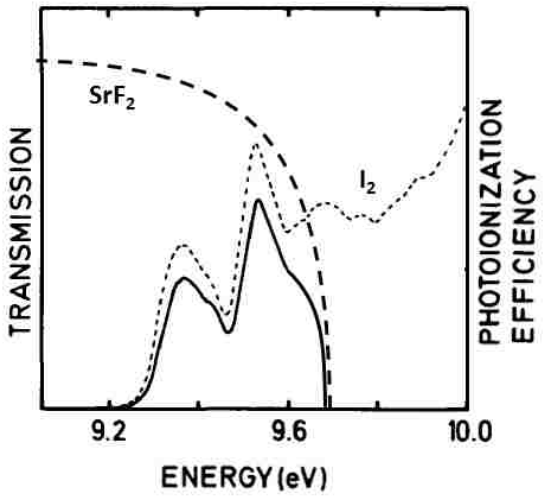

Fig 3.6. Transmission through a SrF_2 window (long dash line) and the photoionization of I_2 (short dash line). The overlapping region shows the bandpass of the Geiger Müller-type detector (solid line). The image was adapted from Ref. 31, and the SrF_2 transmission was determined from Ref. 29.

energy of the electrons is scanned over an energy range (~ 5-20 eV), and the intensity of the photon response from the sample is detected by a band pass Geiger Müller-type detector. The intensity of the response (number of counts) is affected by the density of states (DOS) available for the electron to relax into. The detector combines a SrF_2 window and Ar:I_2 gas mixture to create a band pass with an energy of ~ 9.5 eV, as shown in Fig. 3.6 from the overlap of the photon transmission through the SrF_2 window[29] and the photon energy required to complete the ionization reaction, $I_2 + h\nu \rightarrow {I_2}^+ + e^-$. [30,31] The IPES set-up therefore detects a constant photon energy as the electron energy is scanned. The photon intensity is plotted vs. the electron gun energy, and the onset of the spectrum at low energy corresponds to the minimum energy level in the CB of the material (i.e., the CBM). Similar to UPS, the energy axis is calibrated relative to E_F of a clean Au foil.

3.4 Surface Electronic Band Gap from UPS and IPES

Because the energy axis of UPS and IPES measurements are both calibrated to E_F of a clean, polycrystalline gold foil, they can be plotted on a common energy axis to show the surface electronic band gap. This is especially useful in the analysis of photovoltaic materials, since the chemistry and thus electronic characteristics of the (interface forming) surface often deviates from that of the bulk.

To assign a value to the surface band gap, the energy of the VBM and CBM are determined from linear extrapolation of the leading edge in each spectrum. The linear extrapolation method is used for a number of reasons. First, for both UPS and IPES, some experimental broadening is expected, which makes the low-energy onset less defined. Second, in UPS, which is a k-resolved measurement, the VBM is located at the Γ-point in k-space. Thus, measurement of the "true" VBM requires that a suitable final state is available at the Γ-point at an energy above the VBM equal to the energy of the photon.[32–34] For a polycrystalline sample, similar to those measured in this dissertation, the probability that such a final state is present at the Γ- point is high, but it may or may not be a significant portion of the spectrum, and thus may be obscured in the intensity onset. Finally, additional effects such as inelastic scattering of the escaping electrons, or final-state screening effects in which the screening of the hole is not complete and the escaping electron loses some KE through attraction, will add spectral intensity to lower KE. All of these effects can cause the onset of the VBM to appear farther from E_F, and are accommodated for by linear extrapolation of the leading edge.

3.5 Sample Cleaning

As discussed earlier in relation to the IMFP (see Fig. 3.3), electron-based spectroscopy techniques are extremely surface sensitive. This is especially true for lab-based techniques such as XPS and UPS, which exhibit IMFP values of around 20 monolayers or less. While this may be falsely conceptualized as a well-defined or finite "information depth", the surface sensitivity can be more accurately modeled as an attenuation, described by:[9]

$$I = I_0 e^{\left(\frac{-d}{\lambda sin\theta}\right)} \tag{3.11}$$

where I is the signal intensity measured, I_0 is the full, non-attenuated signal intensity produced at a depth, d, from the sample surface, λ is the IMFP of the electron, and θ is the angle of emission relative to the surface normal. The plot of Eq. 3.11 for two different IMFP values is shown in Fig. 3.7. The area under each curve can be thought of as representing the total signal measured, assuming a homogeneous distribution of the element away from the sample surface.

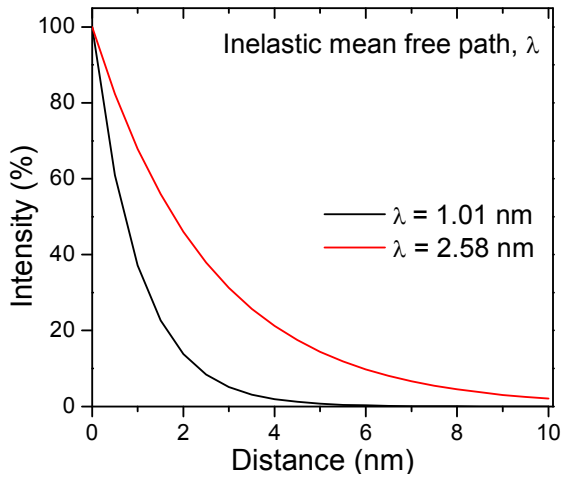

Fig 3.7. The attenuation of electrons traveling through a medium, plotted for two IMFP values as percent intensity of the full value vs. distance through the sample.

From this illustration of XPS signal attenuation, it can be seen how a layer of adsorbates (e.g., water, carbon-containing compounds) on the sample surface can strongly reduce the signal measured from the underlying sample. The effect of adsorbates is also more pronounced for lower KE electrons due to their shorter IMFP (e.g. the black and red line in Fig. 3.7), and can distort the apparent composition of the sample. Adsorbates also inelastically scatter electrons from deeper in the sample, resulting in an increased background, and may alter the chemical environment at the surface of the sample, for example, by oxidizing the top layer of atoms of the sample. Due to these effects, great care was taken in handling the samples measured in this dissertation to avoid air exposure. Samples were predominantly removed from the deposition or treatment chambers with the use of a N_2-filled glove bag, and vacuum sealed in an inert atmosphere for transport. At UNLV, they were unpacked in a N_2-filled glovebox for mounting, and directly moved into the UHV chamber for measurement (pressure $< 1 \times 10^{-9}$ Torr). The measurements were performed in UHV to avoid adsorbate deposition, to facilitate the transfer of electrons from the sample surface into the hemispherical analyzer without scattering losses, and due to the requirement for some components to be operated at high vacuum (HV) or better.

Despite these precautions, an accumulation of surface adsorbates is generally experienced, from the residual gases in UHV and possibly also small impurities in the N_2 environment or impurities in the deposition environment. It is therefore desirable to gently clean the surface and remove these adsorbates, and better measure the "true" surface characteristics. Sputter cleaning, a technique in which ions of a noble gas are used to physically remove atoms from the surface, is a common technique used for producing

very clean surfaces in UHV.[9] While high-energy ions are useful for some applications (e.g., Ar^+ ions in the keV range were used here to clean metal foils for determination of E_F), cleaning of the semiconductor sample surfaces was performed successfully with a low-energy 50 eV Ar^+ "ion-stimulated desorption" treatment. The low energy of this treatment is near the sputter threshold, reducing the possibility of altering the surface through the removal of atoms. A Nonsequitur Technologies Model 1402 ion gun was used to produce the 50 eV Ar^+ ions, and the ion gun beam was rastered to clean a large area of the sample surface. With this ion energy, the sample current during cleaning is generally below 0.4 μA. Multiple, short, 50 eV Ar^+ ion treatments have been shown to be very successful in gently removing non-bonded or weakly bonded adsorbates from CIGSe surfaces, without damaging the underlying film.[35]

An example of a cleaning series performed on the "Cu Poor" $CuInSe_2$ absorber studied in Chapter 5 is shown in Fig. 3.8. Fig. 3.8 a) shows the XPS survey spectra taken

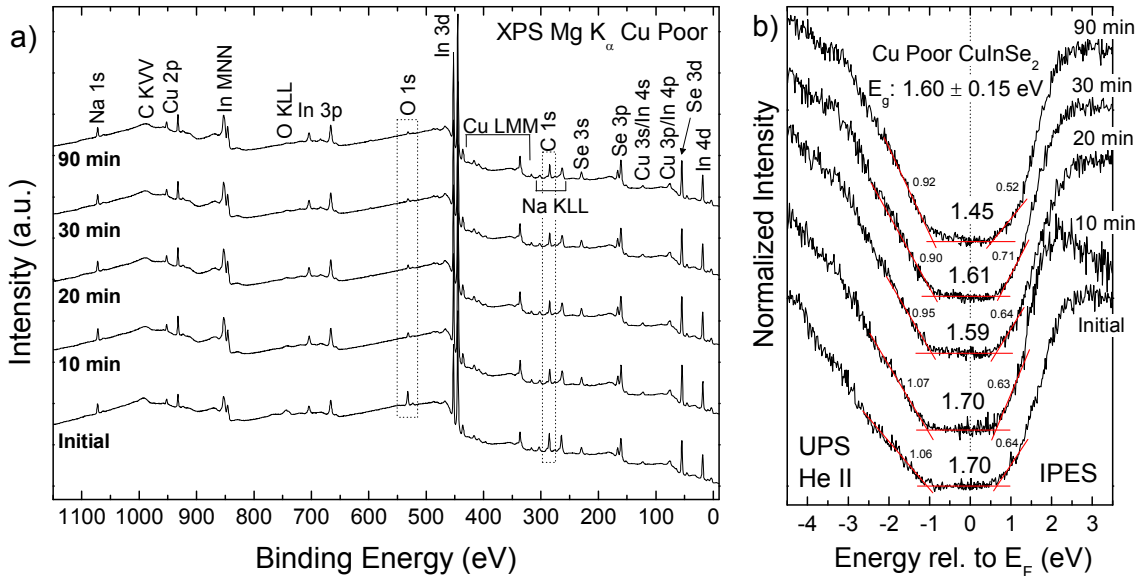

Fig 3.8: a) Mg K_α XPS survey spectra of the "Cu Poor" sample initially (bottom) and after multiple 50 eV Ar^+ ion treatments totaling 90 minutes (top). b) UPS (He II) and IPES spectra taken after each ion treatment and XPS measurement.

from the initial sample (bottom) and after three 10 minute steps and a final 60 minute step of 50 eV Ar^+ ion treatment. The O and C signals (most prominent peaks indicated by dashed boxes) are strongly reduced after the first 10 minute ion treatment, and continue to decrease slightly thereafter. In parallel to the removal of surface adsorbates, all peaks associated with Cu, In, and Se increase.

Detrimental effects (such as metallic states[31,36] and changes in surface stoichiometry[37]) have been observed previously when high energy (500 - 2000 eV) Ar^+ ions are used. Despite using a much lower Ar^+ ion energy, detailed XPS spectra were still taken for all samples after each step of the ion treatment, to monitor these changes. From the detail spectra for the sample in Fig. 3.8, a decrease in Cu-oxide and In-oxide contributions in the Auger spectra was seen after the first 10 minute treatment, and no features indicative of metallic states were observed as the ion treatment progressed.

Evidence of metallic states would also be apparent from the UPS and IPES spectra. This is well illustrated in Fig. 3.9, adapted from Ref. [36], which shows the UPS

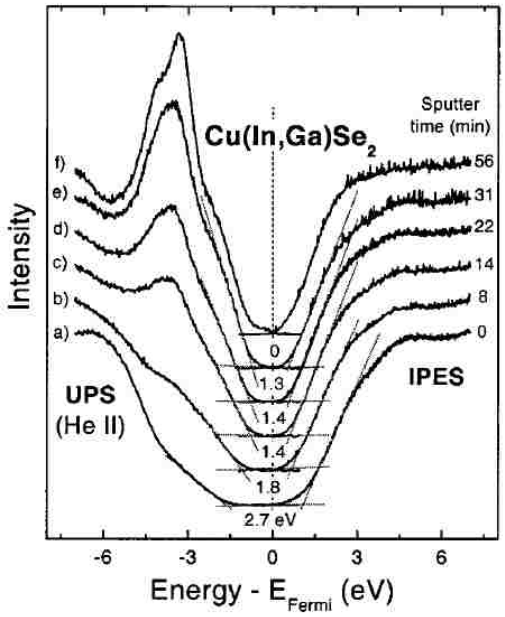

Fig. 3.9: UPS (left) and IPES (right) taken on a CIGSe thin-film sample initially (bottom) and after multiple 500 eV Ar^+ ion sputter cleaning steps. The image was adapted from Ref. 36.

(left) and IPES spectra (right), taken from a CIGSe sample initially (bottom) and after multiple 500 eV Ar^+ sputter treatment steps (total sputter time shown on the right).[36] The linear extrapolation of the VBM and CBM is shown by solid gray lines, and the determined band gap value for each treatment time is stated in the figure. With subsequent cleaning, and thus removal of surface adsorbates, the surface band gap is reduced. Using this high of an Ar^+ ion energy proves to be detrimental to the sample after a significant treatment time, however, as seen from the evolution of a Fermi edge in the 56 and (arguably) 31 minute spectra. Fig. 3.8 b) shows the UPS and IPES spectra taken congruently with the XPS data from the "Cu Poor" CISe sample. The linear extrapolations are indicated by solid red lines, and the VBM, CBM, and band gap values are shown in the figure. As expected, an overall decrease in the surface band gap is seen with increasing ion treatment as the surface adsorbates are removed.[36,38] A band gap of 1.60 ± 0.15 eV is found for both the 20 and 30 minute spectra, with no indication of metallic states forming near E_F.

3.6 Sample Grounding

Due to the removal or addition of charge carriers involved in both PES and IPES, appropriate sample grounding is important. This is especially important when working with semiconducting, photosensitive materials such as photovoltaic absorbers. Measurements were performed with the sample in electrical connection to the sample plate and ground (i.e., the chamber) through a Tantalum or stainless steel grounding clip pressed on the sample surface. For $Cu(In,Ga)Se_2$ absorbers, it was beneficial to ensure that the Mo back contact was also well grounded through the clip.

3.7 Synchrotron-Based X-ray Emission (XES) and Absorption (XAS)

3.7.1 Technique Descriptions

XES measures the relaxation of valence (or core) electrons into a core hole produced by photoionization, as depicted on the right of Fig. 3.10. This is similar to XAES, except that instead of measuring the Auger electron, the competitive process of fluorescence is measured. Auger emission is often favored for low Z atoms (e.g., relaxations into the K and L shells), in which cases fluorescence decay is less probable.[39] For XES measurements, the often low fluorescence yield is overcome by using a high flux photon source, which increases signal and reduces measurement time. XES measures the local partial DOS; "local" because only transitions between states which overlap with the localized core state are possible,[40] and "partial" due to the selection rules for the allowed transitions (e.g., angular momentum quantum number, $\Delta\ell = \pm 1$[41]). Because XES measures transitions between two states, most often between valence band levels and core levels, it is especially sensitive for studying the valence band states, and thus the

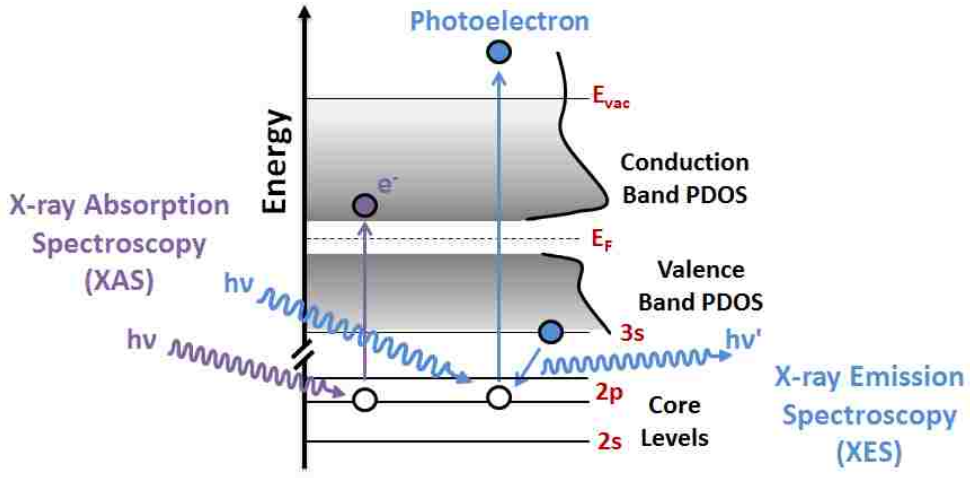

Fig. 3.10: Schematic of x-ray absorption spectroscopy (XAS, left) and x-ray emission spectroscopy (XES, right).

bonding environment of the target element, in an element-specific way.

XAS, shown on the left of Fig. 3.10, probes the unoccupied partial DOS. The photon energy is scanned, starting below the BE of the core level to be studied, and the fluorescence and electron yield from the sample is measured. When the photon energy is sufficient to excite an electron into an unoccupied state, a core-hole is created, which can then be filled radiatively or non-radiatively by electrons from more loosely bound orbitals. The onset of the fluorescence emission (and electron signal) occurs at the energy at which unoccupied states are accessible, and as such XAS probes the CB and CBM, in the presence of a core hole.

3.7.2 Surface Sensitivity

XES and XAS (when measuring the fluorescence yield) are both photon-in, photon-out processes. As such, the surface sensitivity of these measurements is governed by the attenuation length of the photons in the material. Similar to the IMFP, the attenuation length is the distance in the sample after which 1/e of the initial intensity

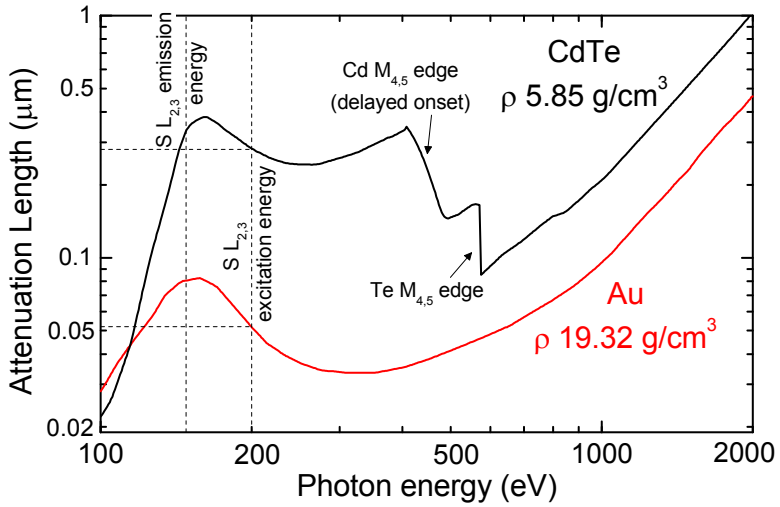

Fig. 3.11: Attenuation of photons from 100 to 2000 eV in CdTe (black) and Au (red). The data values are from Ref. 43.

remains (i.e., has not been absorbed).[42] Depending on the material (the density as well as absorption edges) and the photon energy, the attenuation length of the signal varies from tens to hundreds of nm. This is easily seen from Fig. 3.11, where the photon attenuation in CdTe (black line) and Au (red line) is shown from attenuation data supplied through the CXRO website.[43] An increased attenuation for Au, the more dense of the two materials, is noted, as well as decreases in the attenuation length for CdTe at energies corresponding to Cd and Te absorption edges. Dashed lines are included in Fig. 3.11 as examples, indicating the photon excitation energy (200 eV) and emission energy (~148 eV) for S $L_{2,3}$ XES spectra. Attenuation of the 200 eV photon beam to 36 % of its original intensity occurs after traveling through ~ 50 nm of Au, or ~ 300 nm of CdTe. This information is useful in estimating the degree of surface sensitivity for a measurement, as seen in Chapter 6, where the S $L_{2,3}$ spectra were determined to include information from the CdTe layer beneath 20 nm and 3 nm of Au and Cu, respectively.

3.7.3 Excitons and Determining the Band Gap with XES and XAS

Because XES probes relaxations from the VB and XAS measures excitation into the CB, combining XES and XAS allows for an estimate of the electronic near-surface bulk band gap. Determination of the band gap is not straight forward, however, due to the possible presence of core- and valence-exciton states in the XAS and XES spectra.[44] Excitons occur from electron-hole pair interactions when the probed state includes a core-hole or valence-hole along with an electron in the CB. Excitons can be up to 1 eV,[45] appearing as additional states above the VBM or below the CBM. In some cases excitons can be rather pronounced and distinguishable from the spectrum, especially with the help of theoretical calculations (see, e.g., Ref. 44, 45, and references therein). This is not

always the case, especially for less defined polycrystalline systems, and as such, excitons may obscure the true VBM and CBM. The band gap determined from XES and XAS is therefore best taken as a minimum value.[46]

3.8 Beamline Description

XES and XAS measurements were performed at the Advanced Light Source (ALS) Beamline (BL) 8.0.1, at Lawrence Berkeley National Laboratory. BL 8.0.1 is equipped with a 5-cm periodic undulator, which, through the first, third, and fifth harmonics, is capable of producing x-rays from 65 – 1400 eV.[47,48] Even harmonics are excluded from the beam due to a horizontal beam defining aperture located at the top (upstream) of the beamline. The beam achieves a resolving power (E/ΔE) of 7000 with a high photon flux of 10^{11} to 6×10^{15} photons per second.[48,49]

Higher diffraction orders are also seen in the energy spectrum of the beamline, produced from constructive interference at the monochromator gratings. These higher diffraction orders result in higher energy photons in the beam. Higher order emissions add complexity to the spectra, but can be useful in some situations. An example is found in Chapter 5, when the Cu $L_{2,3}$ emission (BE ≈ 930 eV) is excited at a beamline setting of 480 eV, and appears in third-order at ~ 310 eV on the spectrometer.

3.8.1 Soft X-ray Fluorescence Endstation

Measurements in this dissertation were taken on the permanently installed Soft X-ray Fluorescence (SXF) endstation, which is equipped with a grating emission spectrometer with four interchangeable gratings and a 2D photon-counting detector, which moves relative to the exit slit along a Rowland circle, based on the photon energy

to be detected. The sample sits in the attached UHV chamber, generally at < 3 x 10^{-9} mbar.[47] The samples were often briefly exposed to air during mounting and insertion into the end station, which is acceptable for XES and XAS because of the near-surface bulk nature of the measurement.

3.9 Scanning Electron Microscopy (SEM) and Energy-dispersive X-ray Spectroscopy (EDX)

In Chapter 5 and 7, SEM and EDX are used to determine the elemental composition of the bulk and to produce images of the sample surface, respectively. The EDX measurements in Chapter 5 were performed at the University of Luxembourg, with an Oxford Instruments INCA X-MAX EDX system using a 20 kV accelerating voltage. The SEM images and EDX analysis in Chapter 7 was performed at the Helmholtz-Zentrum Berlin (HZB) on an SEM LEO Gemini 1530 system equipped with a Thermo Fischer Scientific EDX system, employing a much lower (and thus somewhat more surface sensitive) acceleration voltage of 5 kV, and a Si-drift detector.

For SEM, the image contrast is produced by the secondary electrons, which are a byproduct of the primary electron beam interacting with the sample. While the primary electron beam can penetrate hundreds of nm into the sample, the secondary electrons are of a lower KE, and thus have an escape depth, on average, below 10 nm. EDX is possible due to a secondary effect of SEM. The secondary electrons are produced when the primary electron beam removes core-level electrons from the atoms of the sample. These core-holes can then be filled radiatively in core-core transitions. The x-rays produced are energetically in the keV range, giving them a long attenuation length that enables them to

escape from their origin in the bulk for detection. Monte Carlo simulations can estimate interaction depths based on the electron beam energy and the sample properties. From this, a 5 kV electron beam has an IMFP of up to 100 nm, while a 20 kV electron beam applied to the same material will have a longer IMFP, in the range of 600 nm.[50]

3.10 References

(1) Hüfner, S. *Photoelectron Spectroscopy; Principles and Applications*; 3rd ed.; Springer, 2003.

(2) Hess, K. *Advanced Theory of Semiconductor Devices*; IEEE Press: New York, NY, 2000.

(3) Levine, I. N. *Quantum Chemistry*; 6th ed.; Pearson Prentice Hall: New Jersey, 2009.

(4) Moulder, J. F.; Stickle, W. F.; Sobol, P. E.; Bomben, K. D. *Handbook of X-ray Photoelectron Spectroscopy*; Perkin-Elmer Corporation: Minnesota, 1992.

(5) Seah, M. P. *Surf. Interface Anal.* **2001**, *31*, 721–723.

(6) Wagner, C. D.; Gale, L. H.; Raymond, R. H. *Anal. Chem.* **1979**, *51*, 466–482.

(7) Wagner, C. D.; Riggs, W. M.; Davis, L. E.; Moulder, J. F. *Handbook of X-ray Photoelectron Spectroscopy*; Perkin-Elmer Corporation: Minnesota, 1979.

(8) Atkins, P.; de Paula, J. *Atkin's Physical Chemistry*; 8th ed.; Oxford University Press: Oxford, 2006.

(9) Briggs, D.; Seah, M. P. *Practical Surface Analysis Volume I: Auger and X-ray Photoelectron Spectroscopy*; 2nd ed.; John Wiley & Sons, Ltd., 1990; Vol. 1.

(10) Friedbacher, G.; Bubert, H. *Surface and Thin Film Analysis: A Compendium of Principles, Instrumentation, and Applications*; 2nd ed.; Wiley-VCH: Weinheim, Germany, 2011.

(11) User manual for the Hemispherical Energy Analyzer Series PHOIBOS 100/150, Ver. 3.1, 2008.

(12) Wojdyr, M. *J. Appl. Crystallogr.* **2010**, *43*, 1126–1128.

(13) Shirley, D. A. *Phys. Rev. B* **1972**, *5*, 4709.

(14) Seah, M. P. In *Practical Surface Analysis*; John Wiley & Sons Ltd, 1990; Vol. 1, pp. 201–255.

(15) Scofield, J. H. *J. Electron Spectrosc. Relat. Phenom.* **1976**, *8*, 129–137.

(16) Yeh, J. J.; Lindau, I. *At. Data Nucl. Data Tables* **1985**, *32*, 1–155.

(17) Trzhaskovskaya, M. B.; Nefedov, V. I.; Yarzhemsky, V. G. *At. Data Nucl. Data Tables* **2001**, *77*, 97–159.

(18) Trzhaskovskaya, M. B.; Nikulin, V. K.; Nefedov, V. I.; Yarzhemsky, V. G. *At. Data Nucl. Data Tables* **2006**, *92*, 245–304.

(19) Seah, M. P.; Dench, W. A. *Surf. Interface Anal.* **1979**, *1*.

(20) Tanuma, S.; Powell, C. J.; Penn, D. R. *Surf. Interface Anal.* **1994**, *21*, 165–176.

(21) Tanuma, S.; Shiratori, T.; Kimura, T.; Goto, K.; Ichimura, S.; Powell, C. J. *Surf. Interface Anal.* **2005**, *37*, 833–845.

(22) Tanuma, S.; Powell, C. J.; Penn, D. R. *Surf. Interface Anal.* **2011**, *43*, 689–713.

(23) Tougaard, S. *QUASES - IMFP calculation by TPP2M formula*; Quases-Tougaard Inc., 2002.

(24) Jablonski, A. *NIST Electron Inelastic-Mean-Free-Path Database*; 2010.

(25) Lüth, H. In *Solid Surfaces, Interfaces and Thin Films*; Springer-Verlag: Berlin, Heidelberg, 2010.

(26) Schaefers, F.; Mertin, M.; Gorgoi, M. *Rev. Sci. Instrum.* **2007**, *78*, 123102.

(27) Gorgoi, M.; Svensson, S.; Schäfers, F.; Öhrwall, G.; Mertin, M.; Bressler, P.; Karis, O.; Siegbahn, H.; Sandell, A.; Rensmo, H.; Doherty, W.; Jung, C.; Braun, W.; Eberhardt, W. *Nucl. Instrum. Methods Phys. Res. Sect. Accel. Spectrometers Detect. Assoc. Equip.* **2009**, *601*, 48–53.

(28) Smith, N. V. *Rep. Prog. Phys.* **1988**, *51*, 1227–1294.

(29) Strontium Fluoride (SrF2) http://www.korth.de/index.php/162/items/33.html (accessed Aug 18, 2014).

(30) Dose, V. *Prog. Surf. Sci.* **1983**, *13*, 225–284.

(31) Weinhardt, L. Elektronenspektroskopische Untersuchungen an Grenzflächen und Oberflächen in Cu(In,Ga)(S,Se)$_2$ Dünnschichtsolarzellen. Ph.D. Dissertation, Bayerische Julius-Maximilians-Universtät Würzburg, Würzburg, Germany, 2001.

(32) Gleim, T.; Heske, C.; Umbach, E.; Schumacher, C.; Gundel, S.; Faschinger, W.; Fleszar, A.; Ammon, C.; Probst, M.; Steinrück, H.-P. *Surf. Sci.* **2003**, *531*, 77–85.

(33) Gleim, T.; Weinhardt, L.; Schmidt, T.; Fink, R.; Heske, C.; Umbach, E.; Grabs, P.; Schmidt, G.; Molenkamp, L. W.; Richter, B.; Fleszar, A.; Steinrück, H.-P. *Appl. Phys. Lett.* **2002**, *81*, 3813–3815.

(34) Eich, D.; Ortner, K.; Groh, U.; Chen, Z. H.; Becker, C. R.; Landwehr, G.; Fink, R.; Umbach, E. *Phys. Status Solidi A* **1999**, *173*, 261.

(35) Weinhardt, L.; Fuchs, O.; Groß, D.; Storch, G.; Umbach, E.; Dhere, N. G.; Kadam, A. A.; Kulkarni, S. S.; Heske, C. *Appl. Phys. Lett.* **2005**, *86*, 062109.

(36) Morkel, M.; Weinhardt, L.; Lohmüller, B.; Heske, C.; Umbach, E. *Appl. Phys. Lett.* **2001**, *79*, 4482–4484.

(37) Heske, C.; Eich, D.; Fink, R.; Umbach, E.; van Buuren, T.; Bostedt, C.; Kakar, S.; Terminello, L. J.; Grush, M. M.; Callcott, T. A.; Himpsel, F. J.; Ederer, D. L.; Perera, R. C. C.; Riedl, W.; Karg, F. *Surf. Interface Anal.* **2000**, *30*, 459–463.

(38) Weinhardt, L.; Morkel, M.; Gleim, T.; Zweigart, S.; Niesen, T. P.; Karg, F.; Heske, C.; Umbach, E. In *Proceedings of the 17th European Photovoltaic Solar Energy Conference*; Munich, 2001; p. 1261.

(39) Attwood, D. *Soft X-rays and Extreme Ultraviolet Radiation*; Cambridge University Press: New York, NY, 2007.

(40) Fuchs, O. Soft x-ray spectroscopy of organic molecules and liquids. Ph.D. Dissertation, Julius-Maximilians-Universität Würzburg, Würzburg, Germany, 2009.

(41) Pookpanratana, S. Chemical and Electronic Structure of Surfaces and Interfaces in Compound Semiconductors. Ph.D. Dissertation, University of Nevada, Las Vegas, Las Vegas, NV, 2010.

(42) Henke, B. L.; Gullikson, E. M.; Davis, J. C. *At. Data Nucl. Data Tables* **1993**, *54*, 181–342.

(43) X-Ray Attenuation Length http://henke.lbl.gov/optical_constants/atten2.html (accessed Mar 2, 2012).

(44) Weinhardt, L.; Fuchs, O.; Batchelor, M.; Bär, M.; Blum, M.; Denlinger, J. D.; Yang, W.; Schoell, A.; Reinert, F.; Umbach, E.; Heske, C. *J. Chem. Phys.* **2011**, *135*, 104705.

(45) Bechstedt, F.; Enderlein, R.; Koch, M. *Phys. Status Solidi B* **1980**, *99*, 61–70.

(46) Bär, M.; Nishiwaki, S.; Weinhardt, L.; Pookpanratana, S.; Fuchs, O.; Blum, M.; Yang, W.; Denlinger, J. D.; Shafarman, W. N.; Heske, C. *Appl. Phys. Lett.* **2008**, *93*, 244103.

(47) Jia, J. J.; Callcott, T. A.; Yurkas, J.; Ellis, A. W.; Himpsel, F. J.; Samant, M. G.; Stoehr, J.; Ederer, D. L.; Carlisle, J. A.; Hudson, E. A.; Terminello, L. J.; Shuh, D. K.; Perera, R. C. C. *Rev. Sci. Instrum.* **1995**, *66*, 4.

(48) ALS Beamline Directory. Beamline Parameters. http://www-als.lbl.gov/index/php/beamlines/beamlines-directory.html (accessed Sep 5, 2014).

(49) Beamline 8.0.1. General Beamline Information. http://www-als.lbl.gov/index/php/beamlines-directory/115-801.html (accessed Sep 5, 2014).

(50) Drouin, D.; Couture, A. R.; Joly, D.; Poirier-Demers, N.; Demers, H. *CASINO*; Universite de Sherbrooke: Sherbrooke, Quebec, Canada, 2011.

CHAPTER 4

ELECTRONIC AND CHEMICAL PROPERTIES OF INDUSTRIAL, NON-VACUUM DEPOSITED CHALCOPYRITE SOLAR CELLS

4.1 Introduction

The cost of solar cell module production, which includes the raw materials, energy, and time input, is an intimate part of the full cost-per-watt equation (with module efficiency being another fundamental component). It is therefore attractive to the solar cell industry to develop inexpensive, high-output deposition methods, which decrease the manufacturing costs without compromising the final module efficiency.

This chapter details the results of collaboration with Nanosolar, which were presented by the author at a poster session at the 37th IEEE PVSC conference, June 2011 in Seattle, WA. The text, coauthored with Nanosolar, was published in full through IEEE.[1] Nanosolar used a unique PV manufacturing method, in that their absorber was deposited through a patented "ink" based printing step using multiple alternating materials arrayed on a nanometer scale.[2] With this method, the chalcopyrite absorber could be rapidly printed in a non-vacuum chamber and onto a flexible substrate, which also allowed the deposition to be roll-to-roll. Due in part to the low production costs, in 2007 Nanosolar was slated to sell PV modules for around $1/Watt, well below the market at that time.[3] Here we investigate samples from the Nanosolar production line to learn more about the effects of ink-based deposition in a non-vacuum ambient on the chemical and electronic structure of the $Cu(In,Ga)Se_2$ absorber surface and $CdS/Cu(In,Ga)Se_2$ surface/interface.

4.2 Experimental Description

For this study, a $Cu(In_{1-x}Ga_x)Se_2$ (CIGSe) absorber and a CdS/CIGSe interface sample were taken from the Nanosolar manufacturing line. The Nanosolar process consists of an entirely non-vacuum deposition of the CIGSe layer by nanoparticle printing followed by atmospheric pressure rapid thermal processing. The process is roll-to-roll on aluminum foil substrates, and the CdS film is deposited by chemical bath deposition. After production, the samples were sealed under dry nitrogen (to avoid external surface contamination) and shipped to UNLV. The samples were unpacked in a dry-nitrogen-filled glovebox and moved directly into the UHV chamber at UNLV. For experiments at the ALS, the samples were resealed under dry nitrogen, shipped to Berkeley, and briefly exposed to air while mounting and loading them into the UHV system.

XPS, UPS and IPES were performed at UNLV employing the equipment discussed in Sections 3.2 and 3.3. To remove surface contaminants without structural damage to the surface,[4] an ion-stimulated desorption treatment[5] was employed using 50 eV Ar^+ ions, as described in Section 3.5. The ion treatments resulted in sample currents of 0.3 μA on the CIGSe absorber and 0.2 μA on the CdS/CIGSe sample. Each ion-stimulated desorption treatment was performed for up to 15 minutes, followed by detailed XPS, UPS, and IPES investigations. For the CIGSe absorber, a total of 160 minutes of ion-stimulated desorption treatments was performed.

XES was performed at the ALS, using the permanently installed SXF endstation at Beamline 8.0.1, as described in Section 3.8.

4.3 Results and Discussion

4.3.1 XPS Results

Fig. 4.1 shows XPS survey spectra for the as-received CIGSe absorber (a), the CIGSe absorber after several cycles of ion treatment (total treatment time of 160 minutes) and characterization (b), the as-received CdS/CIGSe interface sample (c), and the CdS/CIGSe structure after 15 minutes of ion treatment (d). In addition to the expected photoemission and Auger lines of Cu, In, Ga, and Se, we find Na, O, and C signals for the as-received absorber surface. The carbon signal is very low, indicating a low degree of carbon contamination (if any) during the production process and a successful transfer of the sample from Nanosolar to UNLV without significant additional contamination. In

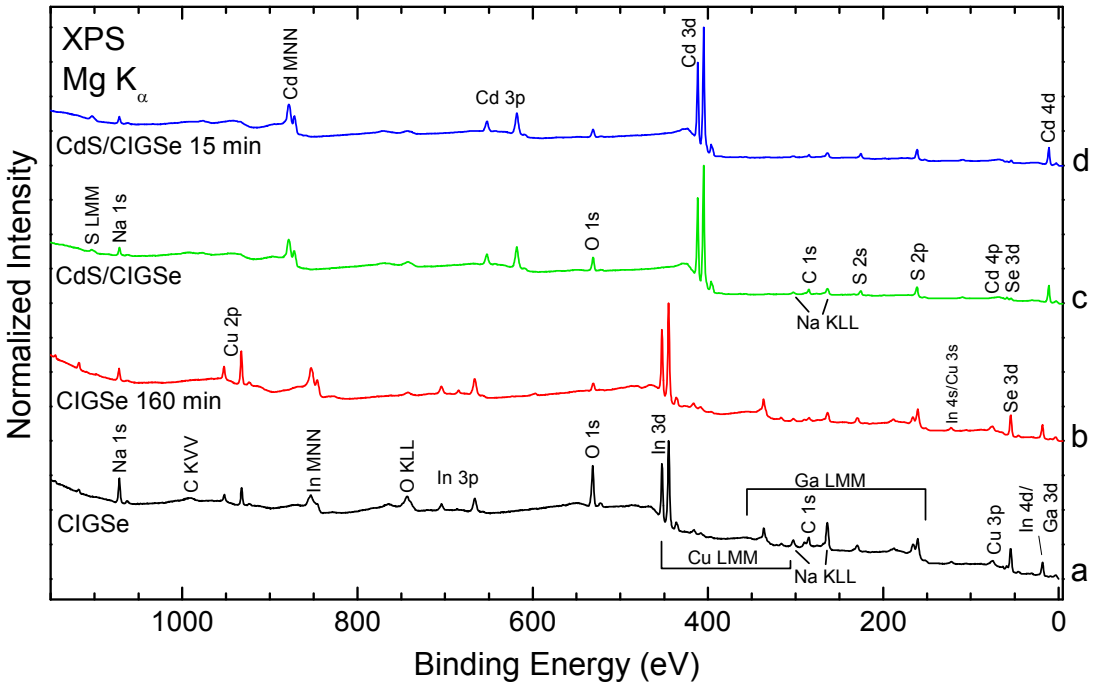

Fig. 4.1: XPS survey spectra of the CIGSe absorber before (a, black) and after (b, red) a total of 160 minutes of ion treatment. XPS survey spectra of the CdS/CIGSe sample before (c, green) and after (d, blue) 15 minutes of ion treatment.

contrast, the oxygen and sodium signals are quite large, but comparable to the surfaces of differently prepared CIGSe absorbers (for example the absorber prepared with the NREL three-stage process,[6] as shown in Ref. [7]). Both signals are strongly reduced after ion treatment, indicating that they are primarily due to surface species. The initial surface of the CdS/CIGSe interface sample exhibits the expected lines of Cd and S, and, in addition, small O, Na, C, and Se signals. Only the oxygen and carbon signals are noticeably reduced after 15 minutes of ion treatment.

The presence of a Se signal at the surface of the CdS film (and the absence of all Cu, In, and Ga signals) suggests a significant degree of S/Se intermixing at the interface, which is a typical characteristic of high-efficiency CdS/CIG(S)Se systems.[8,9] A closer look at the Se 3d detail spectra in Fig. 4.2 reveals not only the presence of Se at the CdS surface, but also indicates the formation of an oxidized Se species, which is also at the

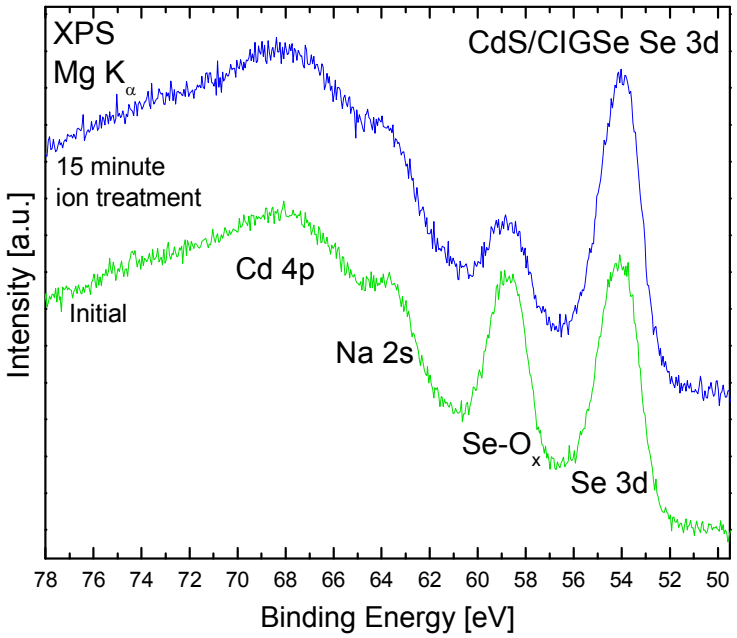

Fig. 4.2: Detailed XPS Mg K_α spectra of the Se 3d peak of the initial CdS/CIGSe sample and after 15 minutes of ion treatment.

initial surface of the CIGSe absorber before ion treatment (not shown). Earlier findings on different CIGSe absorbers also showed evidence for Se oxidation.[10] After ion treatment, the oxidized Se (Se-O_x) contribution at 59 eV is noticeably reduced for both samples.

In addition to a Se-Ox formation at the surface, we find evidence for the formation of oxidized S as well, as shown in the S 2p/Se 3p detail spectra in Fig. 4.3. Small contributions from oxidized S (S-Ox) species are present at 169 and 172 eV[11] (and not reduced after ion treatment). Weak Se $3p_{3/2}$ and $3p_{1/2}$ signals can be seen as a shoulder at 159 eV and a small peak at 166 eV, respectively,[9] while contributions from the oxidized Se species are also observed at 164 and 171 eV, 5 eV above the selenide peaks. These two peaks correspond to the oxidized Se $3p_{3/2}$ and $3p_{1/2}$ peaks, respectively, and are noticeably reduced after 15 minutes of ion treatment.

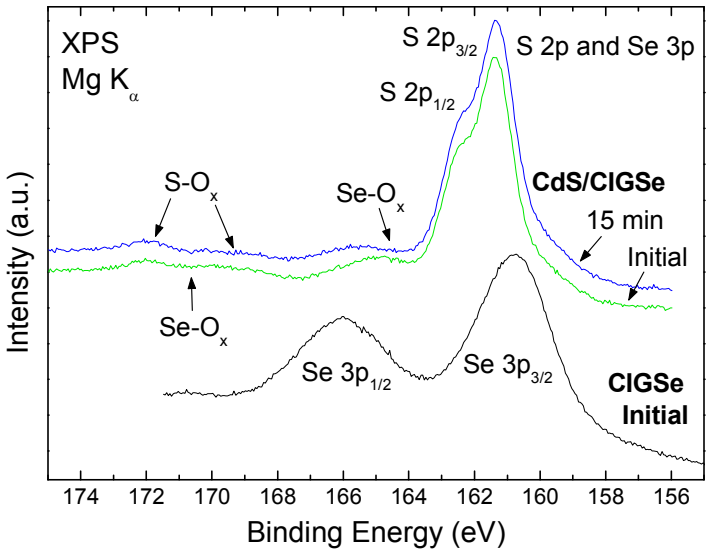

Fig. 4.3: Detailed S 2p and Se 3p XPS spectra of the initial CIGSe absorber surface and the CdS/CIGSe interface sample. In addition to the main S 2p peaks of CdS, small contributions from se 3p and Se-O_x species and contributions from S-O_x species can be seen.

4.3.2 XES Results

In addition to the surface-sensitive XPS data, XES spectra reveal quantitative information about the Cu, Na, Ga, Se, and S signals in the near-surface bulk region of both the CIGSe absorber and the CdS/CIGSe sample. Fig. 4.4 (a) presents XES data of the Cu $L_{2,3}$, Na K, Ga $L_{2,3}$, and Se $L_{2,3}$ emission using 1500 eV photon excitation, with a

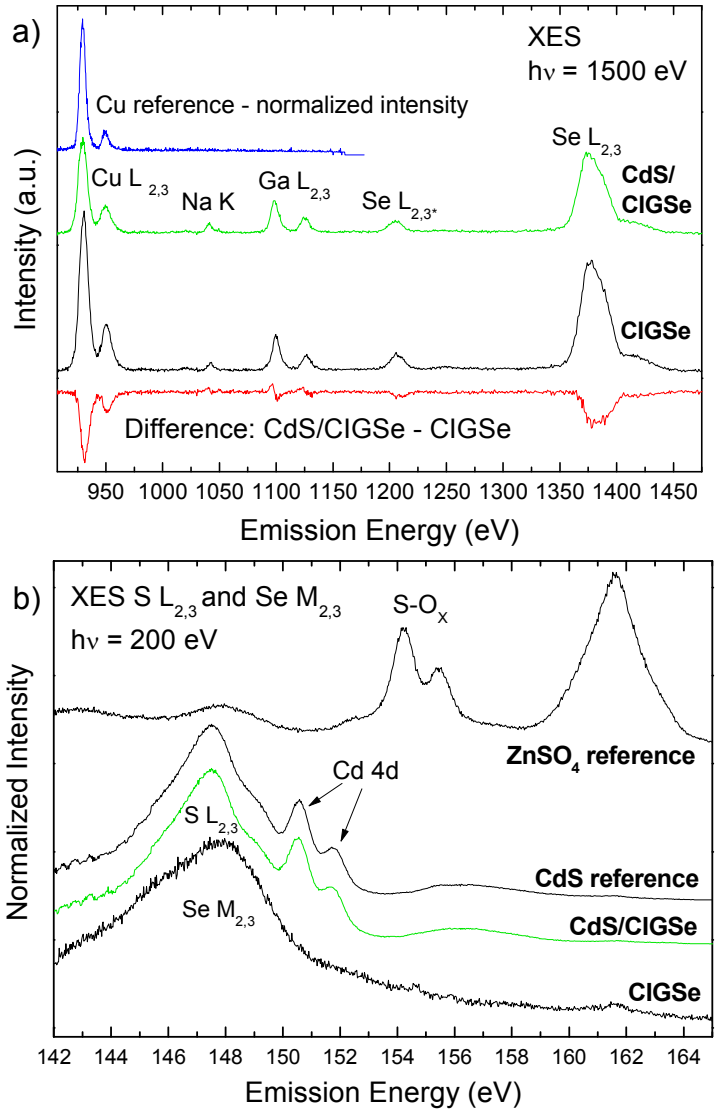

Fig. 4.4: a) Cu $L_{2,3}$, Na K, Ga $L_{2,3}$, and Se L XES spectra (1500 eV excitation energy) of the CIGSe and the CdS/CIGSe sample, together with a Cu reference; b) S $L_{2,3}$ and Se $M_{2,3}$ XES spectra (200 eV excitation energy) of CIGSe, CdS/CIGSe, and CdS and $ZnSO_4$ references.

Cu reference shown in blue at top. Subtraction of the CdS/CIGSe spectrum (green) from the CIGSe spectrum (black) yields the difference spectrum shown in red at bottom. The difference spectrum shows that the near-surface bulk region of the CdS/CIGSe interface sample gives significantly reduced Cu and Se signals as compared to the CIGSe absorber, as expected, but comparable Na and Ga signal intensities. The shape of the Ga difference spectrum (a characteristic "zig-zag" shape) suggests a small shift. The comparable Ga intensity of the two spectra very speculatively might suggest that Ga atoms migrate towards the CdS/CIGSe interface during CdS deposition. Also, the potential presence of a Cu_xSe layer at the CIGSe surface and its subsequent removal in the CdS deposition process might explain this finding, but appears even less likely.

The comparable Na signals indicate an interesting find. As discussed above, a large Na 1s XPS signal is observed for the as-received CIGSe surface, while the Na 1s signal from the CdS/CIGSe sample is significantly reduced. This surface-Na on the CdS film is thus not sufficient to explain the (more bulk-sensitive) XES finding of comparable intensities for the two samples. Thus, we conclude that a significant amount of the original CIGSe surface-Na must remain at the CdS/CIGSe interface, as found in earlier studies.[12,13]

As expected, the Cu and Se signals in Fig 4.4 (a) are noticeably weaker in the CdS/CIGSe sample compared to the CIGSe absorber due to signal attenuation in the CdS overlayer. This suggests that the XES signal contribution from Se atoms seen on the CdS/CIGSe sample surface with XPS is small compared to that of Se atoms at the CIGSe absorber surface.

Fig. 4.4 (b) shows XES spectra of the S $L_{2,3}$ and Se $M_{2,3}$ emission. Two references

were used, $ZnSO_4$ (to represent oxidized S species) and CdS. From these references, it is clear that the S in the CdS/CIGSe sample is indeed in a CdS environment. No direct evidence for a Se-contribution (from the CIGSe absorber) is found for the CdS/CIGSe spectrum, since the photoionization cross section for Se $M_{2,3}$ is substantially lower than that for S $L_{2,3}$ (note that the spectra in Fig. 4.4 (b) were scaled to maximum peak height). The lower cross section of the Se $M_{2,3}$ photoionization is evident in the lower signal-to-noise ratio of the CIGSe spectrum.

In addition to the analysis of the chemical surface and interface properties, we have used UPS and IPES to derive the electronic surface structure of the two samples, before and after ion treatment. Surface contaminants can artificially widen the observed surface band gap (E_g),[14] and thus a cleaning process is needed to measure the true E_g.

However, standard cleaning treatments based on (high-energy) ion sputtering produce changes in the stoichiometry of the surface and create metallic features at the surface (e.g., a Fermi edge[15]). Thus, we employed ion stimulated desorption ("ion treatment"), as described in the experimental section, to clean the sample surfaces in short 5 to 15 minute steps using 50 eV Ar^+ ions. Detailed XPS, UPS, and IPES data were taken after each step to monitor for metallic features.

Fig. 4.5 shows UPS and IPES data of the CIGSe absorber (a) and the CdS/CIGSe interface sample (b) before and after different ion treatment steps. The UPS spectra, indicative of the VB density-of-states and, in particular, the VBM, are shown on the left. The IPES spectra on the right reflect the density-of-states of the unoccupied (conduction) states and, in particular, the position of the CBM. Both spectra are shown on a common energy scale relative to E_F, which was determined using a clean Au foil reference.

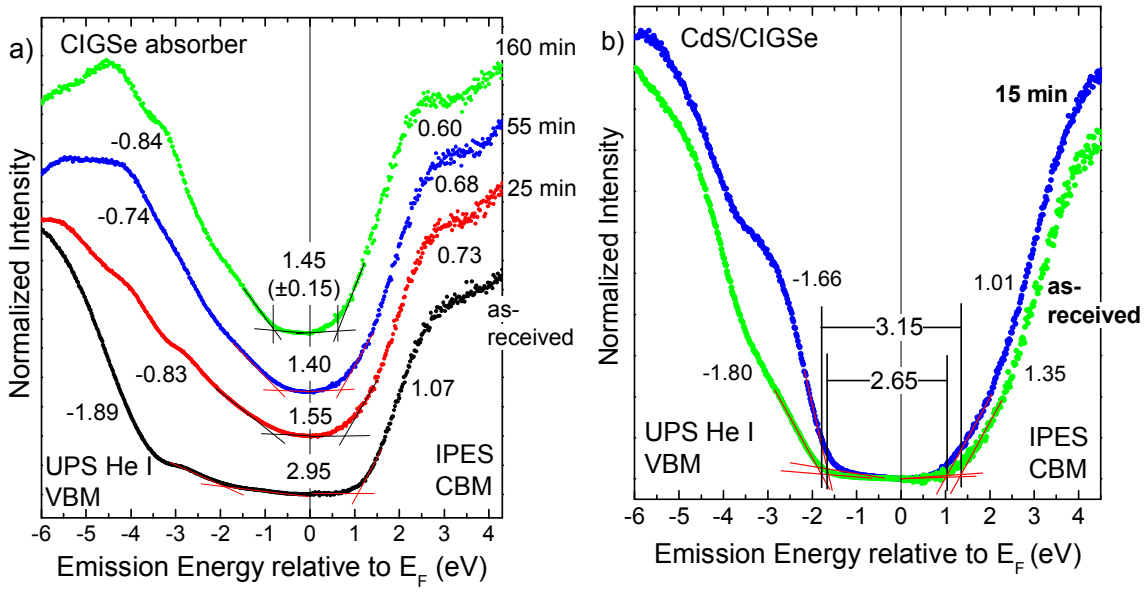

Fig. 4.5: UPS and IPES data of (a) the as-received CIGSe and after 25, 55, and 160 minutes of ion treatment and (b) the as-received CdS/CIGSe interface sample and after 15 minutes of ion treatment. The energy scale is given relative to E_F, and band edges are determined by a linear extrapolation. The energy separation between VBM and E_F (e.g., -0.84 eV for the clean CIGSe) and between CBM and E_F (e.g., 0.60 eV for the clean CIGSe) are listed. The electronic surface E_g for the clean CIGSe absorber is determined to (1.45 ± 0.15) eV (all gap values are rounded to the nearest 0.05 eV and the VBM and CBM positions have an error bar of 0.10 eV).

Combining the UPS and IPES spectra on a common energy scale allows us to determine the electronic surface E_g of the samples using linear extrapolation of the leading edges,[16] as well as the position of E_F within the E_g at the surface.

The E_g of the as-received CIGSe absorber (bottom) shown in Fig. 4.5 (a) is (2.95 ± 0.15) eV. The removal of surface contaminants using successive ion treatments leads to an increase in the spectral weight around -3 eV below E_F (i.e., the spectral region of the Cu 3d bands). Also, the leading edge becomes more pronounced, making a determination of the VBM more reliable. Similarly, the CB onset also shifts with successive ion treatments, leading to a lower CBM position for the cleaned surface. After 160 minutes of

cleaning (leading to a significant reduction of O and C surface contaminants, as seen in Fig. 4.1), a surface E_g of (1.45 ± 0.15) eV is found, which is similar to that of high-efficiency CIGSe absorber solar cells.[15,17] The E_F is found to be slightly above mid-gap (i.e., closer to the CBM).

Fig. 4.5 (b) shows the electronic surface band gap of the CdS/CIGSe interface sample before (black) and after (red) 15 minutes of ion treatment. Again, a reduction in the electronic E_g is observed after surface cleaning (i.e., with reduced O and C surface content, as seen in Fig. 4.1). The surface E_g after ion treatment is found to be (2.65 ± 0.15) eV. This is slightly larger than the bulk and surface E_g of CdS frequently observed (2.4 – 2.5 eV[5]), but might easily depend on the concentration of hydroxide contributions to the CdS matrix. As with the CIGSe absorber, the E_F of the CdS/CIGSe sample is closer to the CBM than the VBM.

As has been repeatedly observed for high-efficiency CIGSe-based thin film solar cells,[14,15,17] the electronic E_g at the absorber surface is larger than the corresponding optical bulk E_g. As discussed in various publications of the CIGSe community (initiated with Refs. [18] and [19]), this is presumably due to the fact that the CIGSe surface is Cu-poor and In-rich, leading to a different stoichiometry and electronic structure in the near-surface region. We also note that the position of the E_F within the E_g indicates a slightly n-type character at the absorber surface.

4.4 Conclusion

We have investigated the chemical and electronic surface properties of a bare CIGSe absorber and a CdS/CIGSe interface sample taken directly from the Nanosolar

manufacturing line. XPS and XES were used to determine surface and near-surface bulk chemical composition, while UPS and IPES were used to determine the surface electronic E_g and other properties such as the location of the E_F within the E_g. Although the samples were produced using a low-cost industrial process, they show a remarkably low degree of C and O surface contamination. Our data shows evidence for S/Se intermixing at the CdS/CIGSe interface, as observed earlier for other high-efficiency CIGSe systems. Also, it indicates that Na atoms, localized at the CIGSe surface, are retained at the interface upon formation of the CdS/CIGSe junction. The electronic surface E_g of both samples were determined before and after sample cleaning - the E_g of the CIGSe absorber surface was determined to (1.45 ± 0.15) eV, and the surface E_g of the CdS/CIGSe interface sample was derived to be (2.65 ± 0.15) eV. From the location of the E_F, both samples show a slightly n-type character at the sample surface.

4.5 References

(1) Horsley, K.; Pookpanratana, S.; Krause, S.; Hofmann, T.; Blum, M.; Weinhardt, L.; Bar, M.; George, K.; Van Duren, J.; Jackrel, D.; Heske, C. In *2011 37th IEEE Photovoltaic Specialists Conference (PVSC)*; 2011; pp. 000374–000378.

(2) Sager, B. M.; Roscheisen, M. R. Nano-architected/assembled solar electricity cell. 6852920, December 11, 2002.

(3) Markoff, J. Start-Up Sells Solar Panels at Lower-Than-Usual Cost. *The New York Times*, 2007.

(4) Heske, C.; Fink, R.; Umbach, E.; Riedl, W.; Karg, F. *Cryst. Resolut. Technol.* **1996**, *31*, 919–922.

(5) Weinhardt, L.; Fuchs, O.; Groß, D.; Storch, G.; Umbach, E.; Dhere, N. G.; Kadam, A. A.; Kulkarni, S. S.; Heske, C. *Appl. Phys. Lett.* **2005**, *86*, 062109.

(6) Contreras, M. A.; Egaas, B.; Ramanathan, K.; Hiltner, J.; Swartzlander, A.; Hasoon, F.; Noufi, R. *Prog. Photovolt. Res. Appl.* **1999**, *7*, 311–316.

(7) Weinhardt, L.; Blum, M.; Bär, M.; Heske, C.; Fuchs, O.; Umbach, E.; Denlinger, J. D.; Ramanathan, K.; Noufi, R. *Thin Solid Films* **2007**, *515*, 6119–6122.

(8) Heske, C.; Eich, D.; Fink, R.; Umbach, E.; van Buuren, T.; Bostedt, C.; Terminello, L. J.; Kakar, S.; Grush, M. M.; Callcott, T. A.; Himpsel, F. J.; Ederer, D. L.; Perera, R. C. C.; Riedl, W.; Karg, F. *Appl. Phys. Lett.* **1999**, *74*, 1451–1453.

(9) Weinhardt, L.; Bär, M.; Pookpanratana, S.; Morkel, M.; Niesen, T. P.; Karg, F.; Ramanathan, K.; Contreras, M. A.; Noufi, R.; Umbach, E.; Heske, C. *Appl. Phys. Lett.* **2010**, *96*, 182102.

(10) Heske, C.; Fink, R.; Umbach, E.; Riedl, W.; Karg, F. *Appl. Phys. Lett.* **1996**, *68*, 3431–3433.

(11) Weinhardt, L.; Morkel, M.; Gleim, T.; Zweigart, S.; Niesen, T. P.; Karg, F.; Heske, C.; Umbach, E. In *Proceedings of the 17th European Photovoltaic Solar Energy Conference*; Munich, 2001; p. 1261.

(12) Heske, C.; Eich, D.; Fink, R.; Umbach, E.; Kakar, S.; Buuren, T. van; Bostedt, C.; Terminello, L. J.; Grush, M. M.; Callcott, T. A.; Himpsel, F. J.; Ederer, D. L.; Perera, R. C. C.; Riedl, W.; Karg, F. *Appl. Phys. Lett.* **1999**, *75*, 2082–2084.

(13) Heske, C.; Eich, D.; Fink, R.; Umbach, E.; van Buuren, T.; Bostedt, C.; Kakar, S.; Terminello, L. J.; Grush, M. M.; Callcott, T. A.; Himpsel, F. J.; Ederer, D. L.; Perera, R. C. C.; Riedl, W.; Karg, F. *Surf. Interface Anal.* **2000**, *30*, 459–463.

(14) Bär, M.; Nishiwaki, S.; Weinhardt, L.; Pookpanratana, S.; Shafarman, W. N.; Heske, C. *Appl. Phys. Lett.* **2008**, *93*, 042110.

(15) Morkel, M.; Weinhardt, L.; Lohmüller, B.; Heske, C.; Umbach, E. *Appl. Phys. Lett.* **2001**, *79*, 4482–4484.

(16) Gleim, T.; Heske, C.; Umbach, E.; Schumacher, C.; Gundel, S.; Faschinger, W.; Fleszar, A.; Ammon, C.; Probst, M.; Steinrück, H.-P. *Surf. Sci.* **2003**, *531*, 77–85.

(17) Bär, M.; Repins, I.; Contreras, M. A.; Weinhardt, L.; Noufi, R.; Heske, C. *Appl. Phys. Lett.* **2009**, *95*, 052106.

(18) Schmid, D.; Ruckh, M.; Grunwald, F.; Schock, H. W. *J. Appl. Phys.* **1993**, *73*, 2902–2909.

(19) Schmid, D.; Ruckh, M.; Schock, H.-W. *Sol. Energy Mater. Sol. Cells* **1996**, *41/42*, 281–294.

CHAPTER 5

Cu-RICH $CuInSe_2$ ABSORBERS WITH A Cu-POOR SURFACE

5.1 Introduction

As discussed in Chapter 2, CIGSe absorbers are typically grown with a Cu-poor stoichiometry, which has repeatedly produced solar cells with efficiencies of over 20 %.[1–3] Cu-poor growth of the absorber has been shown to produce a surface with a Cu content much lower than the bulk. This Cu-deficient surface has been described as an ordered defect compound (ODC), with a wider band gap (~1.3 eV) than the bulk stoichiometric $CuInSe_2$ (~1.0 eV)[4–6] up to 200 nm in from the surface[7]. This widened surface band gap is credited for the reduced recombination seen at the buffer/$CuInSe_2$ interface of Cu-poor CISe absorbers, relative to their Cu-rich counterparts.[8,9] Cu-poor absorbers, however, also exhibit smaller grain formation[10] and large defect concentrations in the bulk, which lead to the domination of bulk recombination in these materials.[11] Growing CISe absorbers in Cu-excess, on the other hand, produces a stoichiometric $CuInSe_2$ with reduced defects in the bulk, leading to a higher crystallinity compound and thus larger grain formation.[10,12] The reduced defects work to lower the bulk recombination, and improve charge-carrier transport properties of the absorber. With Cu-rich grown CISe absorbers, however, it is difficult to reach device efficiencies even over 10%. This is attributed, in part, to increased recombination at the buffer/absorber interface due to the absence of the beneficial ODC seen in Cu-poor absorbers.[13] A metallic $Cu_{2-x}Se$ phase is also observed at the surface and grain boundaries,[10] which may further be detrimental to charge transport. More recently, the elevated doping level found for Cu-rich chalcopyrite relative to Cu-poor has also been discussed as a possible cause

for poor efficiencies. A sufficiently high doping level would lead to steep band bending at the space charge region in the absorber, and cause tunneling-induced recombination.[13,14]

It is therefore the aim of this study to investigate the possibility of growing a CIGSe absorber in Cu-excess (i.e., with a Cu-rich bulk), but with a surface similar to that seen for Cu-poor absorbers. In this way, the large grains and reduced defects characteristic of the Cu-rich bulk can be combined with the widened band gap and lower doping level characteristic of the Cu-poor surface, and increased efficiencies for $Cu(In,Ga)Se_2$ absorber materials may be achieved.

To this end, a sample set was prepared at the University of Luxembourg of $CuInSe_2$ absorbers (omitting Ga to simplify the system), which included two co-evaporated absorbers grown Cu-poor and Cu-rich, and a Cu-rich absorber which had undergone a KCN etch and final In/Se surface deposition at elevated temperature to produce a Cu-poor surface. Positive results have already been produced from these Cu-rich / Cu-poor absorbers, and efficiencies just shy of traditionally-grown Cu-poor sibling absorbers have been achieved.[14,15] This design of absorber deposition has not been previously investigated.

This study was developed and conducted in close collaboration with the group of Prof. Susanne Siebentritt at the University of Luxembourg and Prof. Marcus Bär at the HZB. The research performed at the HZB was supported by a DAAD RISE internship through which the author was hosted by Prof. Bär and his research group. A portion of the data shown here was presented in a talk at the Spring MRS in San Francisco, CA, April 2, 2013.

5.2 Sample Description and Experimental Set-up

The $CuInSe_2$ absorbers were grown by Physical Vapor Deposition (PVD) by Valerie Depredurand at the University of Luxembourg. All of the samples were deposited on Mo-coated 3 mm soda-lime glass substrates manufactured by Saint Gobain. The as-received Mo surface was cleaned in an ionic bath with Decon 5% followed by a rinse with ethanol, prior to absorber deposition. One absorber was deposited similar to the NREL 3-step process,[16] in which the first step co-evaporation of In and Se was performed at 350-400 °C, and the second and third step evaporations of Cu and Se, and then In and Se were both performed at an increased substrate temperature of 500-550 °C. This produced an absorber with a Cu/In ratio of 0.91 ± 0.03, as determined by EDX using a 20 kV accelerating voltage. This absorber is here-on designated "Cu Poor". A second absorber design was followed, in which Cu, In, and Se were deposited together in a 1 step co-evaporation at 540 °C. This produced an absorber with a Cu/In ratio of 1.07 ± 0.03, which is labeled "Cu Rich". A second "Cu Rich" absorber was further treated by a 5 minute etch with a 10 wt% KCN solution followed by a de-ionized (DI) water rinse, and then reintroduced into the PVD chamber for a final 1 minute In and Se deposition at 275 °C. This produced an absorber with an overall Cu/In ratio of 0.99 ± 0.03, which is designated as "In-Se Treated". See Table 5.1 for concise summary of all samples.

The prepared absorbers were removed from the PVD chamber without air exposure, sealed under an inert environment, and shipped to the HZB, where they were unpacked in a N_2 filled glovebox for subsequent introduction into UHV for analysis. The "Cu Rich" sample was broken in half and one portion was removed to air to perform the 5 minute 10 wt% KCN etch at the HZB, similar to the etch performed at the University of

Table 5.1: $CuInSe_2$ absorber sample descriptions

Sample Designation	Absorber Deposition	KCN etch	Final In/Se dep.	Cu/In ratio (EDX ± 0.03)	Final Efficiency	Record Efficiency[15]
Cu Poor	NREL 3-step	--	--	0.91	10.2	13.5
Cu Rich	1 step at 540 °C	--	--	1.07	--	--
Cu Rich Etched	1 step at 540 °C	Yes	--	1.06	7.1	9.5*
In-Se Treated	1 step at 540 °C	Yes	Yes	0.99	8.8	13.1*

[15]V. Depredurand, Y. Aida, J. Larsen, T. Eisenbarth, A. Majerus, and S. Siebentritt, in *2011 37th IEEE Photovolt. Spec. Conf. PVSC* (2011), pp. 000337–000342.

* Cu Rich Etched and In Se Treated record efficiencies achieved with a bulk Cu/In ratio of 1.56 and 1.41, respectively, compared to 1.07 for this sample.

Luxembourg. The sample was rinsed and submersed in DI water, then reintroduced into the N_2-filled glovebox without air exposure. This sample is designated "Cu Rich Etched". A similarly etched "Cu Rich" sample from the same batch at the University of Luxembourg had a Cu/In ratio of 1.06 ± 0.03. Table 5.1 lists the four absorber samples, the treatment steps, and the Cu/In ratios of sibling samples determined by EDX, along with the conversion efficiency of the resulting solar cells and the maximum efficiency achieved to date for each absorber design.

Initial XPS measurements were performed on all samples at the HZB, after which a small piece of each sample was broken off, and both sets were sealed in separate packages under a N_2 environment. The smaller portions were taken to the BESSY II synchrotron for HAXPES, while the remainder of each sample was shipped to UNLV. At BESSY II, the samples were mounted with clean Au foil references and introduced into the UHV analysis system without air exposure.

After baseline measurements at UNLV of XPS, UPS, and IPES, a series of low-energy 50 eV Ar^+ ion treatments were performed, as described in Section 3.5 and Ref. 17, to remove adventitious surface adsorbates and more accurately determine the element ratios and surface E_g for the pristine sample surface. XPS, UPS and IPES were performed after each step of the cleaning treatment to monitor the removal of adsorbates and check for any other changes to the sample surface (e.g., metallic states[18]). At UNLV, additional small pieces were broken off of each sample and taken to the ALS for XES and XAS measurements. The samples were briefly exposed to air while mounting and introducing them into the UHV analysis system. Description of the measurement techniques and equipment used can be found in Chapter 3, Sections 3.2, 3.3, and 3.8.

5.3 Results and Discussion

5.3.1 Surface Stoichiometry and Band Gap

The XPS Mg K_α surveys of all four samples are shown in Fig. 5.1. The expected peaks of Cu, In and Se are present on all sample surfaces, along with small C and O signals, expected to be from adventitious adsorbates. A Na signal is also seen on the "Cu Poor", "Cu Rich" and "In-Se Treated" samples, which is known to diffuse from the soda-lime glass substrate and reside at the surface and grain boundaries of the film.[19,20]

The "Cu Rich" sample shows increased Cu and C signals, decreased In and Na signals, and no discernable change in Se intensity relative to the "Cu Poor". The changes are most easily seen from the Cu 2p (~950 eV), Na 1s (~1070 eV), In 3d (~450 eV), and C 1s (~285 eV) peaks. Comparisons of high BE (low KE) peaks (i.e. Cu 2p and Na 1s) must be done with care since the lower energy of the electrons results in a shallower

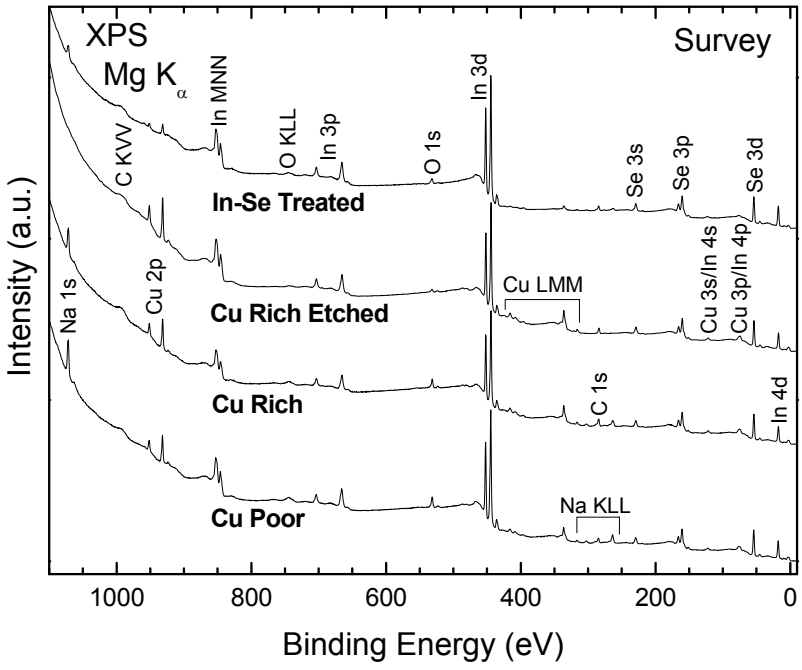

Fig 5.1: Initial XPS Mg K_α survey spectra of the four $CuInSe_2$ absorbers.

escape depth and thus a higher sensitivity to surface adsorbates (i.e., the increased C 1s signal). However, the Cu 3p (~76 eV) and Na KLL (~300 eV) peaks at a significantly lower BE show intensity changes relative to the "Cu Poor" sample which support the previously stated decrease in Na and increase in Cu.

A Na signal is not distinguishable from the survey of the "Cu Rich Etched" sample, showing the KCN etch to remove most if not all of the Na from the surface. The O 1s (~530 eV) is strongly reduced, and some reduction in the C 1s peak is also seen, indicating a removal of surface adsorbates. The Cu 2p, In MNN, and In 3d signals are much stronger for the "Etched" sample. However, the strong reduction in O 1s intensity means that these changes to high BE peaks could be attributable to a removal of surface adsorbates. Only a small increase in the In 4d is seen when the lower BE peaks are

compared, and thus no firm statement can be made about a change in surface Cu, In or Se after the KCN etch based on the survey spectra.

The "In-Se Treated" surface shows a greatly reduced Cu signal and increased In signal compared to both the "Cu Rich" and "Cu Poor" samples, while there is no significant change in the Se 3p (~165 eV) or 3d (~55 eV) intensity. Some Na signal is also seen to have returned to the surface after the final In-Se deposition at 275 °C, though the signal is much lower than that from the "Cu Poor" and "Cu Rich" samples. After removal from the surface, Na has been shown to return to the CIGSe surface both with time in vacuum and after annealing.[20]

The XPS survey spectra and UPS and IPES measurements taken at UNLV on all samples after 30 minutes of ion treatment (35 minutes for the "Cu Rich Etched" sample) are shown in Fig. 5.2 (band gap data is not available for the "Cu Rich Etched" sample). While subsequent ion treatments were performed, the data after ~ 30 minutes of ion treatment gave the most efficient cleaning of the samples with the least potential disturbance to the surface and no subsequent changes to the band gap values were seen.

From the XPS survey spectra of the four cleaned samples, shown in Fig. 5.2 (a), we see that the ion treatment was successful in removing the majority of the surface O signal from all samples. The C signal is reduced but still present for the "Cu Poor", "Cu Rich", and "Cu Rich Etched" sample surfaces, as seen from the C 1s peak at ~285 eV and the C KVV at ~1000 eV. A stronger C signal is present on the "In-Se Treated" sample relative to the other samples, which was not reduced with ion treatment. The absorber peaks of Cu, In, and Se all increased with ion treatment time. A small Cl peak is found on the "Cu Rich" sample, most likely from external contamination during packing. The Na

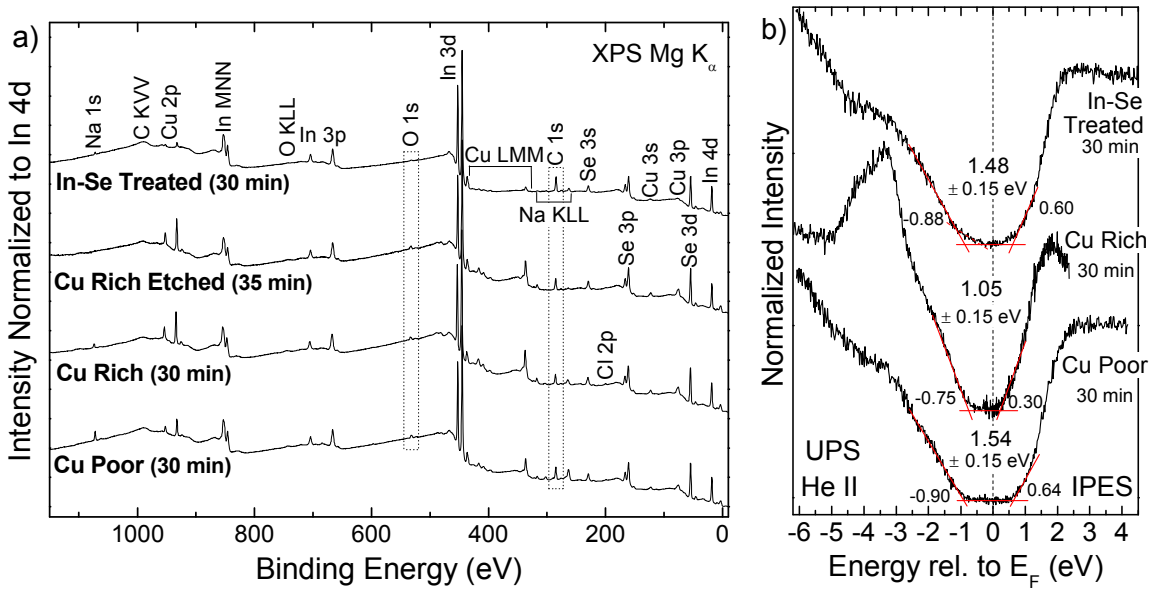

Fig.5.2: a) Mg K_α XPS survey spectra normalized to the In 4d peak intensity of all four samples after 30 minutes of 50 eV Ar^+ ion treatment (35 for the "Cu Rich Etched" sample). b) The corresponding UPS and IPES spectra showing the surface E_g of the "Cu Poor, "In-Se Treated", and "Cu Rich" samples after 30 minutes of ion treatment.

signals on all samples were reduced after each ion treatment, but the relative intensities between samples is maintained. The variation in the surface Cu intensity between samples is also maintained.

A significant variation in the surface E_g is seen for all three samples, as shown in Fig. 5.2 (b). The "Cu Poor" sample (bottom) has a surface E_g of 1.54 ± 0.15 eV, with the E_F slightly right of center between the VBM (-0.90 eV) and the CBM (0.64 eV). The "Cu Rich" sample shows a much smaller surface E_g of 1.05 ± 0.15 eV, with both the VBM (-0.75) and CBM (0.30) shifted in towards the E_F significantly compared to the "Cu Poor" sample. The "In-Se Treated" sample has a surface E_g of 1.48 ± 0.15 eV and VBM (-0.88 eV) and CBM (0.60 eV) positions comparable to that of the "Cu Poor" sample, despite the strong reduction in Cu content seen at the surface. We note an added intensity above

the VBM in the UPS spectrum for this sample. If this shoulder is taken to be the "true" VBM of the surface, an extrapolated VBM value of -0.40 eV is measured, leading to a much smaller E_g of 1.00 ± 0.15 eV. This low-intensity shoulder could be indicative of Cu-vacancies, which, in the bulk, create shallow acceptor states,[12] or the presence of a second phase at the surface, such as an indium selenide, with a higher VBM. Further evaluation of these E_g values is continued after determination of the surface stoichiometry.

The surface Cu:In:Se ratios were determined for all four samples from the Cu 3p, Se 3d, and In 4d peaks, which were measured together and are shown in Fig. 5.3 a). All spectra were taken after 30 minutes of ion treatment cleaning (35 minutes for the "Cu Rich Etched" sample), and are normalized to the In 4d peak intensity. These peaks were chosen due to their proximity to one another, which minimizes any auxiliary changes in peak intensity due to variation in the transmission function of the analyzer, changes in the electron escape depth (for electrons of 1150-1250 eV KE, the IMFP through $CuInSe_2$ is ~ 5 nm), and variations in attenuation from any remaining surface adsorbates.

The fits of the Cu 3p, Se 3d, and In 4d regions are shown in Fig. 5.3 b) along with the residual below each fit, which was multiplied by the factor given in the figure. The fits of each region are shown with the same relative scaling of the y-axis for each respective box, such that variations in peak intensity can be seen. A linear background and Voigt peak shape was used for all peaks. Additional broadening is present for the measurements taken on the "Cu Poor" and "In-Se Treated" samples, due to the use of a higher Pass Energy for the electron analyzer (see, for example, the shape of the Se 3d peak on the "Cu Rich Etched" sample compared to the "In-Se Treated" sample). Usually

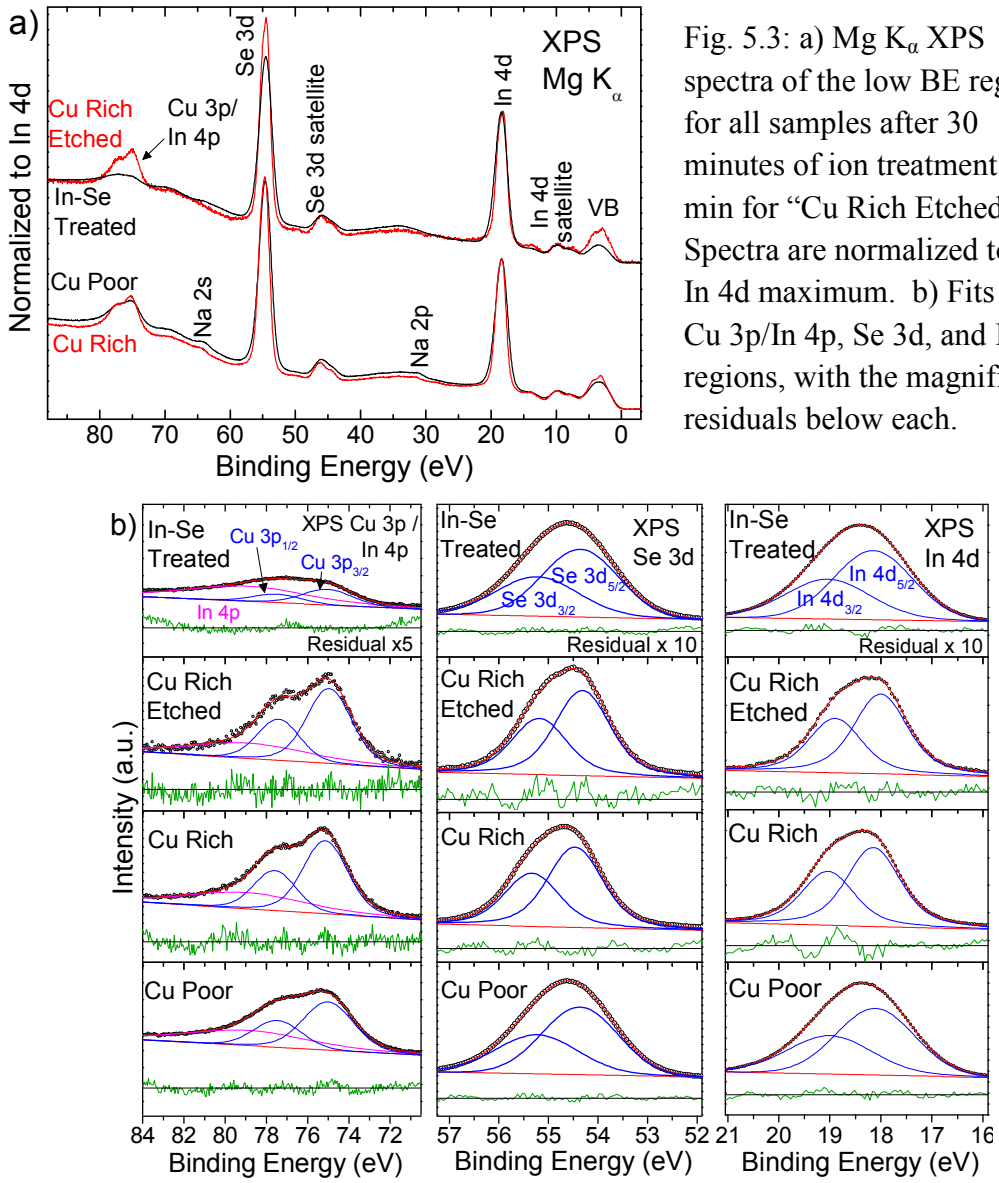

Fig. 5.3: a) Mg K_α XPS spectra of the low BE region for all samples after 30 minutes of ion treatment (35 min for "Cu Rich Etched"). Spectra are normalized to the In 4d maximum. b) Fits of the Cu 3p/In 4p, Se 3d, and In 4d regions, with the magnified residuals below each.

the same Gaussian and Lorentzian broadening would be used for all peaks of a given subshell, since they would be expect to share the same core hole lifetime and electron analyzer settings. With the analyzer settings changed between measurements, a good fit of the data could not be achieved by setting the Gaussian and Lorentzian broadening of the peaks from all samples equal to one another. Thus, for each set of similarly measured samples ("Cu Poor" / "In-Se Treated" and "Cu Rich" / "Cu Rich Etched"), the Gaussian

broadening was held constant for all peaks of a given element and the Lorentzian broadening was held constant for each split-peak component (e.g., all In $4d_{3/2}$ and $4d_{5/2}$ peaks used to fit the "Cu Poor" and "In-Se Treated" spectra share the same Gaussian broadening, but only the In $4d_{3/2}$ peaks share the same Lorentzian broadening). This gave a robust description of the data for all peaks except for the case of the Se 3d, for which the broadening and shape was not consistent between the "Cu Poor" and "In-Se Treated" samples. The same peak shape was only sufficient to describe both spectra if *two* sets of Se 3d peaks were used to fit the "In-Se Treated" sample data. However, no variation in peak shape or location is seen for the Se LMM between samples (not shown), and thus the validity of a two-component fit is not well founded. For the fits as shown, the Lorentzian broadening of the Se 3d was not paired for the "Cu Poor" and "In-Se Treated" spectra, to allow the best description of the data with only one Se-species, and thus the most accurate determination of peak area.

The Cu 3p/In 4p region (Fig. 5.3 (b), left) was fit with three peaks – the In 4p, as measured from a clean In foil and scaled to the intensity of the In 4d peak, and the Cu $3p_{1/2}$ and $3p_{3/2}$ peaks. The area ratio of the Cu 3p peaks was set to 1:2 and the spin-orbit splitting of the Cu 3p peaks was set to 2.4 eV[21] as a starting point. The peaks were then allowed to vary slightly to best fit the data, which was achieved at 2.46 eV. The area of the In 4p peak was also allowed to vary by up to 7%, which was based on the variation in In 4d peak *area* after normalizing all spectra to the In 4d peak *height*. The Se 3d and In 4d doublets (Fig. 5.3 (b), center and right) were given a fixed separation following a procedure similar to that for the Cu 3p (0.87 and 0.89 eV, respectively, compared to 0.9 and 0.8 eV as listed in Ref. 22), and a fixed area ratio of 2:3. The area of each peak, as

Table 5.2: Surface Cu/In and Se/(Cu+In) ratios for all four $CuInSe_2$ samples, as determined from the fits of the Cu 3p, In 4d and Se 3d XPS peaks.

	XPS		EDX
Sample	**Cu/In (±0.05)**	**Se/(Cu+In) (±0.05)**	**Cu/In (±0.03)**
Cu Poor	0.34	0.93	0.91
Cu Rich	0.48	0.87	1.07
Cu Rich Etched	0.48	0.91	1.06
In-Se Treated	0.11	1.06	0.99

determined from the fit of the data, was then divided by the cross section of the respective subshell[23] to correct for the excitation probability. The resulting surface Cu/In and Se/In ratios are shown in Table 5.2, along with the bulk Cu/In ratios determined from EDX.

From an overview of the Cu/In and Se/(Cu+In) ratios, we find all sample surfaces to be In-rich (note that the sample names focus on Cu and the Cu content of each sample relative to the others, and not necessarily the overall stoichiometry). The "Cu Rich" and "Cu Rich Etched" samples have the highest surface Cu/In ratios of 0.48 ± 0.05, followed by the "Cu Poor" sample at 0.34 ± 0.05. In comparison, the "In-Se Treated" sample surface is extremely Cu-depleted, with a Cu/In ratio of 0.11 ± 0.05.

The extremely low Cu/In ratio at the "In-Se Treated" sample surface compared to the almost stoichiometric bulk Cu/In ratio of 0.99 (which includes the Cu-poor surface) suggests that the bulk is maintained as Cu-rich in the final absorber. The surface Cu/In ratio of the "In-Se Treated" sample is only $^1/_3$ that of the "Cu Poor" sample. Even with this strong variation, however, the surface VBM spectra and extrapolated E_g values for these two samples match each other very well (Fig. 5.2). This may be related to the

stability of $CuInSe_2$ compounds through such a high range of stoichiometries, and the ability for multiple defects working in combination to become electrically inactive.[12] This would suggest that a comparable band gap can be achieved for surface Cu/In ratios varying between ~ 0.1 and 0.3, while a sudden change in the surface E_g is seen for a Cu/In ratio above 0.4. The Cu-deficiency at the "In-Se Treated" sample surface and the comparable E_g value to the "Cu Poor" sample shows a success in the growth of the "In-Se Treated" absorber, and could explain the comparable efficiencies achieved between these two absorber designs.

The surface Cu/In and Se/(Cu+In) ratios for the "Cu Poor" sample match well to literature values. $CuInSe_2$ absorbers with a bulk Cu/In ratio of ~ 0.9 have been investigated previously by Niemi,[24] Schulmeyer,[6] and Schmid,[4] and found to have surface Cu/In ratios from 0.38 to 0.40. The surface VBM values reported by Schulmeyer (0.8 eV) and Schmid (slightly larger than 1 eV) for these samples also match well to the VBM of the "Cu Poor" sample of 0.90 eV. We note that the surface Cu/In ratios determined by XPS are surprisingly consistent for all of these samples, despite variations in sample preparation (single-crystal $CuInSe_2$ with In-Se deposition,[6] and co-evaporated polycrystalline $CuInSe_2$[4,24]). This suggests a general stability in the surface Cu/In ratio of Cu-poor samples, as seen by Schmid et al.[4]

While the "Cu Rich" sample has the highest surface Cu/In ratio of all the samples, it is unexpectedly low for a sample with a bulk Cu/In ratio over 1. For Cu-rich grown absorbers, a $Cu_{2-x}Se$ phase is expected at the surface and grain boundaries,[10] which results in a surface Cu/In ratio above 1 for absorbers with a bulk Cu/In ratio above 1 or even slightly below.[4] One example from literature which does not follow this trend (and

thus matches more closely with our results) is present in the study by Niemi et al., where a stoichiometric bulk deposition (Cu/In = 0.99) resulted in a slightly Cu-poor surface (Cu/In = 0.68) as determined by XPS.[24] Only the samples with a bulk Cu/In ratio significantly over 1 in this study (e.g., 1.23 and 1.57) exhibited a surface Cu/In ratio also over 1. However, the surface Cu/In ratio of 0.48 for the "Cu Rich" sample is still significantly lower. This surface Cu depletion similar to Cu-poor samples is in contrast to both the poor solar cell efficiency (7.7 %, Table 5.1) and the significantly narrowed surface E_g (Fig. 5.2 (b)), both of which match the expectations for a typical, Cu-rich grown absorber. The low surface Cu/In ratio may be an indication that this sample was not sufficiently Cu-rich to produce a significant $Cu_{2-x}Se$ phase at the surface. It is interesting to note that the difference in the surface Cu content for the "Cu Poor" and "Cu Rich" samples (0.14 ± 0.10) is close to the difference in bulk Cu content (0.16 ± 0.16).

The "Cu Rich Etched" sample shows a comparable Cu content at the surface after the KCN etch, but an increase in the Se/(Cu+In) ratio. An increase in Se intensity would be expected, since the KCN etch preferentially removes the $Cu_{2-x}Se$ phases, making the stoichiometric $CuInSe_2$ more dominant at the surface. However, a parallel decrease in Cu would also be expected, and is not seen. This is further evidence for a limited $Cu_{2-x}Se$ phase presence at the "Cu Rich" sample surface.

The "Cu Poor", "Cu Rich", and "Cu Rich Etched" samples all have Se-poor surfaces, as shown from the Se/(Cu+In) ratios in Table 5.2. The surface Se concentration has been shown to increase opposite of Cu depletion due to either an increase in Se-rich phases such as In_2Se_3, or an absence of Se vacancy sites, which, in the bulk, form easily in the presence of Cu_{In} antisites in Cu-rich materials. [24,25] Thus the slight Se-poor nature

of the “Cu Poor” surface and the more exaggerated Se-poor nature of the “Cu Rich” surface are expected, based on the Cu/In ratios. The Se-rich nature of the “In-Se Treated” sample surface is also expected due to both the extremely low surface Cu/In ratio and the final In and Se deposition step. Despite the strong variation in surface Cu:In:Se ratios in the “In-Se Treated” sample relative to the other samples, no evidence of In_xSe_y compounds was found from the XPS and X-ray Auger Electron Spectroscopy detailed spectra of In and Se (not shown).

To further investigate the stoichiometry at the surface, HAXPES measurements were performed with a photon energy of 6030 eV. These measurements have a deeper IMFP (1/e attenuation of ~10.9 nm) than that achieved with Mg K_α XPS (~ 2.6 nm).[26] This means, for example, that for the lower BE region of XPS, 85 % of the signal comes from the first 5 nm of the sample surface, while for the lower BE region of the HAXPES data, 37 % of the total signal comes from the first 5 nm of the sample surface (the remainder of the signal originating from deeper). The different photon energy used also results in different cross sections for the various photoelectric excitations, which makes some subshells more intense than as seen in XPS. The survey spectra and detailed VBM region taken from the “Cu Poor”, “Cu Rich Etched”, and “In-Se Treated” samples are shown in Fig. 5.4.

The HAXPES survey spectra in Fig. 5.4 (a) are normalized to the In 3d peak height at ~ 445 eV to allow direct comparison of changes in peak intensities between samples. The expected elements of Cu, In, and Se are present on all samples, along with Na, C, and O. With the longer IMFP (and thus a larger contribution to the spectrum from electrons originating from deeper in the sample), the “In-Se Treated” sample is still

extremely Cu-, Na-, and Se-poor (i.e., In-rich) relative to the "Cu Poor" sample. This can be seen from the Na 1s, Cu 2p, and Se 3s peaks located at ~ 1000 eV and ~ 250 eV. The "In-Se Treated" sample also has weaker C and O signals relative to the "Cu Poor" sample. This could be explained by the removal of O and C during the KCN etch, as seen from the "Cu Rich Etched" sample, which also has reduced C and O peaks. This verifies

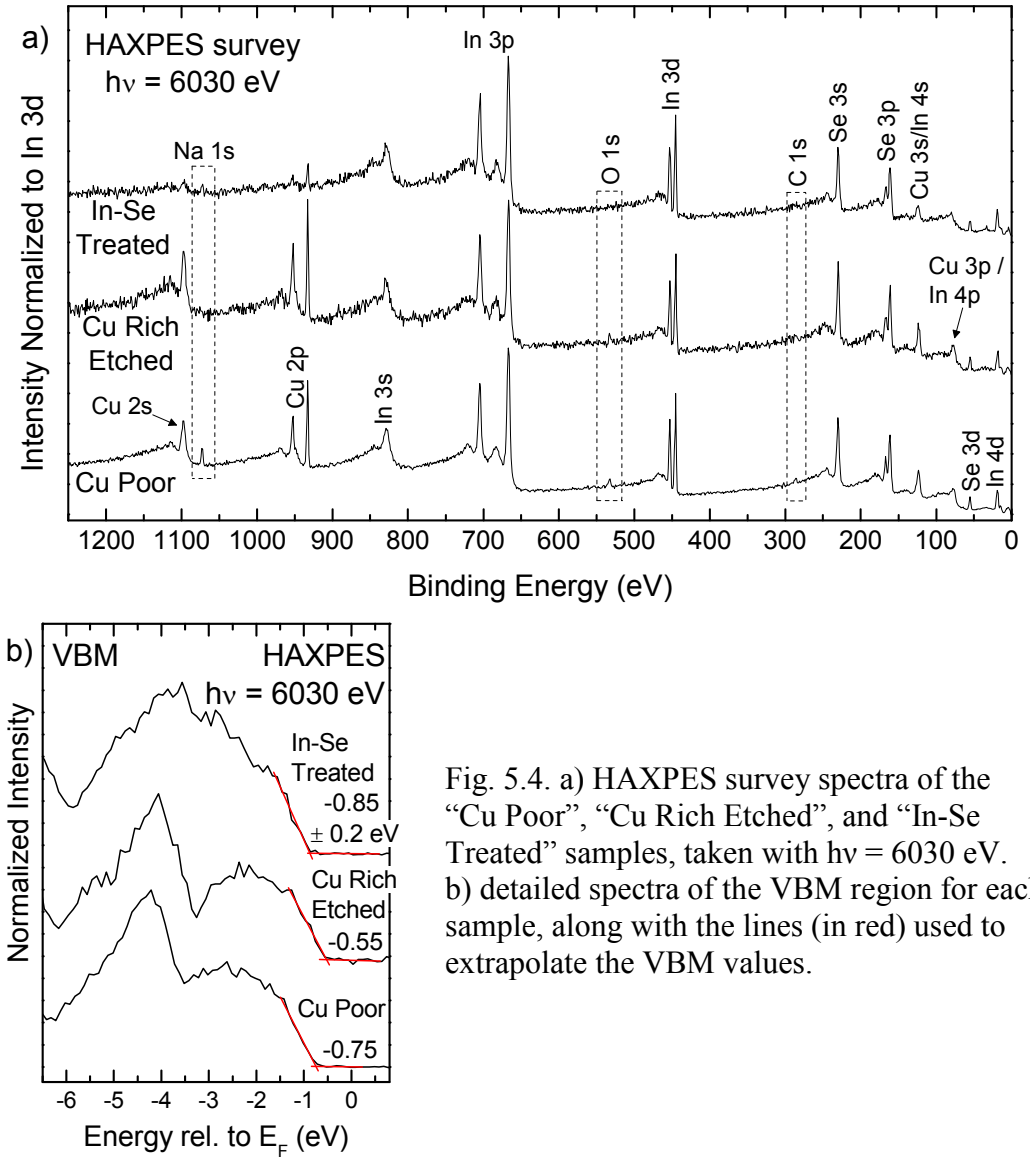

Fig. 5.4. a) HAXPES survey spectra of the "Cu Poor", "Cu Rich Etched", and "In-Se Treated" samples, taken with hν = 6030 eV. b) detailed spectra of the VBM region for each sample, along with the lines (in red) used to extrapolate the VBM values.

that the final KCN etch and In-Se deposition was performed without significant introduction of contaminants to the "In-Se Treated" sample.

Estimates of the Cu/In ratios were determined from the HAXPES survey spectra by integrating the Cu $2p_{3/2}$ and In $3d_{5/2}$ peak areas after subtracting a linear background, and then dividing the areas by the cross section of each subshell. Calculated cross section values from 1,000 – 5,000 eV and for 10,000 eV are available, published by Trzhaskovskaya et al.[27,28] The cross sections were adjusted by the angular distribution parameters as described in the aforementioned publications, based on the measurement geometry at the KMC-1 beamline and HIKE end station (with the angle between the polarization of the photons and the vector of the outgoing electron, $\theta = 0°$, and the angle between the incoming photon and y-axis component of the emitted electron, $\varphi = 90°$ [29,30]). Only the parameters for select photon energies are provided by Trzhaskovskaya et al., and thus an equation was fit to the available cross section values in order to find the value at exactly 6030 eV. A substantial error bar was given to the final ratios determined, based on 1) the use of an equation to extrapolate the cross section at the desired photon energy, 2) the uncertainty in the peak areas (a relatively large step size of 1 eV, and

Table 5.3: Estimated Cu/In ratios from the HAXPES survey spectra taken with a photon energy of 6030 eV of the "Cu Poor", "Cu Rich Etched", and "In-Se Treated" samples, along with Cu/In ratios determined from XPS and EDX.

Sample	XPS Cu/In (±0.05)	HAXPES Cu/In (±0.10)	EDX Cu/In (±0.03)
Cu Poor	0.34	0.54	0.91
Cu Rich Etched	0.48	0.70	1.06
In-Se Treated	0.11	0.13	0.99

estimation of peak tails), and 3) any changes in the analyzer transmission function and the IMFP of the photoelectrons measured (ranging from 5100 to 5800 eV KE for the Cu 2p and In 3d, corresponding to an IMFP of 9.3 to 10.2 nm). The results are shown in Table 5.3, along with the XPS and EDX results, shown in order of decreasing surface sensitivity.

Relative to the Cu/In ratios determined from XPS, all three Cu/In ratios determined from the HAXPES data are increased, suggesting an increase in the Cu content farther from the sample surface for all three samples. While the Cu/In ratios for the "Cu Poor" and "Cu Rich Etched" samples are both strongly approaching that of their bulk ratios, the "In-Se Treated" sample is still extremely Cu-poor relative to the bulk Cu/In ratio of 0.99. Further, the change in Cu/In ratios between HAXPES and XPS for the "In-Se Treated" sample is within the error bar for the two measurements, such that the apparent increase in the Cu/In ratio for this sample may not be significant. This suggests a rather thick Cu-depletion layer at the surface of the "In-Se Treated" sample, such that a significant portion of the Cu-rich bulk is not included in the still surface-sensitive HAXPES measurement.

Fig. 5.4 (b) shows detailed spectra of the VBM taken with a photon energy of 6030 eV. The resulting photoelectrons have a much longer IMFP than those in the UPS spectra in Fig. 5.2, and thus a larger portion of the measured electrons here are expected to originate from deeper in the sample. It is noted that when comparing this HAXPES data to the UPS data, a larger step size (0.1 vs. 0.02 eV) was used, and a lower resolution (0.30 vs. 0.13 eV) was achieved.

Relative to the UPS measurement, the VBM here for the "Cu Poor" sample is shifted upward by 0.15 eV. Cu-poor $CuInSe_2$ has been shown to have a broadened surface E_g, which narrows towards the bulk.[7] Since the shallowest bands probed will define the VBM, a higher VBM might be expected here for the "Cu Poor" sample, due to the narrowing energy gap between the VB and E_F expected farther in from the surface contributing more greatly to the final spectrum. Some of this narrowing may also be due to the lower resolution of the HAXPES measurements relative to the UPS measurements, and the associated broadening of the spectral features.

The "Cu Rich Etched" sample has a VBM 0.55 eV below E_F and 0.2 eV higher than the "Cu Poor" sample. This is similar to the UPS measurements, in which the "Cu Rich" sample VBM was 0.15 eV higher than the "Cu Poor" sample. This suggests a more narrow band gap for the "Cu Rich Etched" sample, as expected from the higher Cu/In ratio.

For the "In-Se Treated" sample the VBM position is similar to that measured with the much more surface-sensitive UPS, showing a consistent VBM position with a longer IMFP measurement. This matches with the strong Cu-depletion still seen for this sample from the HAXPES data, suggesting also a more homogeneous Cu/In ratio farther in from the surface. Due to the high overall Cu/In ratio of 0.99, an increased Cu-content in the bulk is expected. Thus, while no change in the VBM is seen between UPS and HAXPES, a change in the VBM could be present further in from the surface.

5.3.2 Near-Surface Bulk Stoichiometry and Band Gap

The XES spectra taken for all samples are shown in Fig. 5.5, and further support the findings thus far. Fig. 5.5 (a) shows the 300 to 400 eV emission window, which

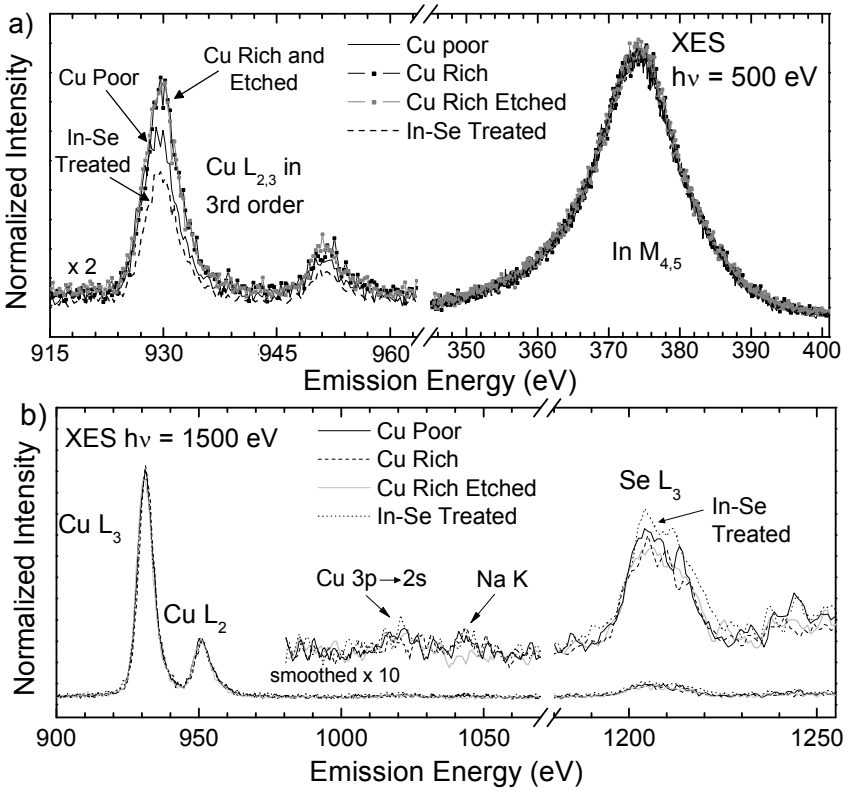

Fig 5.5: a) XES at hν = 500 eV of the Cu $L_{2,3}$ emission in 3rd order and In $M_{4,5}$ in 1st order, normalized to the In $M_{4,5}$ intensity. b) XES at hν = 1500 eV of the Cu $L_{2,3}$, Na K, and Se L_3 emissions, normalized to the Cu L_3 emission.

contains the Cu $L_{2,3}$ emission in 3rd order (shown on the 1st order energy axis) and the In $M_{4,5}$ emission, with an estimated attenuation length (1/e of the original intensity) of 150 nm for the photons being detected. The spectra are normalized to the intensity of the In $M_{4,5}$ emission to directly visualize the variations in the Cu/In ratio.

Care must be taken in analyzing the variations in peak intensity, since the Cu $L_{2,3}$ x-ray emission is of a sufficient energy (~ 930 and 950 eV) to be re-absorbed by the In $M_{4,5}$ edge (~ 375 eV). This is a significant effect, and is well illustrated by a comparison of the photoabsorption cross sections for a 931 eV photon, which is approximately 3 ½ times greater for In than for Se.[31] Thus an increase in In content in the sample would result in a greater reabsorption effect, and an artificially reduced Cu intensity. For

$CuInSe_2$, an increase in In is expected to be concurrent with a decrease in Cu, and therefore this photoabsorption effect would be expected to accentuate any true variations in the Cu/In ratio.

From the variations of the Cu L_3 intensity, the "In-Se Treated" sample is shown to still be Cu-poor (In-rich) relative to all other samples, with a Cu L_3peak approximately half that of the "Cu Rich". From the surface Cu/In ratios, a much more reduced Cu signal relative to the "Cu Rich" sample would be expected. Further, the increased In content would be expected to result in a stronger reabsorption effect, and a further reduced Cu signal. That the Cu L_3 is a full half the intensity of the "Cu Rich" might therefore be taken as an indication of a strong increase in the Cu content of the "In-Se Treated" sample with the deeper attenuation length of this measurement. A variation in the Cu/In ratio is also seen between the "Cu Poor" and "Cu Rich" samples, which is expected from the differences in both the surface (XPS) and bulk (EDX) Cu/In ratios of these two samples.

Fig. 5.5 (b) shows the window from 915 to 1250 eV, which contains the Cu $L_{2,3}$, Na K, and Se $L\ell$ emissions. The spectra are normalized to the Cu L_3 area to determine variations in the Cu/Se ratio. We see the highest Se/Cu ratio for the "In-Se Treated" which may be a result of both the high Se/(Cu+In) ratio and low Cu/In ratio seen at the surface of this sample. For the other three samples, the Se/Cu ratio does not vary significantly.

The "Cu Poor", "Cu Rich", and "In-Se Treated" samples show a small Na K emission at ~ 1040 eV, which is notably weaker than is usually seen for chalcopyrite absorbers (see, e.g., Fig 4.4). The "In-Se Treated" sample shows a comparable Na K

intensity to both the "Cu Poor" and "Cu Rich" samples, which is in contrast to the variation seen between samples in the XPS survey spectra. This could be due to the normalization to Cu, which for the "In-Se Treated" sample increased the intensity of other emission peaks as well, or due to the behavior of Na, which is known to sit predominantly at the absorber surface.[32] The variation in Na content at the very surface could be within the noise for these measurements with a longer attenuation length. A complete absence of any Na K intensity is seen for the "Cu Rich Etched" sample, showing the Na to have been removed from both the surface and the grain boundaries of this sample at least 200 nm in from the surface.

XES and XAS of the Cu L_3 edge for the "Cu Poor", "Cu Rich", and "In-Se Treated" samples is shown in Fig. 5.6, along with a Cu foil reference. XES probes

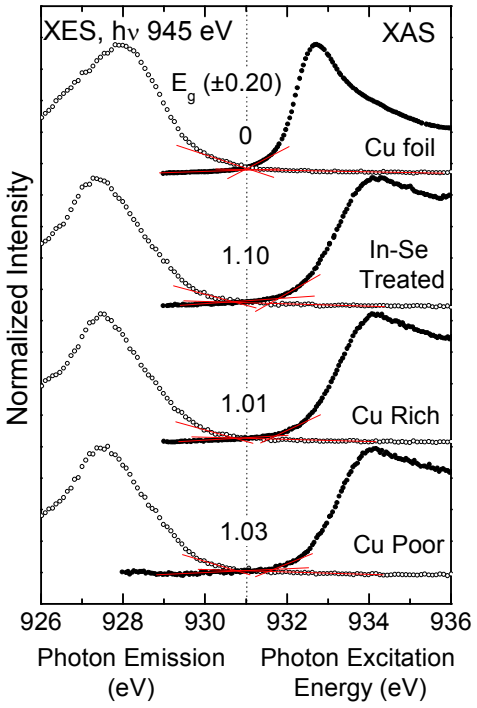

Fig 5.6: Cu L_3 XES and XAS taken from the "Cu Poor", "Cu Rich", and "In-Se Treated" samples, and a Cu foil reference.

radiative relaxation events between occupied states, while XAS probes excitations into unoccupied states. Together they provide an estimate of the band gap up to ~200 nm in from the surface. An error bar of ± 0.20 eV is given for these measurements to account for both the determination of the onsets, and because of the nature of these measurements. XAS is the excitation of a core electron into an unoccupied state, and thus measures the energy of this transition in the presence of a core-hole. The minimum absorption energy is therefore less than the energy of the un-perturbed state by an amount equal to the core exciton binding energy, which may vary from negligible values up to 0.4 eV.[33] This method of determining the band gap must therefore be taken as a lower limit for the "true" band gap.[7] While the absolute value is prone to error, the relative values, and variations between samples are more reliable (since all XAS measurements are performed in the presence of a core-hole).

A band gap value between 1.0 and 1.1 eV is found for all three samples. While small variations are present between the samples which trend with the Cu/In ratios seen in Fig. 5.5, all variations are well within the error of this measurement (the difference between the "Cu Poor" and "Cu Rich" samples is certainly within the error of the data analysis, i.e., linear extrapolations). While these values should be taken as "minimum" values (the true band gap in the absence of a core-hole may be larger), we note that the band gap measured is similar to the bulk band gap of stoichiometric $CuInSe_2$, which is expected for all samples. The similar band gap values also suggest that some level of homogeneity in the Cu/In ratio is found between samples, possibly indicating the achievement of stoichiometry for all three samples within ~ 200 nm of the surface. While this may at first seem to disagree with the Cu/In variations seen by XES in Fig. 5.5, the

following hypothesis shows this to be a possibility. If, for example, the "In-Se Treated" absorber reached a stoichiometric Cu/In ratio 100 nm in from the surface, a Cu-depletion relative to the "Cu Poor" and "Cu Rich" sample would still be seen in the XES data due to the extreme Cu-poor nature of the very surface. However, the smallest band gap within ~ 200 nm of the surface (i.e., the band gap towards the bulk and close to 1.0 eV) would be measured by the XES and XAS data in Fig. 5.6. The bulk band gap for the "Cu Poor" sample is also expected to be near 1.0 eV, with the Cu-depletion only at the surface.

5.4 Conclusion

We have investigated the chemical and electronic properties from the surface to the near-surface bulk of a new $CuInSe_2$ absorber design in which a Cu-rich bulk deposition is paired with a final In-Se treatment to produce a Cu-poor surface. The novel absorber was investigated along-side a Cu-poor absorber and a Cu-rich absorber before and after KCN-etch, for direct comparison. From XPS we find a surface Cu/In ratio of 0.11 ± 0.05 and a Se/(Cu+In) ratio of 1.06 ± 0.05, showing the surface of this novel absorber to be very Cu-poor and slightly Se-rich. Despite the variation in Cu/In ratio, a surface E_g similar to that of the traditional Cu-poor grown absorber is measured for the novel absorber. A reduced Na content at the surface of the novel absorber is also found, most likely due to the KCN-etch of the Cu-rich deposited absorber layer prior to the final In-Se deposition. An increase in the Cu/In ratio is present for all samples measured with HAXPES, with the novel absorber still very Cu-poor. The VBM as measured with 6030 eV photons (with a longer IMFP) is closer to the Fermi energy for the Cu-poor sample, but equivalent to the UPS-determined VBM for the novel absorber. Near-surface bulk XES measurements

with an attenuation length of ~ 200 nm show a continued Cu depletion for the novel absorber compared to both the Cu-rich and traditional-grown, Cu-poor absorbers. Using XAS in conjunction with XES, however, we find no variation in the near-surface bulk E_g of the novel absorber and the Cu-poor and Cu-rich grown absorbers.

From the success thus far of these novel-grown absorbers (reaching a conversion efficiency of 13.1 %, compared to 13.5 % for Cu-poor grown absorbers), we expect the Na depletion and Cu depletion at the surface to not be detrimental. The similar surface E_g found for both the novel absorber and Cu-poor grown absorber shows that the novel absorber design successfully mimicks the electronic structure of the Cu-poor surface. The equivalent near-surface bulk E_g found for all absorbers suggests that within 200 nm from the surface, all samples achieve a comparable, most likely stoichiometric, Cu/In ratio. This also indicates a narrowing of the E_g away from the surface for the novel absorber, which is a characteristic of successful chalcopyrite absorbers.

5.5 References

(1) "EMPA takes thin film solar cells to a new level; A new world record for solar cell efficiency" Internet Media Release, 17 January 2013. Web. 29 May 2014.

(2) Jackson, P.; Hariskos, D.; Lotter, E.; Paetel, S.; Wuerz, R.; Menner, R.; Wischmann, W.; Powalla, M. *Prog. Photovolt. Res. Appl.* **2011**, *19*, 894–897.

(3) "Solar Frontier Sets Thin-Film PV World Record with 20.9% CIS Cell." Internet Media Release, 2 April 2014. Web. 29 May 2014.

(4) Schmid, D.; Ruckh, M.; Grunwald, F.; Schock, H. W. *J. Appl. Phys.* **1993**, *73*, 2902–2909.

(5) Morkel, M.; Weinhardt, L.; Lohmüller, B.; Heske, C.; Umbach, E. *Appl. Phys. Lett.* **2001**, *79*, 4482–4484.

(6) Schulmeyer, T.; Hunger, R.; Klein, A.; Jaegermann, W.; Niki, S. *Appl. Phys. Lett.* **2004**, *84*, 3067–3069.

(7) Bär, M.; Nishiwaki, S.; Weinhardt, L.; Pookpanratana, S.; Fuchs, O.; Blum, M.; Yang, W.; Denlinger, J. D.; Shafarman, W. N.; Heske, C. *Appl. Phys. Lett.* **2008**, *93*, 244103.

(8) Scheer, R. *Thin Solid Films* **2011**, *519*, 7472–7475.

(9) Wilhelm, H.; Schock, H.-W.; Scheer, R. *J. Appl. Phys.* **2011**, *109*, 084514.

(10) Tuttle, J. R.; Albin, D. S.; Noufi, R. *Sol. Cells* **1991**, *30*, 21–38.

(11) Turcu, M.; Pakma, O.; Rau, U. *Appl. Phys. Lett.* **2002**, *80*, 2598.

(12) Zhang, S.; Wei, S.-H.; Zunger, A.; Katayama-Yoshida, H. *Phys. Rev. B* **1998**, *57*, 9642–9656.

(13) Siebentritt, S.; Guetay, L.; Regesch, D.; Aida, Y.; Depredurand, V. *Sol. Energy Mater. Sol. Cells* **2013**, *119*, 18–25.

(14) Depredurand, V.; Tanaka, D.; Aida, Y.; Carlberg, M.; Fevre, N.; Siebentritt, S. *J. Appl. Phys.* **2014**, *115*.

(15) Depredurand, V.; Aida, Y.; Larsen, J.; Eisenbarth, T.; Majerus, A.; Siebentritt, S. In *2011 37th IEEE Photovoltaic Specialists Conference (PVSC)*; 2011; pp. 000337–000342.

(16) Repins, I.; Contreras, M. A.; Egaas, B.; DeHart, C.; Scharf, J.; Perkins, C. L.; To, B.; Noufi, R. *Prog. Photovolt. Res. Appl.* **2008**, *16*, 235–239.

(17) Weinhardt, L.; Fuchs, O.; Groß, D.; Storch, G.; Umbach, E.; Dhere, N. G.; Kadam, A. A.; Kulkarni, S. S.; Heske, C. *Appl. Phys. Lett.* **2005**, *86*, 062109.

(18) Heske, C.; Fink, R.; Umbach, E.; Riedl, W.; Karg, F. *Cryst. Resolut. Technol.* **1996**, *31*, 919–922.

(19) Zellner, M. B.; Birkmire, R. W.; Eser, E.; Shafarman, W. N.; Chen, J. G. *Prog. Photovolt. Res. Appl.* **2003**, *11*, 543–548.

(20) Heske, C.; Fink, R.; Umbach, E.; Riedl, W.; Karg, F. *Appl. Phys. Lett.* **1996**, *68*, 3431–3433.

(21) NIST X-Ray Photoelectron Spectroscopy Database, Version 4.1. (National Institute of Standards and Technology, Gaithersburg, 2012); http://srdata.nist.gov/xps/.

(22) Williams, G. P. In *X-ray Data Booklet*; Center for X-ray Optics and Advanced Light Source: Berkeley, CA, 2009.

(23) Scofield, J. H. *J. Electron Spectrosc. Relat. Phenom.* **1976**, *8*, 129–137.

(24) Niemi, E.; Stolt, L. *Surf. Interface Anal.* **1990**, *15*, 422–426.

(25) Neumann, H.; Tomlinson, R. D. *Sol. Cells* **1990**, *28*, 301–313.

(26) Powell, C. J.; Jablonski, A. *NIST Electron Effective-Attenuation-Length Database, Version 1.3, SRD 82*; National Institute of Standards and Technology: Gaithersburg, MD, 2011.

(27) Trzhaskovskaya, M. B.; Nefedov, V. I.; Yarzhemsky, V. G. *At. Data Nucl. Data Tables* **2001**, *77*, 97–159.

(28) Trzhaskovskaya, M. B.; Nikulin, V. K.; Nefedov, V. I.; Yarzhemsky, V. G. *At. Data Nucl. Data Tables* **2006**, *92*, 245–304.

(29) Gorgoi, M.; Svensson, S.; Schäfers, F.; Öhrwall, G.; Mertin, M.; Bressler, P.; Karis, O.; Siegbahn, H.; Sandell, A.; Rensmo, H.; Doherty, W.; Jung, C.; Braun, W.; Eberhardt, W. *Nucl. Instrum. Methods Phys. Res. Sect. Accel. Spectrometers Detect. Assoc. Equip.* **2009**, *601*, 48–53.

(30) Schaefers, F.; Mertin, M.; Gorgoi, M. *Rev. Sci. Instrum.* **2007**, *78*, 123102.

(31) Henke, B. L.; Gullikson, E. M.; Davis, J. C. *At. Data Nucl. Data Tables* **1993**, *54*, 181–342.

(32) Heske, C.; Eich, D.; Groh, U.; Fink, R.; Umbach, E.; van Buuren, T.; Bostedt, C.; Franco, N.; Terminello, L. J.; Grush, M. M.; Callcott, T. A.; Himpsel, F. J.; Ederer, D. L.; Perera, R. C. C.; Riedl, W.; Karg, F. *Thin Solid Films* **2000**, *361–362*, 360–363.

(33) Bechstedt, F.; Enderlein, R.; Koch, M. *Phys. Status Solidi B* **1980**, *99*, 61–70.

CHAPTER 6

CHEMICAL SURFACE AND INTERFACE PROPERTIES OF DIFFERENTLY STRESSED (Au/Cu/)CdTe/CdS THIN-FILM SOLAR CELL STRUCTURES

This project and a portion of the data and conclusions shown here were presented by the author at a poster session at the 38th IEEE PVSC conference, June 2012 in Austin, TX. A majority of the text and figures were previously published through IEEE in a co-authored work.[1]

6.1 Introduction

CdTe-based solar cells, presently the most commercially successful thin-film photovoltaic technology, have reached efficiencies of up to 21.0 % in lab.[2] To ensure that such high efficiencies are preserved over the lifetime of the device, it is important to both identify and prevent possible causes of degradation. As discussed in Chapter 2, one known cause of cell degradation is Cu, which is commonly used in the back contact as a "buffer layer" to produce an ohmic contact with the CdTe absorber.[3] Cu readily diffuses into CdTe, and initially causes beneficial changes to the band edges and electronic properties of this layer, especially at the metal/CdTe interface.[4]

After heat stress treatments, cells with Cu back contacts show a decreased efficiency. Rollover in the I-V curves is often present, indicating the degradation of the metal/semiconductor interface due to the formation of a barrier to charge transport.[5] However, rollover was not seen by Visoly-Fischer et al. in the absence of both humidity and Cl.[5] This suggests Cu, along with Cl and O, has a detrimental effect on the back

contact/semiconductor junction, and that oxygen plays a role in the back contact degradation. Direct evidence for the oxidation of sulfur in the presence of Cu has been previously shown,[6] which is further evidence for the formation of an oxide layer at the back contact / CdTe interface after stress.

To further study the degradation-related chemical changes in CdTe solar cells, we have studied the chemical surface and interface properties of differently stressed (Au/Cu/)CdTe/CdS thin-film solar cell structures using x-ray photoelectron (XPS), Hard x-ray photoelectron (HAXPES), and soft x-ray emission (XES) spectroscopy. Masks were used for the Au/Cu back contact deposition, creating samples in which both the Au/Cu back contact and the surface of the CdTe absorber were accessible for characterization. Four samples were prepared and each subjected to a different heat stress treatment, varying the ambient environment and light exposure. The chemical composition of the surface and near-surface bulk of both types of surfaces was investigated by XPS, HAXPES, and XES.

6.2 Sample Description and Experimental Details

The samples were produced at the University of Toledo, Ohio (UT) by Dr. Naba Paudel and the group of Prof. Alvin Compaan. This project was part of an extended collaboration between UNLV and UT, and funded through the DOE Solar America Initiative. Previous sample sets under this project were studied by Sujitra Pookpanratana, and she also headed the design of this sample set prior to graduation. The CdTe/CdS stacks were prepared on SnO_2:F (FTO)-covered 3 mm-thick TEC15 soda lime glass superstrates, using magnetron sputtering for both the CdS and CdTe layers. The thickness of the CdS (CdTe) layer was

approximately 0.12 (2.0) μm. The CdTe surfaces underwent a wet treatment of drops of methanol saturated with $CdCl_2$, followed by a 30 minute activation step at 387 °C. This was followed by the back contact, consisting of 3 nm of Cu followed by 20 nm of Au, evaporated onto the CdTe surface in approximate areas of 4 mm^2 and 10 mm^2 with the use of a mask. This resulted in large areas of the CdTe which were bare and large areas covered by the back contact materials. The finished cells underwent a final thermal treatment step at 150 °C for 45 minutes in ambient air. After processing, three sibling samples each underwent different heat and environment stress treatments at 85 °C (in ambient air or N_2, while exposed to air mass (AM) 1.5 illumination or kept in the dark) for two weeks. A fourth sample (D, control), acting as an internal reference, was stored in a desiccator at room temperature (in the dark) for the duration of the two-week stress treatments. Table 6.1 summarizes the conditions for each sample.

After stress treatment, all four samples were vacuum-sealed under dry N_2 and shipped to UNLV. The samples were unpacked in a N_2-purged glove box, mounted, and moved into a directly attached ultra-high vacuum (UHV, base pressure < 3×10^{-10} mbar) XPS analysis system for characterization. For experiments performed at the ALS, the samples were resealed in the N_2 glove box for shipment and briefly exposed to air while

Table 6.1: CdTe sample stress treatments

Sample	**Treatment**			
	Atmosphere	Illumination	Temp (°C)	Duration
A	Air	AM 1.5	85	2 weeks
B	N_2	AM 1.5	85	2 weeks
C	Air	Dark	85	2 weeks
D	Desiccator	Dark	22 (room)	2 weeks

mounting and introducing the samples into the UHV XES analysis system. The surface-sensitive XPS measurements were performed at UNLV using the equipment described in Section 3.2.3, the HAXPES measurements were performed at the BESSY synchrotron described in Section 3.2.4, and the near-surface bulk sensitive XES measurements were performed at the ALS, as described in Section 3.8.1.

6.3 Results and Discussion

6.3.1 XPS

Fig. 6.1 shows XPS survey spectra taken from (a) the Au/Cu back contact and (b) an exposed CdTe area from the four investigated samples. All XPS spectra taken on the back contacts show the expected Au-related photoemission lines. In addition, C-, O-, and Cl-related XPS and Auger lines (due to surface contaminants and the applied $CdCl_2$ treatment) are observed. The photoemission lines of copper (Cu 2p and Cu LMM) are also identified on all samples, which is interesting in regards to the surface-sensitive nature of XPS, which is governed by the IMFP of the emitted photoelectrons (typically in the 1-3 nm range[7]). Because of this fact, one could expect that XPS of the Au (20 nm)/Cu (3 nm) contact regions would only probe the Au and not the underlying Cu and CdTe film. The significant intensities of the Cu-related photoemission lines might therefore be interpreted as an indication for a significant morphological change of the Au layer and/or an intermixing/alloying of the Au contact with the underlying Cu and CdTe layers. The presence of Cd- and Te-related emission in all but the B sample also supports a morphological change in the back contact layer, such as the presence of voids, which have been observed before in similarly prepared samples.[8] However, despite using the

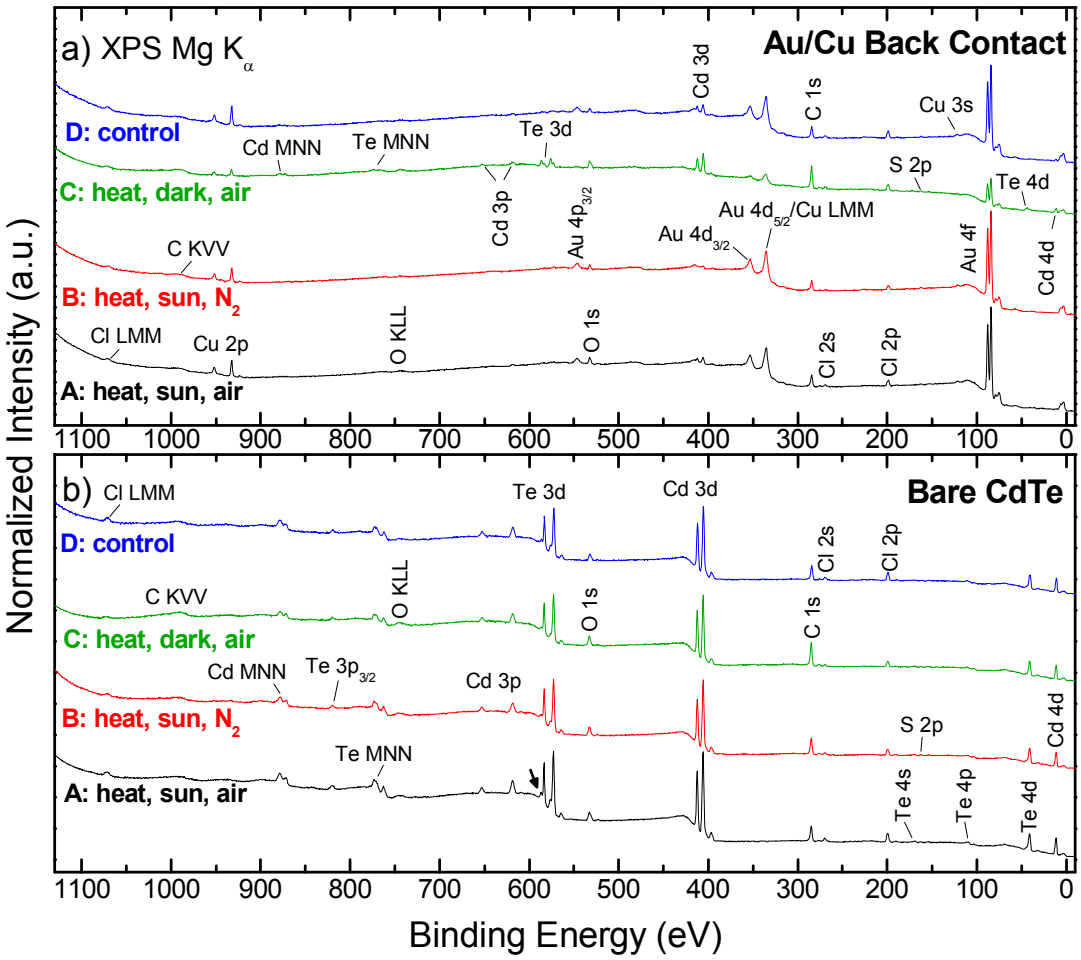

Fig. 6.1: XPS survey spectra taken on (a) the Au/Cu back contact area and (b) the bare CdTe area of samples A-D, using Mg K_α excitation.

small area lens mode of the electron analyzer – which should, in principal, allow the study of exclusively the Au/Cu contact area – it cannot be ignored that a sample misalignment could lead to the inclusion of the CdTe regions outside of the metal contact area in these measurements. This could explain the Cd and Te signals present, as well as the variations between samples, such as the absence of a significant Cd signal on the B sample, and strong Cd and Te signals observed on the C sample.

The survey spectra taken on the regions of exposed CdTe for all samples are shown in Fig. 6.1 (b). The expected photoemission lines from Cd and Te are present for all samples, along with C, O, and Cl from surface contaminants and the $CdCl_2$ treatment. No Au- or Cu-related photoemission lines are present for these spectra, showing a successful exclusion of the Au/Cu back contacts from the measurement areas.

The survey spectra of sample C vary significantly from those of the other samples in a number of ways. For the back contact survey in Fig. 6.1 (a), the intensities of the C 1s and O 1s peaks are significantly increased, while the intensity of the Au 4f and the Cu 2p peaks are strongly reduced. These findings indicate a significant C- and O-containing surface contamination layer on the Au/Cu contact, which attenuates the signals from the Cu and Au atoms underneath. Due to the significant difference in kinetic energies of the Cu 2p and Au 4f peaks (and hence of the associated information depths), a quantification of the Au/Cu ratio is very unreliable. The Cd and Te peaks in this spectrum are also much more intense than for the other samples, such that the presence of two sets of peaks for the Te 3d signal can be distinguished from the survey. The two Te $3d_{5/2}$ peaks at ~ 573 and ~ 576 eV indicate that the Te at the surface is in two chemical environments: most likely a CdTe-like bonding environment (expected at an energy of 572.7 to 573 eV), and either an oxidized environment (expected from 576.1 to 577.7 eV) or a chlorinated Te environment (e.g., $TeCl_4$ would be expected at ~576.9 eV).[9] Furthermore, the higher BE peak is more intense than the CdTe-like peak, showing the majority of the Te in the information depth to be in a non-CdTe like environment. A second peak is also seen for all samples in the survey spectra of the exposed CdTe regions, as indicated by the arrow in Fig. 6.1 (b) on the higher BE side of the Te 3d peaks. The peak intensity is limited and

comparable for all samples, despite the varying heat treatments and the fact that some samples were air exposed. Thus, while Te oxidation may be expected, increased oxidation is seen for sample C, in the presence of the Au/Cu back contact. A strong increase in Te-O after heat-stressing in air has been reported previously for CdTe covered by a Cu back contact.[5] This suggests that the Te signal seen on the C sample is from Te atoms affected by the Au/Cu back contact, either at the edges of the metallic contact areas, or possibly seen through the voids.

A small sulfur signal (S 2p at 162 eV) is also observed at the surface of all four samples on both the bare CdTe and the Au/Cu back contact regions. This suggests sulfur migration from the CdS layer through the CdTe absorber and into the back contact, or to the (Au/Cu)/CdTe interface. Previous experiments have shown S to accumulate at the back contact/CdTe interface after $CdCl_2$ treatment.[6] The presence of S in all survey spectra shows S to have migrated to the surface of the exposed CdTe and at least to the (Au/Cu)/CdTe interface for all samples, regardless of the heat stress treatment.

6.3.2 HAXPES

To further investigate the (Au/Cu)/CdTe interface, HAXPES survey spectra using a 6030 eV photon energy were taken from the back contact regions of samples A, B, and D. The higher photon energy used for these measurements results in a higher KE for the photoelectrons, and thus a longer IMFP (approximately 5.5 nm through Au, 6.9 nm through Cu, and 10.8 nm through CdTe[10]) relative to the XPS spectra. Despite the reduced signal attenuation, nearly 97 % of the signal would still be expected to originate from the 20 nm thick surface Au layer if it were uniform and closed. The lower BE region of the spectra up to 600 eV are shown in Fig. 6.2, normalized to the Au $4f_{7/2}$ peak

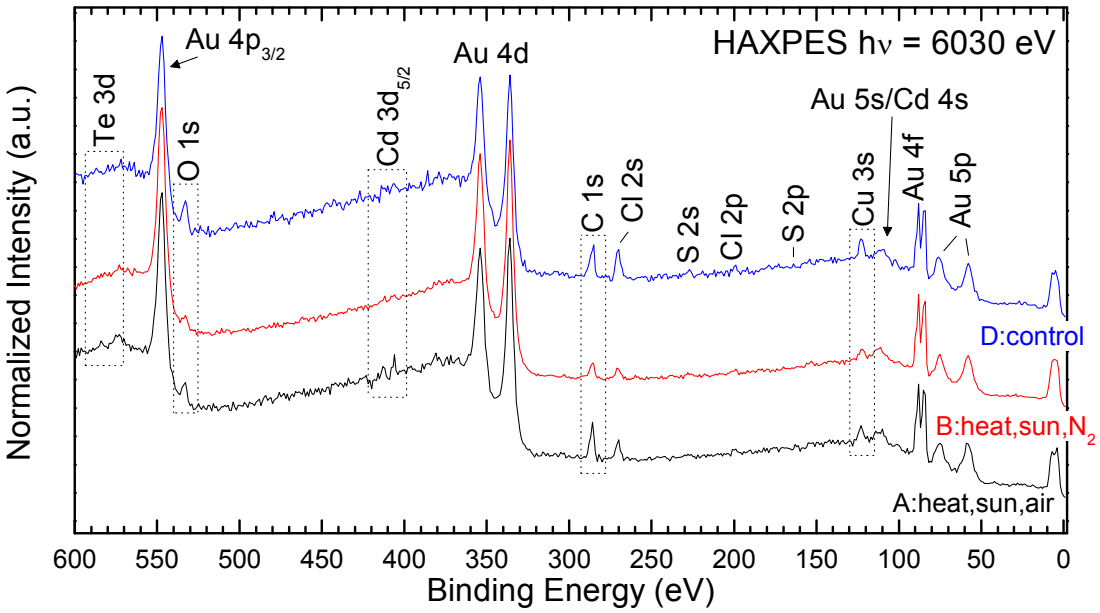

Fig. 6.2: HAXPES survey spectra (hν = 6030 eV) taken from the back contact regions on samples A, B, and D. Spectra are normalized to the intensity of the Au $4f_{7/2}$ peak.

intensity. While the most prominent peaks in all surveys are from Au, peaks of significant intensity are also seen from Cu, C, O, Cl, and S. A small Cd 3d signal is distinguishable in all spectra at ~ 400 eV, and confirmed in a detailed spectrum from sample D (not shown). A definite Te signal is seen at ~ 570 eV for sample A only.

The spectra from samples A and D are most comparable, with all peaks of approximate equal intensity, except for a slightly higher Cl signal and absent Te signal for sample D. Sample B varies significantly from the other two samples, with a noticeably lower Cu, Cl, C, and O signal. This may be also be due to a stronger Au signal on the B sample, which with normalization, would reduce the apparent intensity of all other peaks.

The photon energy used here results in different cross section values for the various electron shells, compared to those seen in XPS using Mg or Al K_α. At a photon

energy of 6030 eV, a higher cross section is realized for the Cu 3s subshell, which allows for an easier comparison of the Cu/Au ratio from the Cu 3s and Au 4f peaks at ~ 120 and 85 eV, respectively. Unlike the Cu 2p and Au 4f comparison that was possible from the XPS survey spectra, this comparison is not strongly affected by variations in surface contamination, due to the proximity of the two peaks. Here we see a strong change in the Cu/Au ratio between samples, with a much lower ratio for sample B relative to both samples A and D. This suggests the formation of pinholes and/or intermixing of the Au and Cu layers which is more pronounced for samples A and D than for sample B. A correlation between increased Cu signal and increased C, O, and Cl signals is also noted. These could be correlated (e.g., Cu, being more reactive than Au, is more likely to bond C- and O- containing adsorbates, or the presence of C and O in the environment could encourage Cu migration to the surface) or could be due to a variation in sample preparation (e.g., if a thicker Au layer were unintentionally deposited on sample B).

It is noted here that the higher Au signal seen for sample B agrees well with the XPS spectra in Fig. 6.1. This is in spite of using different pieces of each sample for the two measurements, and the smaller measurement spot size at the beamline.

6.3.3 S $L_{2,3}$ XES

To study the local chemical environment of sulfur atoms at or near the surface, XES was performed on all four samples at the S $L_{2,3}$ edge. Fig. 6.3 shows XES spectra taken on the Au/Cu back contact areas, along with the spectra of several sulfur reference compounds. For these measurements, a photon energy of 200 eV was used to create S 2p core holes, giving rise to the fluorescing decay of valence electrons into these holes. XES is a photon-in-photon-out process, and thus the information depth, determined by the

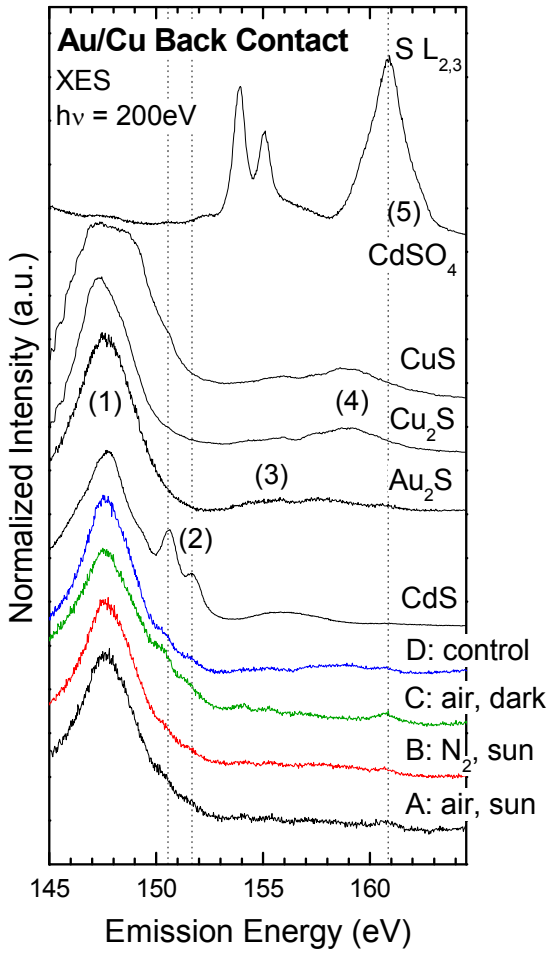

Fig. 6.3: S $L_{2,3}$ XES spectra taken on the back contact areas (Au/Cu/CdTe/CdS) of samples A-D, along with reference spectra of CdS, Au_2S, Cu_2S, CuS, and $CdSO_4$.

attenuation length of the photons in the probed material, is much larger than that of XPS (the 1/e-attenuation length of soft x-rays is approximately 80 nm in Au, 20 nm in Cu, and 210 nm in CdTe for 160 eV photons[11]). XES on the back contact areas thus allows the study of both the Au/Cu back contact layers and the material buried below, reaching into the very topmost portion of the CdTe layer (but not through the CdTe layer), and including the Au/Cu/CdTe interfaces.

All four samples show a significant S $L_{2,3}$ emission intensity, indicating pronounced sulfur migration from the CdS into the CdTe layer and back contact, as previously shown, most likely during $CdCl_2$ activation.[6,12] Based on the reduced intensity of the Cd 4d-related emission, which appears between 150 and 152 eV (feature (2)), and which is direct evidence of the presence of S-Cd bonds, a large portion of the migrated sulfur under the back contacts is not in a CdS-like environment. The overall shape of the dominant S 3s-derived emission peak at 148 eV (feature (1)), as well as the added spectral weight around 155 eV (feature (3)) and 158 eV (feature (4)), which can be ascribed to emission involving Au 5d-derived states and Cu 3d-derived states, respectively, is in reasonable agreement with a large portion of the sulfur being in a Au_2S- and/or Cu_2S-like environment.[13] This correlates with the previous findings that sulfur accumulates at the back contact/CdTe interface,[6] and thus would be in the same physical location as the back contact metals, and able to form these bonds.

The magnification of the S $L_{2,3}$ upper valence band is given in Fig. 6.4, left. In the spectrum of sample D, we find spectral weight at 155 eV and 158 eV. The comparison with the reference spectra of Au_2S and the Cu sulfides suggests the presence of Au-S and Cu-S bonds. Some evidence for such bonds is also found for sample B, while the spectra of sample A and C do not show significant intensity in these regions. Further comparison with the sulfate reference spectrum suggests the presence of some S-O bonds in all samples, particularly sample C.

A spectral analysis of the D spectrum is shown in Fig. 6.4, right, in which spectrum D is fitted by a superposition of the spectra of Au_2S, Cu_2S, and CdS. This subtraction attributes 46% of the sulfur signal to sulfur in a Au_2S-like environment, 19%

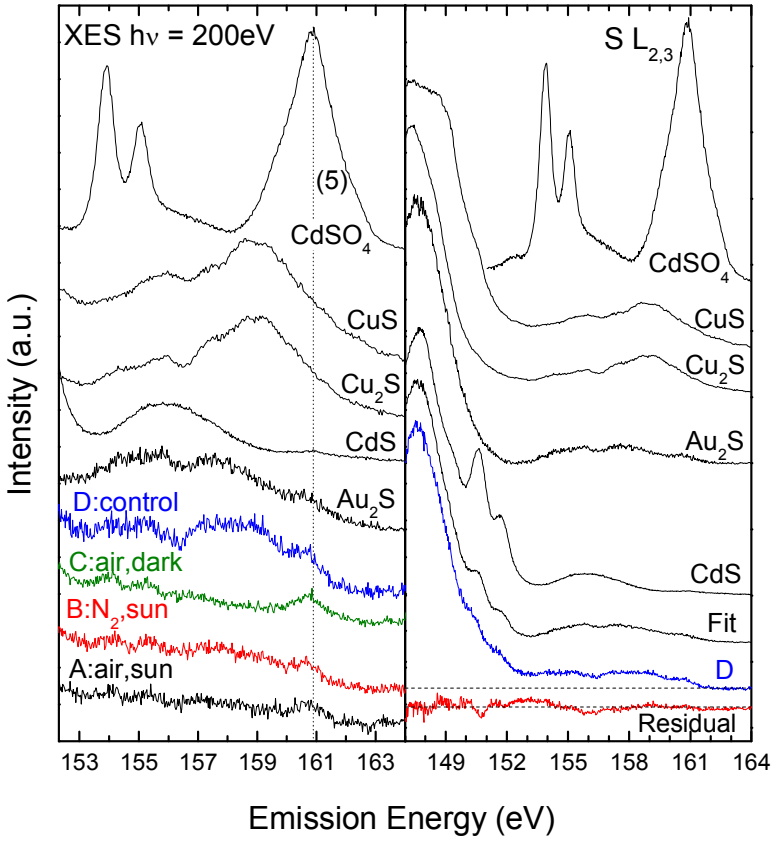

Fig. 6.4: Left: S $L_{2,3}$ XES spectra of the upper valence band of the Au/Cu/CdTe/CdS sample regions and selected references. Right: Fit analysis of the D sample spectrum.

in a Cu_2S-like environment, and 35% in a CdS-like environment. Surprisingly, inclusion of $CdSO_4$ in the fit resulted in less than 1% of the spectrum being attributed to oxides. This may be due to the spectral weight in the Au_2S reference spectrum around 154 and 161 eV, which overlaps with the sulfate features and complicates the identification of sulfate bonds. Some differences remain between the fit and the D spectrum, and a more detailed analysis would be required to determine if an additional sulfur species needs to be taken into account. Nevertheless, this analysis shows that, in the unstressed D sample, the majority of the migrated sulfur is most likely in a Au_2S-like environment, with minimal oxidation.

Of the four samples, the A and C samples show the lowest spectral intensity between 157 and 159 eV, resulting in more distinct sulfate-like peaks at 154, 155, and 161 eV. This is most apparent for the sample C spectrum, which can be confidently said to contain a sulfide component. From these observations, we see some correlation between the sulfur bonding near the (Au/Cu)/CdTe interface and the environment (N_2 or air) that the samples were held in. Specifically, the presence of Au-S and Cu-S bonds is most pronounced for samples B and D, which were not held in air, and a decrease in Au- and Cu-S bonds is seen for the two air-stressed samples.

S $L_{2,3}$ emission spectra were also measured on the exposed CdTe regions, i.e., in-between the Au/Cu contacts of each sample, and are shown in Fig. 6.5. Due to the absence of the metal back contact layers, the S $L_{2,3}$ information depth for these measurements is expected to reach almost completely thorough the 2 μm CdTe layer. All sample spectra show more pronounced Cd 4d-derived transitions (feature (2) in Fig. 6.5) indicative of sulfur in a S-Cd bond environment. This signifies that the sulfur atoms in the probing volume, i.e., in the CdTe film, form S-Cd bonds similar to those in CdS. It is interesting that this species is only predominant in the regions that are not covered by a Au/Cu back contact.

Small peaks are also present for all sample spectra which align well with the features of the $CdSO_4$ reference (features (3) and (4)), and are indicative of S-O bonds. Again, the magnitude of the sulfate contributions is comparable for all samples, which is surprising when the variation in ambient environment during stress treatment is

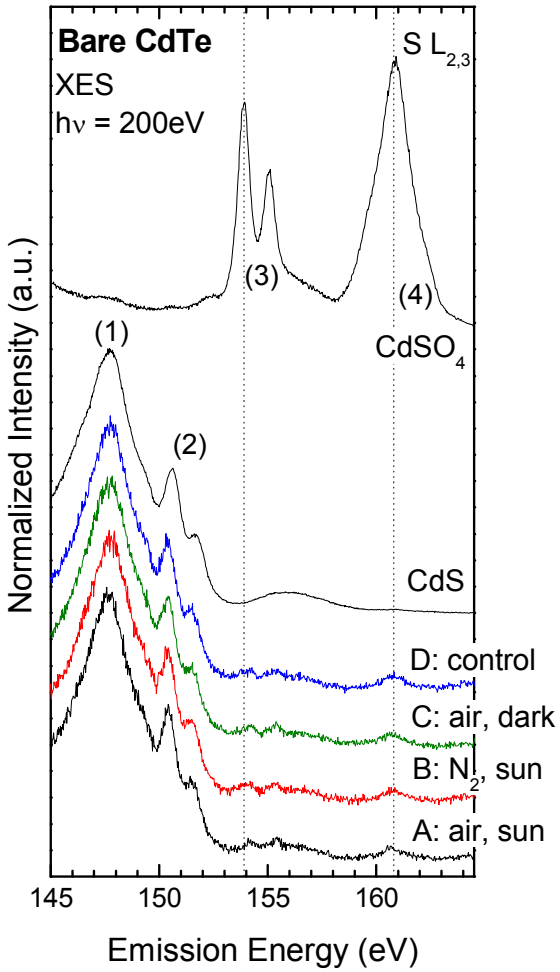

Fig. 6.5: S $L_{2,3}$ XES spectra of the CdTe samples surfaces, along with reference spectra.

considered. This suggests that heat and/or air exposure does not oxidize the sulfur diffused within the CdTe layers.

6.3.4 Cl $L_{2,3}$ XES

XES measurements of the Cl $L_{2,3}$ emission were taken of the Au/Cu back contact and the exposed CdTe area of each sample. A photon energy of 220 eV was used to excite Cl 2p core-electrons from the sample, and a photon fluorescence energy range from 170 to 200 eV was detected, resulting in an information depth comparable to that of

the S $L_{2,3}$ XES spectra. A significant chlorine intensity is found in the near-surface bulk of both the back contact and the exposed CdTe absorber. A close-up of the upper valence band region from both measurement locations, together with the respective spectra of a few chlorine reference compounds, is shown in Fig. 6.6. Comparing the Au/Cu back contact region spectra (middle), with the three reference spectra (top), we note that the broad features between 189 and 191 eV present for all samples (with maxima marked by vertical dotted lines) could best be described by a superposition of these three references. The $CdCl_2$ and $Cd(ClO_4)_2$ reference spectra, however, both show features from 184 to 188 eV that are not found in the $CuCl_2$ spectrum. An increased intensity in this area is

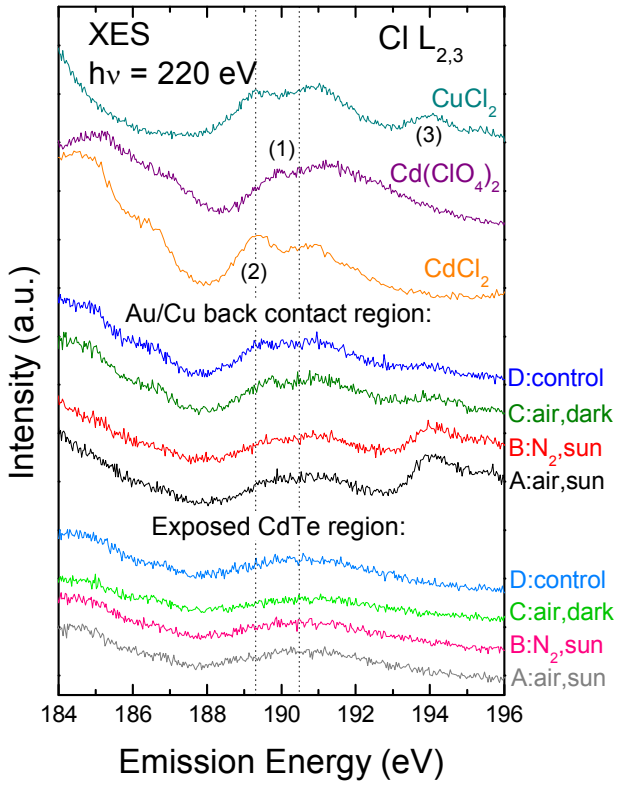

Fig. 6.6: Close-up of the Cl $L_{2,3}$ XES valence band region on the exposed CdTe area (bottom), and Au/Cu back contact (middle), along with Cl compound reference spectra (top).

seen in the spectra of sample C and D relative to samples A and B. Conversely, the $CuCl_2$ spectrum exhibits unique features from 193 to 196 eV. Similar features are present for all samples, but are dramatically increased for the spectra of the sun-exposed samples, A and B. We therefore find evidence for Cu-Cl bonds in the near-surface bulk of the (Au/Cu)/CdTe interface, predominantly in the samples that were heat-stressed under 1.5 AM illumination. Degradation studies by Visoly-Fisher et al. found a correlation between the presence of Cl and the degradation of the back contact, as manifested by rollover in the I-V curve.[5] Thus the in-diffusion of Cu with heat stress could cause the filling of V_{Cd} and thus the replacement of Cd-Cl or V-Cl complexes with Cu-Cl bonds. While some Cl-O bonding may be present for all samples, an increase in Cl-O or Cl-Cd bonding is seen for the non-illuminated samples, C and D.

The Cl $L_{2,3}$ emission spectra taken on the exposed CdTe areas are shown at the bottom of Fig. 6.6. The broad spectral features in the 184-188 eV region and also between 189 and 191 eV point to the presence of Cl in an oxidized state. No strong variation in the spectra is observed between the differently stressed samples, suggesting that there is little change in the chemical environment of Cl (located within the CdTe layer) with stress treatment.

6.4 Conclusion

We have investigated (Au/Cu/)CdTe/CdS solar cell thin-film stacks after subjection to heat stress treatment in different environments. With surface-sensitive XPS, we find evidence to suggest Au/Cu metal alloying of the back contact materials, and evidence for sulfur migration through the 2 μm thick CdTe layer and to the Au/Cu back contact for all

samples. Evidence for increased metal alloying or the presence of pinholes in the back contact with air exposure is suggested from the HAXPES data. A significant sulfur signal is seen under the back contacts using near-surface bulk XES, and both Au_2S- and $Cu_{2-x}S$-like features are observed. A correlation between air exposure and a reduction in Au- and Cu-S bond features is seen. Small sulfate signals are present in all samples, both at the Au/Cu back contact and at the exposed CdTe area. We find no evidence for variations in the sulfur environment at the exposed CdTe areas, despite the different stress treatments, and the sulfur is found to be predominantly in a CdS environment, suggesting that it does not diffuse to the CdTe surface. Chlorine is also found in the near-surface bulk of both areas, and is found to preferentially form Cu-Cl bonds under the back contact with exposure to sunlight during heating. In the exposed CdTe areas, chlorine is found to reside predominantly in an oxidized state, independent of heat stress treatment.

6.5 References

(1) Horsley, K.; Wilks, R. G.; Hanks, D.; Pookpanratana, S.; Blum, M.; Yang, W.; Paudel, N.; Compaan, A.; Bar, M.; Weinhardt, L.; Heske, C. In *2012 38th IEEE Photovoltaic Specialists Conference (PVSC)*; 2012; pp. 000400–000405.

(1) *First Solar builds the highest efficiency thin film PV cell on record*; Tempe, AZ, August 5, 2014.

(3) Bätzner, D. L.; Romeo, A.; Zogg, H.; Wendt, R.; Tiwari, A. N. *Thin Solid Films* **2001**, *387*, 151–154.

(4) Corwine, C. R.; Pudov, A. O.; Gloeckler, M.; Demtsu, S. H.; Sites, J. R. *Sol. Energy Mater. Sol. Cells* **2004**, *82*, 481–489.

(5) Visoly-Fisher, I.; Dobson, K. D.; Nair, J.; Bezalel, E.; Hodes, G.; Cahen, D. *Adv. Funct. Mater.* **2003**, *13*, 289–299.

(6) Liu, X.; Paudel, N.; Compaan, A.; Sun, K.; Weinhardt, L.; Bär, M.; Pookpanratana, S.; Heske, C.; Fuchs, O.; Yang, W.; Denlinger, J. D. In *2009 35th IEEE Photovoltaic Specialists Conference (PVSC)*; 2009; Vol. 35th, pp. 02107–02110.

(7) Seah, M. P.; Dench, W. A. *Surf. Interface Anal.* **1979**, *1*.

(8) Pookpanratana, S.; Khan, F.; Zhang, Y.; Heske, C.; Weinhardt, L.; Bär, M.; Liu, X.; Paudel, N.; Compaan, A. In *2010 36th IEEE Photovoltaic Specialists Conference (PVSC)*; 2010; Vol. 36th, pp. 24–27.

(9) NIST X-ray Photoelectron Spectroscopy (XPS) Database, Version 4.1 http://srdata.nist.gov/xps/ (accessed Mar 5, 2014).

(10) Powell, C. J.; Jablonski, A. *NIST Electron Effective-Attenuation-Length Database, Version 1.3, SRD 82*; National Institute of Standards and Technology: Gaithersburg, MD, 2011.

(11) X-Ray Attenuation Length http://henke.lbl.gov/optical_constants/atten2.html (accessed Mar 2, 2012).

(12) Pookpanratana, S.; Liu, X.; Paudel, N.; Weinhardt, L.; Bär, M.; Zhang, Y.; Ranasinghe, A.; Khan, F.; Blum, M.; Yang, W.; Compaan, A.; Heske, C. *Appl. Phys. Lett.* **2010**, *97*, 172109.

(13) Heske, C.; Groh, U.; Fuchs, O.; Umbach, E.; Franco, N.; Bostedt, C.; Terminello, L. J.; Perera, R. C. C.; Hallmeier, K. H.; Preobrajenski, A.; Szargan, R.; Zweigart, S.; Riedl, W.; Karg, F. *Phys. Status Solidi A* **2001**, *187*, 13–24.

CHAPTER 7

THE IMPACT OF ANNEALING ON THE CHEMICAL STRUCTURE AND MORPHOLOGY OF THE THIN-FILM CdTe/ZnO INTERFACE

The sample set and subsequent data shown in Chapter 7 were a result of combined collaboration with Dr. Russel Beal and the group of Prof. B. G. Potter at the University of Arizona, and Dr. Regan Wilks and the group of Prof. Marcus Bär at the HZB. The data and text presented here have been published in a co-authored work in the Journal of Applied Physics.[1]

7.1 Introduction

Nanocomposites are of interest due to their optical and electronic properties, which can be tailored on the nanoscale by adjustments to the deposition parameters, or post-deposition treatments. A discussion of the band gap of nanoparticles and the nanoparticle-to-wide band gap material interface was presented in Chapter 2. While Ge:ITO and Ge:ZnO interfaces were specifically mentioned,[2] many other semiconductor nanomaterials have also been previously combined with wide band gap oxides to produce nanocomposite material systems, e.g., Ge and TiO_2,[3] CdSe and ZnO,[4] and Ge and SiO_2[5]. Recently, the combination of CdTe and ZnO has also been investigated.[6–9]

CdTe- and ZnO-based nanocomposite materials (and many other material systems) have been produced using RF sputter deposition of alternating layers of the semiconductor and the wide-gap material.[5,8–12,2] This allows the nanocomposite thin-films to be produced at high speed using established technologies, while offering control of the

nanoparticle size and spatial distribution within the matrix of the wide-gap material. Such control is important for the potential of CdTe-ZnO nanocomposites to enhance the performance of photovoltaic devices by allowing for a variation of the absorption onset[8,9] and an increased photoresponse from the nanocomposite films.[9] Further tuning of the material properties can be realized by annealing the sputter-deposited nanocomposite stacks, which has been shown to increase crystallinity without affecting the absorption onset.[8]

The material interfaces in these nanocomposite systems are of great importance for the final efficiency of a potential device, especially due to the high semiconductor-to-matrix interface area. Evidence of an oxide potential barrier at the semiconductor-ITO interface has been reported previously for Ge-based composites.[2] The presence of an oxide layer at the nanoparticle-matrix interface could result in an energy barrier with significant impact on the charge transport through this interface.

To further investigate the chemical environment at the CdTe/ZnO interface, as well as the morphology of CdTe thin films on a ZnO substrate, a sample series was studied of CdTe thin films with varying thickness deposited on 100 nm ZnO on Si(100) substrates, following the deposition parameters for CdTe-ZnO nanocomposite thin films reported earlier,[8,9] including an annealing treatment. The chemical environment and morphology at the surface of the samples before and after annealing was investigated using XPS, XAES, EDX, SEM, and AFM. Particular emphasis in the data and discussion is placed on an analysis of Cd and Te surface composition, surface topography, and oxide formation after annealing.

7.2 Experimental Description

All samples were prepared at the University of Arizona by Dr. Russel Beal using a multi-source sequential RF sputtering deposition apparatus described previously.[13] Planar sputtering sources (diameter = 2 in.) were used with polycrystalline target materials (AJA International, 99.99 % purity). An RF (13.56 MHz) power of 42 W and 15 W were applied to the ZnO and CdTe sources, respectively. The chamber was pumped down to a base pressure of 10^{-6} mbar before backfilling with ultra-high purity argon (99.999 %) to a process pressure of 5×10^{-3} mbar. These conditions produced a deposition rate of 0.1 nm/s for each source under the target-substrate geometries used, as determined by a quartz crystal thickness monitor. All samples produced in the present study were deposited on surface-oxidized single-crystal Si(100) without substrate heating.

CdTe films of 4, 8, 12, and 24 nm thickness were deposited on top of 100 nm ZnO. Exposure times were controlled by a stepper motor that positioned the substrate holder sequentially over the two sources. Total film thicknesses were verified after deposition with a stylus profilometer (Dektak). A total of 10 samples were produced, in addition to two "bare" ZnO references (one before and one after annealing at 525 °C). The first sample set consisted of two samples made with an 8 nm thick CdTe film, while the second sample set consisted of eight samples total, two of each CdTe film thickness. One of these samples was kept in the as-deposited state, while the duplicate of each thickness was annealed for 20 minutes at a nominal temperature of 525 °C in a muffle tube (fused silica process tube) furnace under a flowing Ar (99.9% purity) atmosphere. The annealing time was established as the time between introduction and removal of the boat from the hot zone of the furnace using a sliding rod. Note that, based on a detailed

analysis of the XPS intensities found for the annealed sample of the first sample set, it is likely that the annealing temperature in this set was somewhat lower than for the second sample set.

An Ar-filled glovebag was used to prevent air exposure while transporting the samples between the deposition chamber and the annealing furnace, and during removal from the furnace. A portion of each of the final samples was sealed in an Ar environment without air exposure and shipped to UNLV for XPS and XAES analysis with the equipment described in Section 3.2, and to HZB for SEM and EDX analysis (after air exposure) with the equipment described in Section 3.10, and with the help of Dr. Regan Wilks. All measurements were performed with a ground connection at the front surface of each sample. Non-contact mode AFM (Bruker Innova) analysis of the remaining portion of each of the second-set samples was performed at the University of Arizona. Various scan ranges (from 1 to 50 μm in each direction), a scan rate of 0.4 Hz, and 256 lines per image were used.

7.3 Results and Discussion

Fig. 7.1 shows the XPS Mg K_α survey spectra of all CdTe/ZnO samples from the second sample set before and after annealing. The spectra are labeled according to the nominal CdTe layer thickness before annealing, and organized in order of ascending thickness from bottom to top. For each thickness, the lower spectrum represents the non-air exposed sputter-deposited surface (denoted "As-deposited"), while the upper spectrum was taken from the sample annealed at 525 °C for 20 minutes (denoted "Annealed"). The spectra were normalized to give approximately equal peak height for the Cd $3d_{5/2}$ peak in

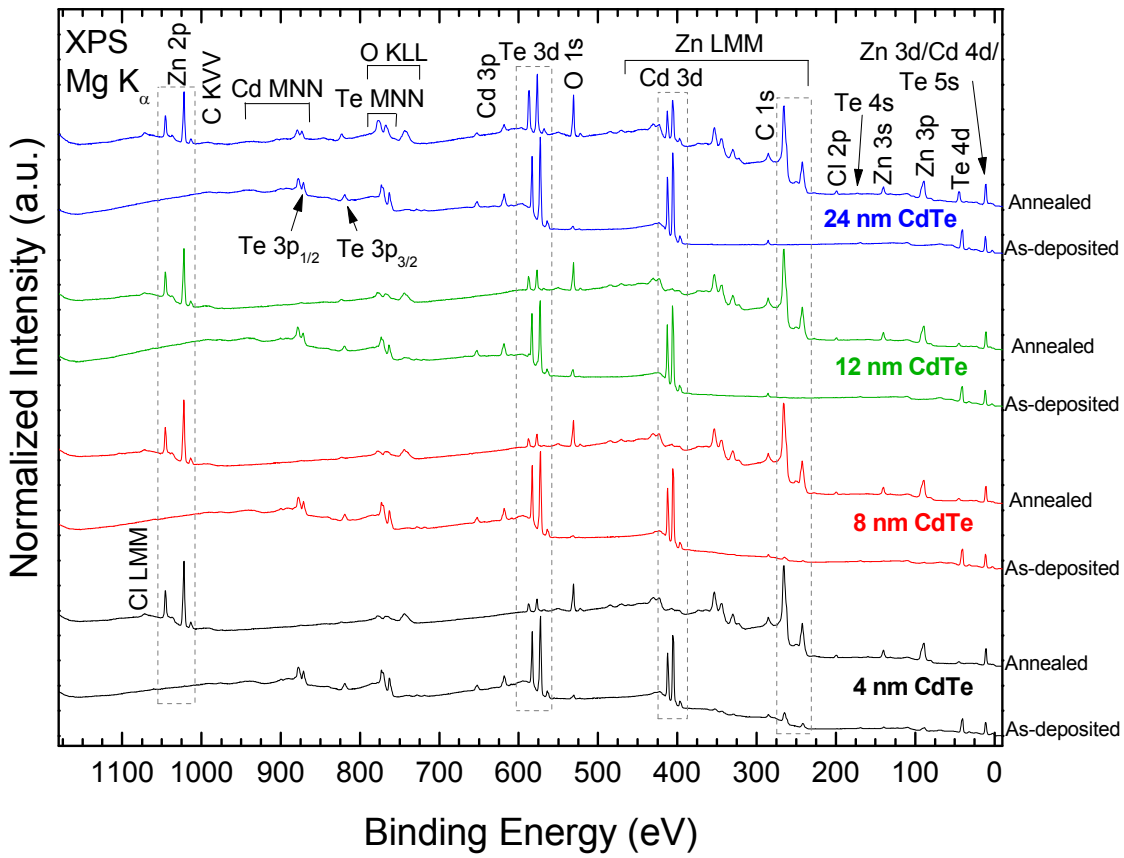

Fig. 7.1: Mg K_α XPS survey spectra of the 4, 8, 12, and 24 nm thick CdTe films on ZnO deposited on surface-oxidized Si(100) substrates, "As-deposited" and "Annealed" (at 525°C). The spectra were normalized to give approximately equal peak height for the Cd $3d_{5/2}$ peaks in the "As-deposited" spectra and for the most prominent Zn LMM peak in the "Annealed" spectra.

the "As-deposited" spectra and for the most prominent Zn LMM peak in the "Annealed" spectra, respectively.

The expected peaks of Cd and Te dominate the "As-deposited" spectra. Peaks associated with ZnO are very weak and only seen for the samples with thinner CdTe films. In detail spectra taken with Mg K_α excitation (shown in Figure 7.10), we find evidence for weak Zn LMM Auger peaks (around 265 eV binding energy) for the 4, 8,

and 12 nm, but not for the 24 nm sample, while the more surface-sensitive Zn $2p_{3/2}$ peak at 1022 eV binding energy can only be seen on the 4 nm sample. All "As-deposited" spectra exhibit small C and O peaks. In the case of carbon, we ascribe the peaks to adventitious surface adsorbates, and the low peak intensity indicates that the packing procedure was successful in transferring samples with minimal ambient exposure. The oxygen peaks are also mostly due to adventitious adsorbates, but for the thinner CdTe-film samples, some contribution from the underlying ZnO is also expected (scaling with the observed Zn peak intensities). The inelastic mean free path of a 780 eV kinetic energy (KE) O 1s electron in CdTe is ~2 nm.[14] Therefore, 1/e (i.e., ~36%) of the original O intensity from the underlying ZnO would be expected after attenuation in a 2 nm thick CdTe layer (in normal emission geometry). Similary, ~14% and ~2% of the initial signal are expected after attenuation in a 4 and 8 nm thick CdTe layer, respectively.

In all "Annealed" spectra, the previously dominant Te 3d peaks [~580 eV binding energy, (BE)] are greatly reduced in intensity and, as will be discussed below, shifted to higher BE. The Cd 3d peaks (~410 eV BE) show an even stronger reduction in intensity, in particular for the samples with thinner CdTe. Only the 24 nm sample shows a Cd signal after annealing that is significant enough to be distinguished in the survey spectra.

In parallel with the Cd- and Te-signal reduction, all Zn-related signals are increased substantially on the annealed samples, most clearly seen by the Zn 2p doublet (~1022 and ~1045 eV BE) and the Zn LMM Auger region (most prominent peak at ~265 eV BE). In parallel, all oxygen-related peaks (e.g., the O 1s peak at 530 eV BE) are increased. We note that there is no evidence for a significant increase of the C 1s signal, indicating that the additional oxygen content at the surface is most likely not due to

further adventitious surface adsorbates, but rather to the underlying (possibly chemically modified) ZnO. As will be discussed below, the annealing step changes the morphology of the CdTe layer, and hence the underlying ZnO may contribute more strongly to the peak intensity. Also, an oxidation of Cd and/or Te by oxygen from the ZnO film and/or the annealing environment is possible, as will be discussed below. Note that a small Cl 2p signal is seen on all samples after annealing, most likely from the polyethylene glove-bag that was used to transfer the samples into and out of the tube furnace, as this showed signs of heat damage after use (and possibly contains residues of polymerization catalysts such as titanium (III) chloride).

The strong reduction in the Cd and Te signal intensities and increase in the Zn and O signal intensities after annealing suggest significant changes to the CdTe layer topography. First, this effect might be seen with a loss of Cd and Te from the surface of the samples, either by sublimation and/or diffusion into the ZnO bottom layer. Second, a morphology change of the CdTe layer appears possible, e.g., the creation of Cd- and Te-containing islands and the exposure of intermittent regions of ZnO (or ZnO covered with a thinner CdTe layer). Finally, the increased oxygen signals might indicate oxidation-related modifications at the surface.

To understand the changes observed in the XPS survey spectra, we will in the following focus on the surface morphology and lateral element distribution before and after annealing. Afterwards, we will discuss the chemical and electronic modifications visible in the XPS and Auger detail spectra.

Figure 7.2 shows AFM images (5×5 μm^2) of all samples, before (left) and after (right) the annealing step. The images of the 8 nm CdTe film are divided into two

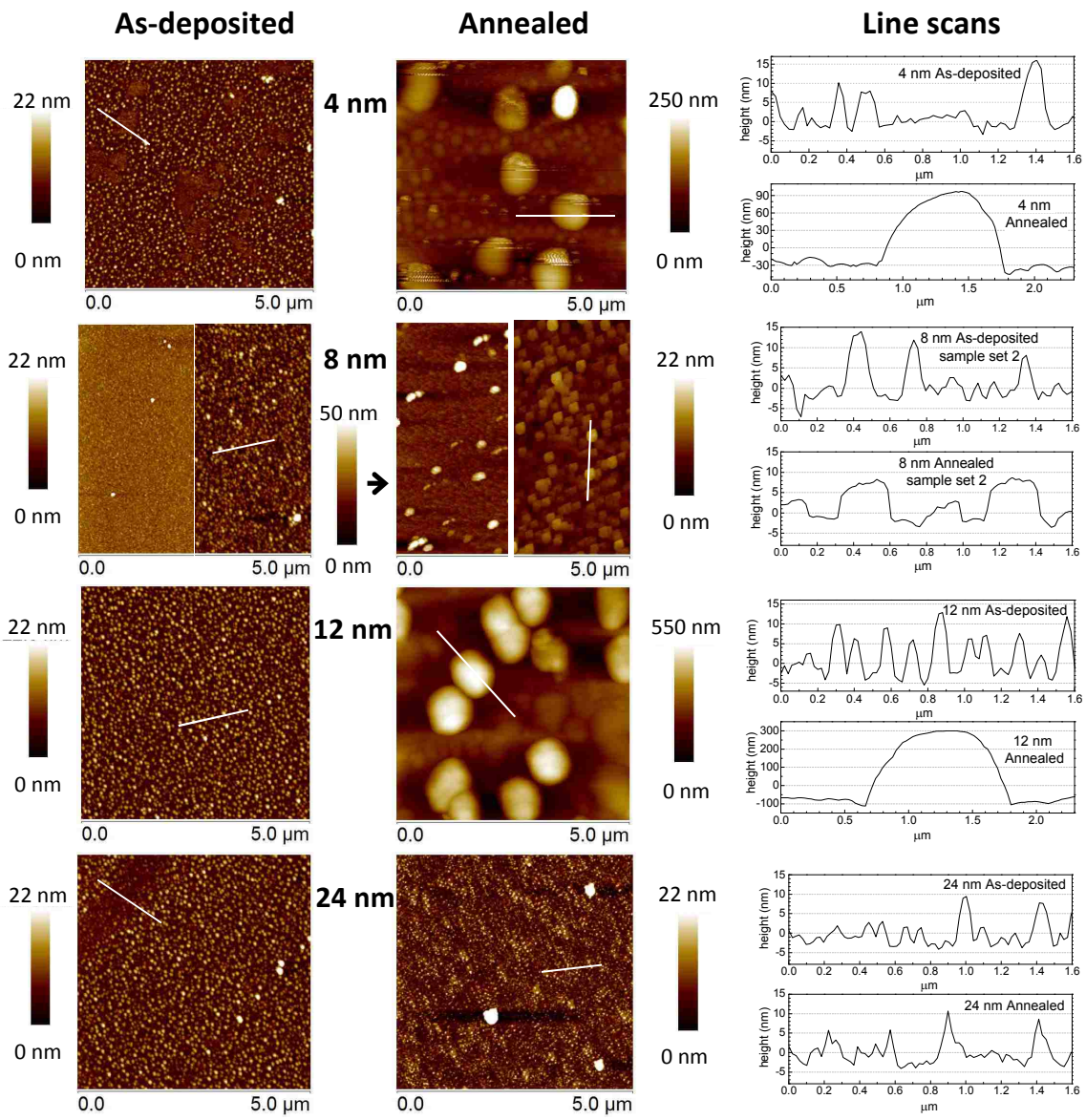

Fig. 7.2: AFM images (5×5 µm^2) of the CdTe/ZnO film surfaces with different CdTe thickness (4, 8, 12, and 24 nm), "As-deposited" (left) and "Annealed" (right). The images of the 8 nm CdTe film are divided into two portions to show the 8 nm sample from the first (left) and second (right) sample set. A line scan from each image (indicated by the white line) is shown on the right.

portions to show the 8 nm sample from the first (left) and second (right) sample set. While the as-deposited surfaces are characterized by small, uniform grains of approximately 100 nm diameter and 10 nm height (and 80 nm diameter and 3 nm height

for the 8 nm film from the first sample set, with a few larger grains of approximately 110 nm diameter and 15 nm height), significant enlargement and separation of the grains is observed after annealing of the 4, 8, and 12 nm CdTe film samples (see Table 7.1 for a complete overview of all grain sizes).

On the "As-deposited 4 nm" sample surface, we note areas in which a smoother morphology is found, compared to both the regions surrounding these areas on the film and the surfaces of all thicker CdTe films in this sample set. These regions may represent exposed areas of the underlying ZnO layer or areas with a thin (wetting) layer of CdTe that did not develop a larger grain structure. The 24 nm sample shows a similar "darker" region, but close inspection indicates that grains similar to the rest of the surface are present in this region, too, and thus it is more likely due to an overall depression in the substrate.

The approximate grain sizes of annealed samples are also listed in Table 7.1. After annealing, the smallest grain diameters are found for the 8 nm samples (~230 nm in diameter and 35 nm in height for the sample from the first set, and ~260 nm diameter and 7 nm in height for the sample from the second set), while the 4 and 12 nm samples

Table 7.1: Most often found approximate grain sizes in the AFM images in Fig. 7.2 for the "As-deposited" and "Annealed" 4, 8, 12, and 24 nm CdTe samples.

Sample	**Approximate grain width × height (nm)**	
	As-deposited	**Annealed**
4 nm CdTe	100 × 10	1000 × 100 and 270 × 15
8 nm CdTe, set 1	80 × 3 and 110 × 15	230 × 35 and 75 × 3
8 nm CdTe, set 2	100 × 10	260 × 7
12 nm CdTe	100 × 10	1000 × 380 and 150 × 15
24 nm CdTe	100 × 10	100 × 10 and 300 × 30

exhibit distinct islands up to 1 μm wide and 100 nm (4 nm sample) or 380 nm (12 nm sample) high. In between these features on the 4 and 12 nm samples, smaller grains are visible that are approximately 270 nm (4 nm sample) or 150 nm (12 nm sample) in diameter and 15 nm high. Smaller grains are also visible between the enlarged grains on the 8 nm sample from the first sample set, which are approximately 75 nm in diameter and 3 nm high.

The morphology of the 24 nm CdTe film sample after annealing deviates from the other samples in that, aside from a small number of very large features of approximately 300 nm width and 30 nm height, the grains at the surface maintain their initial size after annealing. This sample also varied from the other samples in the XPS survey spectra in Fig. 7.1, in that a significant amount of Cd was still present at the surface after annealing. This suggests that a larger portion of the Cd and Te atoms remain at the surface after annealing, likely forming CdTe grains of similar magnitude as before annealing, while all other annealed samples (i.e., without an appreciable amount of Cd remaining at the surface) exhibit a very different chemical structure and surface (island) morphology.

To identify the chemical nature of the islands after annealing, we have followed two approaches. First, using the "Annealed 8 nm" sample from the first sample set, we conducted a combined SEM/EDX investigation, in which a small region of the sample surface was imaged for morphology (SEM) and element distribution of Zn, O, Cd, and Te (EDX maps). The results are shown in Fig. 7.3 and will be discussed in the following. Second, we used the "Annealed 12 nm" sample from the second sample set to record EDX *spectra* at two different sample locations, namely on a post-anneal island and next

to it (as indicated by the corresponding SEM image). This will be shown and discussed later (Fig. 7.4).

Figure 7.3 shows an SEM image (top left) of a region on the 8 nm sample (first sample set) after annealing, within which several island features are observed. The elemental EDX maps depict the Zn L, O K, Cd L, and Te L emission intensities. In all maps, we find evidence for elemental distribution inhomogeneities on the sample surface, which, for Zn, Cd, and Te correspond to the features seen in the SEM image. For example, the largest island at the top left of the region of study is also the most prominent in the respective elemental maps. For the Zn L emission, and possibly O K emission, this island is seen as an area of reduced intensity, while increased intensity is observed at this location in the Cd and Te element maps. The Cd and Zn elemental maps show the most pronounced intensity variations, and the smaller islands can also easily be seen. Based on

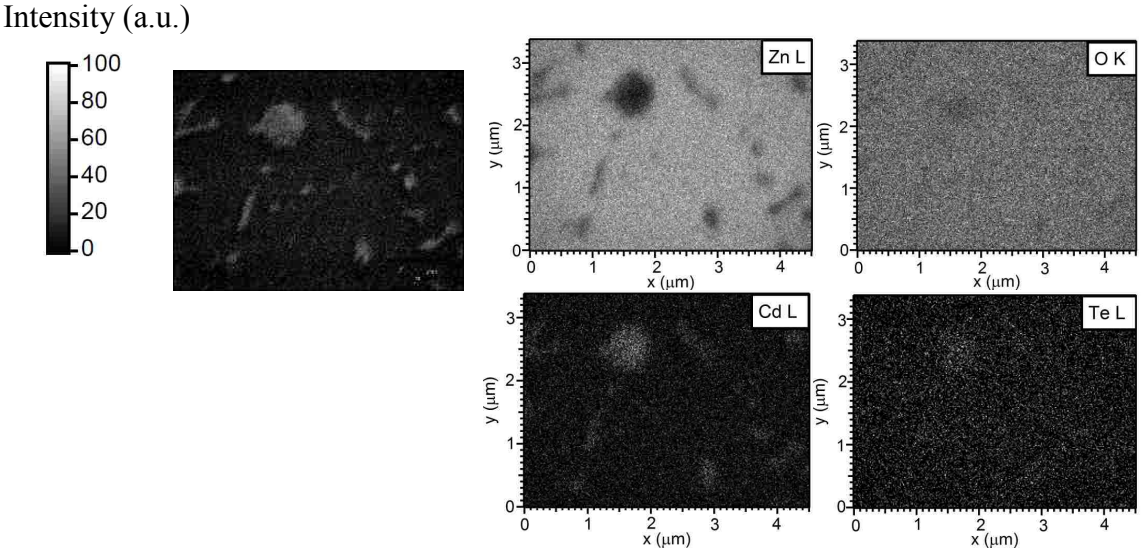

Fig. 7.3: SEM (top left) and EDX images for Zn, O, Cd, and Te, taken on the "Annealed 8 nm" sample from the first sample set.

the EDX maps, we find the islands to be rich in Cd and Te. The Zn content is substantially lower in the regions of the islands than in the surrounding environment, suggesting that the Zn emission from the underlying ZnO film is strongly attenuated by the islands.

Figure 7.4 shows the SEM image of the "Annealed 12 nm" CdTe sample surface and EDX spectra, taken *on* (labeled "Feature" and shown in black) and *next to* (labeled "Background" and shown in red) an island. Below 1.9 keV, the EDX spectra show the C K, O K, Zn L, and Si K emission peaks. Above 2.4 keV, the intensity has been magnified to allow viewing of the weaker Cd L and Te L transitions.[15]

The "Feature" spectrum shows a reduction in Zn and Si intensity compared to the "Background" spectrum, and an increase in O. The reduced intensities suggest an attenuation of the underlying ZnO layer and Si substrate, while the increased O signal suggests the presence of oxides on (or in) the "Feature" island. The C signal is comparable in both spectra.

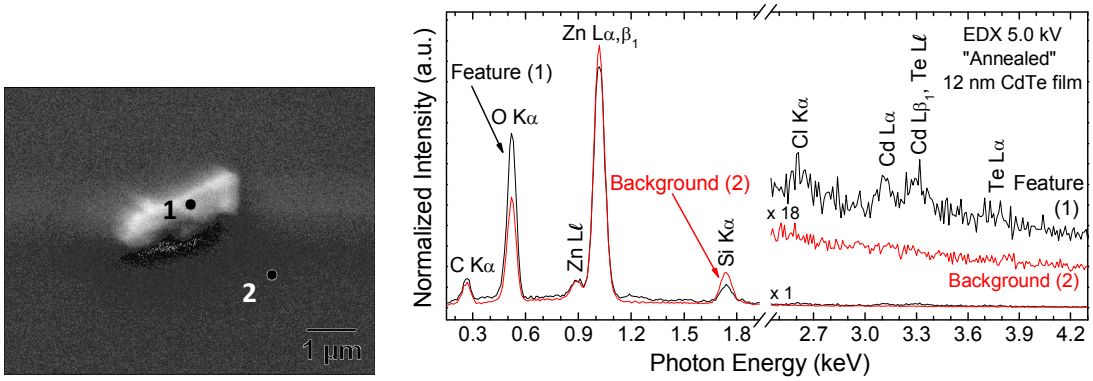

Fig. 7.4: SEM image (left) and EDX spectra (right), taken on the "Annealed" 12 nm CdTe film. The black "Feature" spectrum corresponds to point 1, while the red "Background" spectrum was taken at point 2 on the SEM image.

While the region from 2.5 to 4.5 keV shows no peaks for the "Background" spectrum, the "Feature" spectrum displays a number of emission lines, most notably the Cd L_α (~3.1 keV) and Te L_α (~3.8 keV) transitions.[15] The peak at ~3.3 keV is attributed to a combination of Cd L_β and Te L_ℓ. The peak at ~2.6 keV is ascribed to Cl K_α emission, in agreement with the XPS survey spectra in Fig. 7.1, which show a small Cl peak at the surface of all annealed samples. The presence of Cd and Te signals on the "Feature" island and the absence of these peaks on the "Background" further supports the above-described island formation of the CdTe layer after annealing.

Thus, so far, we have determined that annealing leads to the formation of islands and the reduction (or removal) of Cd and Te signals from the surface. The islands are Zn poor, Cd and Te rich, oxidized, and contain some Cl contaminants. To further investigate the chemical environment of the Cd and Te atoms remaining at the surface, detailed XPS and XAES spectra were taken and are discussed in the following.

Fig. 7.5 shows the detailed Mg K_α-excited Te $3d_{3/2}$ XPS (left) and Te $M_{4,5}N_{4,5}N_{4,5}$ XAES (center) spectra, measured on the "As-deposited" (bottom) and "Annealed" (top) samples. A two-component fit of each "Annealed" Te MNN spectrum, after subtraction of the overlapping O KLL contribution, is also shown (right). All spectra are normalized to the most intense transition in each region, except for the O KL_1L_1 and $KL_1L_{2,3}$ contributions shown in the center panel, which scale with the intensity of the O $KL_{2,3}L_{2,3}$ emission at 509.5 eV kinetic energy (KE). All fits and additional spectra shown are described in detail below.

For the as-deposited samples, the Te $3d_{3/2}$ XPS peaks are found at a BE of 583.0 eV. A shift in the peak location of the "As-deposited 12 nm" samples was observed for

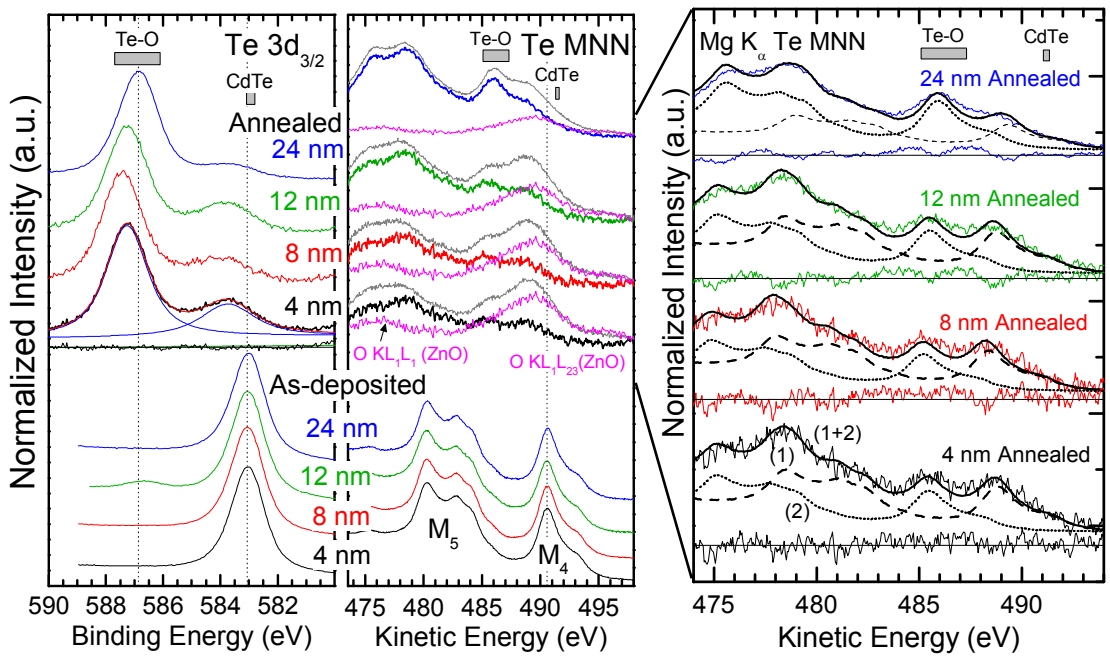

Fig. 7.5: Mg K_α-excited spectra of the Te $3d_{3/2}$ XPS (left) and Te $M_{4,5}N_{4,5}N_{4,5}$ XAES (center and right) regions of the "As-deposited" (bottom) and "Annealed" (top) CdTe/ZnO/Si sample surfaces. For the Te $3d_{3/2}$ region, the fit (including residuum) of the "Annealed 4 nm" sample is shown as an example. The Te MNN raw spectra of the "Annealed" samples (grey), their O $KL_1L_{2,3}$ contributions (pink, lineshape taken from a ZnO reference), and their difference (bold) are shown in the center panel. On the right, each difference is fit with two Te MNN spectra (lineshape taken from the "As-deposited 24 nm" sample). The grey bars (top) indicate literature values for CdTe and compounds containing Te-O bonds, from Refs. 18, 21, 22, and 26.

all peaks (+0.4 eV relative to the 4, 8, and 24 nm samples). All spectra shown for this sample have thus been shifted by -0.4 eV BE to correct for this. A second, small peak at a BE of 586.6 eV is also present in the Te $3d_{3/2}$ region for this sample. For the "Annealed" sample spectra, we observe two peaks, the first at ~583.7 eV and the second, more intense, at ~587.2 eV. Small variations in peak position between samples are present, with the "Annealed 8 nm" sample shifted by +0.2 eV and the "24 nm" sample shifted by -0.4 eV relative to the 4 and 12 nm samples. Contrary to the shifts in the "As-deposited"

spectra discussed above, these shifts are not uniform for the various XPS and XAES lines. We speculate that they could be due to size-dependent effects of small particles distributed on an oxide layer[16] since the grain sizes observed after annealing (see Fig. 7.2) correlate with the magnitude of the peak shifts (the "Annealed 8 nm" sample shows the smallest particles and the strongest shift to higher BE). The Te $3d_{3/2}$ peak position in the "As-deposited" spectra matches earlier reports for CdTe,[17,18] while the prominent peaks in the "Annealed" spectra are indicative of an increase in the oxidation state of Te similar to that of TeO_2[17,18] or $CdTeO_x$ species (such as $CdTeO_3$ or $CdTe_2O_5$[19,20]). The "Annealed" spectra also show that some Te remains in a CdTe-like environment, indicated by the peak at lower BE. Both peaks in the "Annealed" spectra are broadened compared to their "As-deposited" counterparts, suggesting a less defined chemical environment after annealing.

The Te MNN regions of all samples are shown in the center panel of Fig. 7.5. While the overall shape and position of the "As-deposited" spectra matches to chemically well-defined CdTe reference spectra,[17,21] the analysis of the Te MNN region for the "Annealed" spectra is more complicated. These spectra represent a superposition of the Te $M_{4,5}N_{4,5}N_{4,5}$ emission of (at least) two Te species, as indicated in the XPS spectra in the left panel. Furthermore, the O $KL_1L_{2,3}$ and KL_1L_1 signals in this region are more intense (in agreement with the annealing-induced overall increase of all oxygen-related signals, see, e.g., the O 1s in the XPS survey spectra in Fig. 7.1). To isolate the Te MNN signal, the O $KL_1L_{2,3}$ and KL_1L_1 signals of a ZnO reference were scaled with the O $KL_{2,3}L_{2,3}$ intensity at 509.5 eV KE (not shown) and subtracted, as mentioned above. The

"Annealed" spectra (grey), the O KLL spectrum that was subtracted (pink), and the remaining, now-isolated Te MNN signals (bold) are shown in the center panel of Fig. 7.5.

To evaluate the Te environment of the annealed samples, fits were performed of the Te $3d_{3/2}$ and Te MNN regions. The Te $3d_{3/2}$ peaks of all "Annealed" spectra were fit simultaneously using a pair of Voigt profiles to describe each spectrum. The positions and intensities of the peaks were allowed to vary freely, while the Gaussian broadening was coupled for all peaks and the Lorentzian broadening was coupled for each chemical environment. In Fig. 7.5, the fit of the "Annealed 4 nm" Te $3d_{3/2}$ spectrum together with the respective residuum (difference between data and fit) is shown as an example. In the right panel of Fig. 7.5, two "As-deposited 24 nm" Te MNN spectra were used as reference spectra to describe each "Annealed" Te MNN spectrum. For a first estimate, the two reference spectra were separated by the BE difference derived from the fit of the two Te $3d_{3/2}$ XPS peaks. Then, in a second step, their separation was used as a free fit parameter (leading to shifts between -0.2 and +0.3 eV). The two weighted Te MNN contributions (as determined by the fit), the resulting sum of these spectra, and the measured "Annealed" Te MNN spectra are shown in the right panel of Fig. 7.5. The residual is shown below each set of spectra. Grey bars indicating the range of literature values for CdTe and compounds containing Te-O bonds (e.g., TeO_2, $Te(OH)_6$, $CdTeO_3$, etc., denoted "Te-O") are included at the top of the graph.

The fits of the "Annealed" Te MNN spectra show the intensity of the two components to be almost equal to one another, suggesting that nearly 50% of the Te in the probed volume is oxidized. In contrast, the "Te-O" peak in the Te $3d_{3/2}$ XPS spectra is clearly dominant for all annealed samples. To quantify this observation, the fraction of

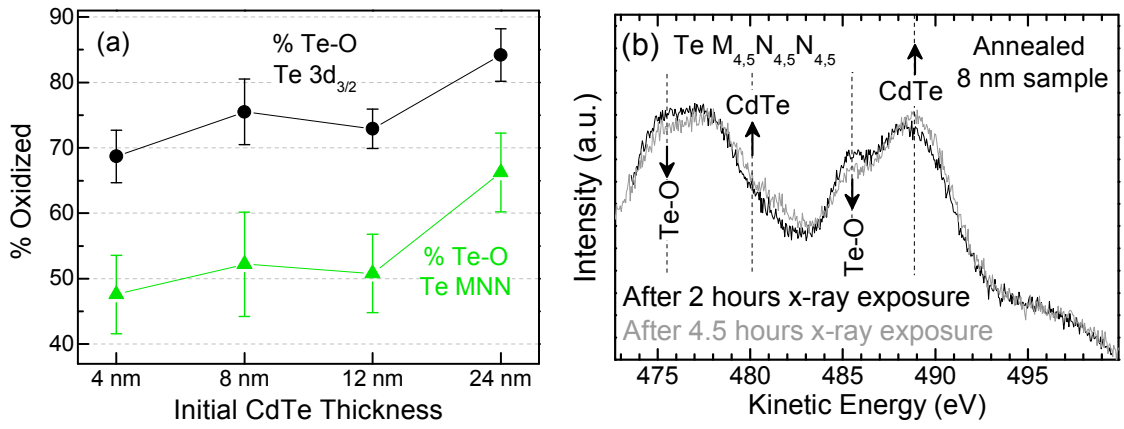

Fig 7.6. (a) Percent of the total Te signal coming from the "Te-O" peak in both the Te $3d_{3/2}$ region and the Te MNN region. (b) A reduction of the Te-O species was observed as a function of time under x-ray exposure.

Te-O was determined from the area of the "Te-O" peak in the Te $3d_{3/2}$ and MNN regions relative to the total Te signal (i.e., combined area of the "CdTe" peak and the "Te-O" peak). The results, plotted in Fig. 7.6 (a), show a trend of reduced oxidation for the Te MNN region, with a difference of 18-23% for all samples. We speculatively assign this difference to three effects. First, we note that the subtraction method employed to derive the "isolated" Te MNN spectra is simple and inherently connected to a significant degree of uncertainty. Second, we compare two spectral regions with two different kinetic energies and hence different degrees of surface sensitivity. We would roughly expect the inelastic mean free path of the XPS signal to be larger than that associated with the Auger signal by a factor of $\frac{\sqrt{670}}{\sqrt{480}} = 1.18$ (using the approximate KE for the Te 3d and Te MNN, respectively, and a square root dependence for the "universal" inelastic mean free path[22]). Third, and possibly most prominently, we observe a reduction of the "Te-O"/"CdTe" ratio as a function of x-ray exposure. This is exemplarily shown for the "Annealed 8 nm" sample in Fig. 7.6 (b). The black spectrum was taken after 2 hours of x-ray exposure,

while the grey spectrum was taken 2.5 hours after the black spectrum (i.e., after 4.5 hours of x-ray exposure). After subtraction of the O KLL contribution, a fit of the grey spectrum shows an 11 % (absolute) reduction in the Te-O species relative to the black spectrum (which is also easily seen in the raw spectra, as indicated by the arrows), and an even larger relative reduction would be expected when comparing with the pristine surface (data not available. Our measurement cycle included the XPS and XAES measurements with a time separation of ca. 2-3 hours, and all XAES data was therefore taken at a later stage of the x-ray-induced Te-O reduction. Nevertheless, the here-presented analysis of the different Te species, the presence of a dominant tellurium oxide species, and the finding of island formation upon annealing is independent of this effect and hence remains fully valid.

The Te MNN reference spectra (i.e., the "As-deposited 24 nm" spectra) had to be shifted by an additional amount towards lower KE relative to the position of the "As-deposited" Te MNN spectra to achieve the fits shown. This amount varied for each sample, from 0.66 eV for the "Annealed 24 nm" spectrum to 1.13 eV for the "Annealed 8 nm" spectrum. This additional shift is speculatively attributed to the increased Coulomb interaction of the double vacancy final state of the $M_{4,5}N_{4,5}N_{4,5}$ transition due to the nano-size dimensions of the CdTe grains,[16] similar to the earlier discussion of the XPS core levels. Again, a larger shift would be expected for smaller grain sizes, and the magnitude of the required additional shift agrees with the grain sizes in the AFM images in Fig. 7.2. This interpretation also sheds light on the peak broadening observed for all "Annealed" Te 3d XPS peaks compared to the "As-deposited" spectra, in that a distribution in grain size at the surface would lead to a less-defined chemical state for each sample.

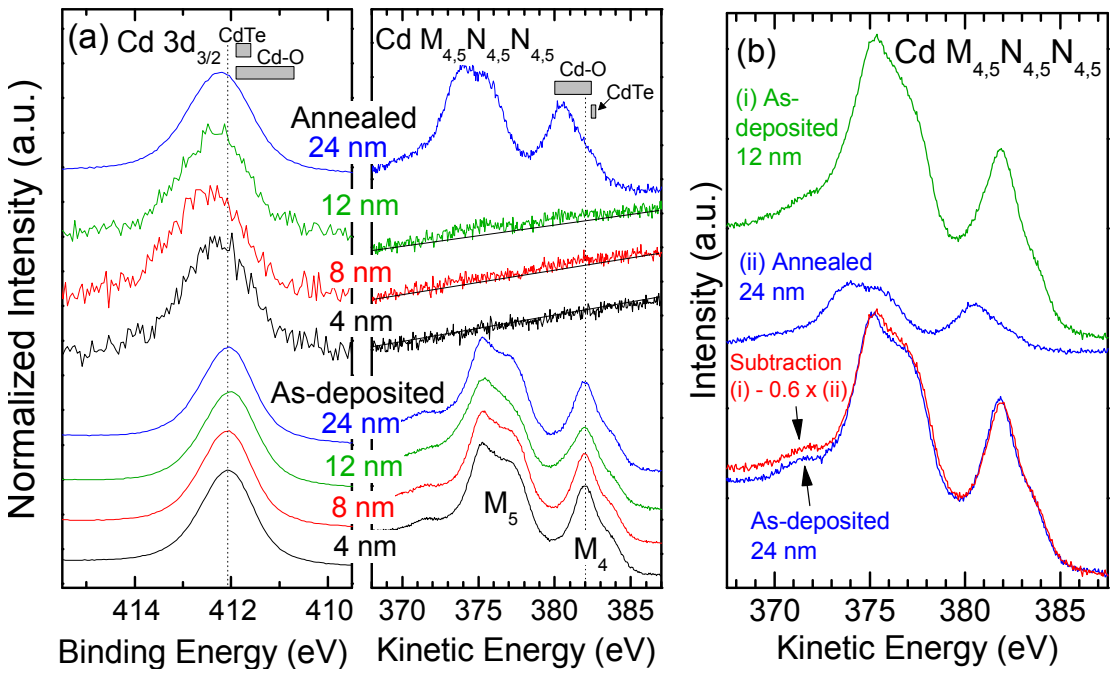

Fig. 7.7: (a) Al K_α-excited XPS and XAES spectra of the Cd $3d_{3/2}$ (left) and Cd $M_{4,5}N_{4,5}N_{4,5}$ (right) regions taken from the "As-deposited" (bottom) and "Annealed" (top) CdTe/ZnO/Si sample surfaces. The grey bars (top) indicate literature values for CdTe and compounds containing Cd-O bonds, from Refs. 18, 21, 22, and 26. (b) The "As-deposited 12 nm" spectrum is shown as-measured (i), along with the "Annealed 24 nm" spectrum (ii). After subtraction of 60% of spectrum (ii), the remainder of the "As-deposited 12 nm" spectrum most closely resembles the other as-deposited samples. The "As-deposited 24 nm" is shown for reference.

Detailed Al K_α-excited XPS and XAES spectra of the Cd $3d_{3/2}$ (left) and Cd $M_{4,5}N_{4,5}N_{4,5}$ (right) regions, respectively, are shown in Fig. 7.7 (a). All spectra are normalized to the intensity of the strongest transition in each region (except for the annealed 4, 8, and 12 nm CdTe samples, which exhibit extremely low intensity).

The Cd $3d_{3/2}$ peak is found at 412.0 eV BE for all "As-deposited" spectra, while all "Annealed" spectral peaks exhibit broadening and a small shift to higher BE relative to the "As-deposited" spectra. The largest shift is seen for the "Annealed 8 nm" spectrum,

with the Cd $3d_{3/2}$ peak appearing at 412.5 eV. The broadening of the peak shape is most apparent when comparing the "Annealed 24 nm" spectrum to the "As-deposited 24 nm" spectrum, but can also be seen for the "Annealed" 4, 8, and 12 nm spectra, despite their low Cd signal.

The energy shifts and peak broadening correlate with the Te $3d_{3/2}$ data in Fig. 7.5, showing that the Cd remaining at the surface is also in a less-defined chemical state after annealing. In comparison to the chemical shifts of Te core levels, the shifts for Cd core levels upon oxide formation are often much smaller (BEs for CdTe, CdO, and $Cd(OH)_2$ overlap within their reported ranges, while only CdO_2 shows an appreciable chemical shift of ~1.0 eV[21]). Grey bars at the top of Fig. 7.7 demonstrate the range of literature values for CdTe and compounds containing Cd-O bonds (designated "Cd-O"). The observed peak shifts and broadenings could therefore be due to the presence of multiple chemical species, such as CdTe and Cd-O compounds, or the nano-scale quantum-effects previously mentioned.

A strong Cd MNN signal is present for all as-deposited CdTe film thicknesses, with the $M_4N_{4,5}N_{4,5}$ transition found at 382.0 eV KE. Close inspection finds that the shape of the "As-deposited 12 nm" Cd MNN spectrum varies from the other three "As-deposited" spectra, exhibiting smeared-out features and a shallower dip between the M_4- and M_5-related transitions. No Auger signal is seen for the "Annealed" 4 and 8 nm spectra, while a small signal is observed for the 12 nm spectrum (a linear background is drawn as a guide to the eye). A strong Cd MNN signal is seen for the "Annealed 24 nm" spectrum, shifted by 1.5 eV to lower KE relative to the "As-deposited" spectra.

A similar shape variation as found for the "As-deposited 12 nm" Cd MNN spectrum was previously shown to be due to the presence of multiple Cd species, especially when an oxidized Cd species is present; an example of CdS and $Cd(OH)_2$ is shown in Ref. [23]. Since a Te-O species was also seen on this sample in the Te $3d_{3/2}$ region (Fig. 7.5), an oxidized Cd species is likely to be present here as well. The large shift of the "Annealed 24 nm" Cd MNN spectrum relative to the "As-deposited" spectra also suggests a change in the chemical environment of Cd, and the energy value of the $M_4N_{4,5}N_{4,5}$ transition (380.5 eV) is close to literature values for $Cd(OH)_2$ (380.0 eV[17]) and $CdTeO_3$ (380.8 eV[20]).

To further investigate the spectral changes seen in the "As-deposited 12 nm" Cd MNN spectrum, we note that the "Annealed 24 nm" spectrum is satisfactorily described by a single Cd-O species. By subtracting sixty percent of the "Annealed 24 nm" spectrum from the "As-deposited 12 nm" spectrum, as shown in Fig. 7.7 (b), the remainder most closely resembles a Cd MNN spectrum from a single Cd component. Furthermore, it compares well with the three other "As-deposited" spectra, as shown for the "As-deposited 24 nm" spectrum at the bottom of Fig. 7.7 (b).

To better visualize the observed peak shifts, chemical state plots were made for Te and Cd from the XPS and XAES peak locations of both elements. For the "Annealed" Te spectra, the energy of each $M_4N_{4,5}N_{4,5}$ contribution and $3d_{5/2}$ peak was determined from the previously described fits of the Te $3d_{3/2}$ and Te MNN regions (see Fig. 7.5). For the "As-deposited" Te $3d_{3/2}$ and all Cd $3d_{3/2}$ spectra, one Voigt peak and a linear background was used to describe each spectrum. The Gaussian broadening was held constant for all peaks of a particular element, while the Lorentzian broadening was

allowed to vary in order to describe the peak broadening observed for the annealed samples. Due to the overlap of the $3d_{3/2}$ contribution – excited with the $K_{\alpha 3,4}$ x-ray source satellites – with the $3d_{5/2}$ component, the $3d_{5/2}$ BE for each sample was determined from the fitted $3d_{3/2}$ BE position and the spin-orbit splitting documented in literature (10.4 eV

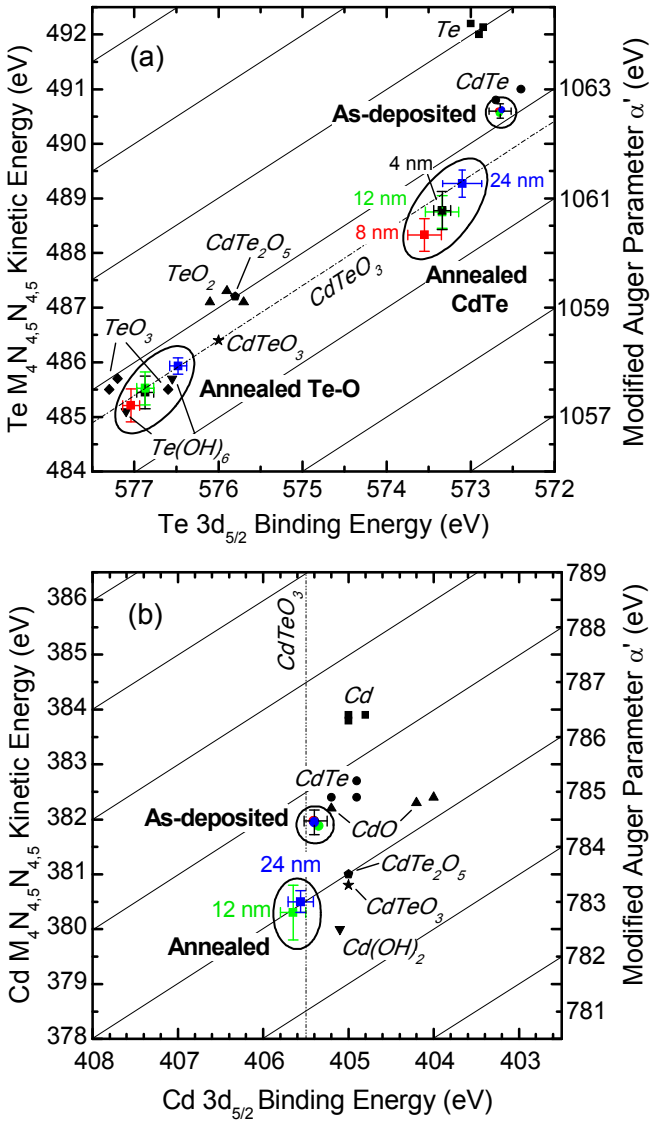

Fig.7.8: Chemical state plots for (a) Te and (b) Cd. Data points are shown along with literature values (labeled in italics) taken from Refs. 18, 21, 22, and 26. The color code for the sample data is identical to that in Figs. 7.5 and 7.7.

for Te and 6.7 eV for Cd)[24]. The KE of the $M_4N_{4,5}N_{4,5}$ peak of the "As-deposited" Te MNN samples and all Cd MNN spectra were taken as the energy at maximum intensity. The magnitude of the error associated with each value is based on the energy step size of the measurement, the intensity of the signal, the method used for finding the peak location, and the data analysis necessary to isolate the individual components (e.g., a larger error bar is derived for the "Annealed" Te MNN). The resulting data points and their error bars are plotted in Fig. 7.8, along with relevant references. All reference values were taken from [17], [21], and [25], except for the $CdTeO_3$ and $CdTe_2O_5$ data, which were taken from reference [20]. A ZnTe reference for the Te Auger parameter is not included because, to our knowledge, this data is not available from the literature. However, no evidence for the formation of ZnTe is seen from the Zn LMM region, which would show a 2.7-3.8 eV shift relative to ZnO[25] (see Fig. 7.10 below for more details).

The chemical state plot of Te is shown in Fig. 7.8 (a). The modified Auger Parameter (α', right ordinate) for all "As-deposited" samples is 1063.3 ± 0.1 eV, in very good agreement with the CdTe references. Both chemical contributions from the "Annealed" spectra are plotted, designated "Annealed CdTe" and "Annealed Te-O". All "Annealed Te-O" data points appear in the lower left corner of the plot (described by the solid ellipse), near the TeO_3 and $Te(OH)_6$ reference points, while the "Annealed CdTe" data points are located to the right, significantly closer to the "As-deposited" data points.

All "Annealed CdTe" data points (i.e., for the Te atoms in a CdTe environment after annealing) are shifted to a lower α' value relative to the "As-deposited" and the CdTe literature values. This could be due to two effects. First, the underlying assumption that a simple two-component analysis is a sufficient description of the various local

chemical environments of the Te atoms might be incorrect – if further species are required for a correct description, one or more of them could exhibit the modified Auger parameter value of CdTe. More likely, however, we believe the shifts to be due to additional *final*-state effects. Most prominently, changes in extra-atomic screening and/or the lifetime of the core- and valence-holes could be involved.[26] For example, a structural change producing small grains similar to those observed in the AFM images, and/or a loss or reduction of electrical connectivity (reduced charge transfer) between the small grains as well as between the grains and the substrate could lead to such final-state variations (note that the final state of the XPS process is a core-hole, while the final state of the Auger process involves two valence holes with an additional interaction of the two charged particles). As an indication that the island size might play a role in the observed shifts, we note that the "Annealed 24 nm" data points for both, Te-O and CdTe, are at a higher α' value than those of the other annealed samples (top right data point in each ellipse); this sample showed the smallest impact of annealing on grain size, and hence the impact of morphology-related final-state effects would be reduced.

The chemical state plot for Cd is shown in Fig. 7.8 (b). The "Annealed" 4 and 8 nm samples could not be plotted due to the absence of the Cd Auger peaks. All "As-deposited" data points are located at the α' value of 787.3 ± 0.2 eV, in the vicinity of both CdTe and CdO reference values. While all CdTe reference values (and one of the CdO references) agree well with the "As-deposited" data points, the full set of CdO reference values shows a strong variation, in particular in the $3d_{5/2}$ binding energy. A large shift in α' is present between the "As-deposited" and "Annealed" data points, the latter of which are located towards the bottom of the plot, sharing the same α' value as $CdTeO_3$ and

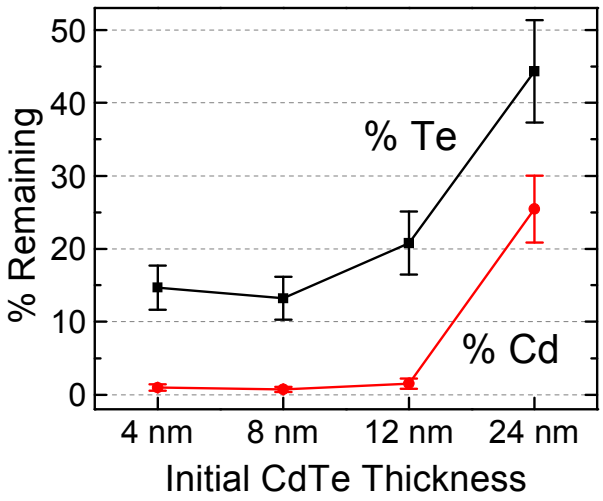

Fig. 7.9: Percent of the "remaining" Cd and Te $3d_{3/2}$ signal intensity for each thickness, given as the intensity ratio between the "Annealed" and "As-deposited" samples.

$CdTe_2O_5$ (Ref. [20]), and in line with the $CdTeO_3$ Cd $3d_{5/2}$ reference value given in Ref. [17]. The formation of $CdTeO_3$ and (to a lesser extent) $CdTe_2O_5$ has been observed in intentionally oxidized CdTe samples after annealing treatments between 300 and 550 °C,[27] i.e., comparable to the annealing temperature used here (525 °C).

The literature value for $Cd(OH)_2$ is also found in this region, making it a viable candidate as well. An exact identification of the Cd chemical environment on the "Annealed" samples is difficult, since final state effects are expected to also lead to energy shifts, as described above for the case of Te. Nevertheless, that fact that the "Annealed' data points are nearest to $CdTeO_3$, $CdTe_2O_5$, and $Cd(OH)_2$ references suggests that the remaining Cd atoms on the "Annealed" samples are in an oxidized environment with a bonding structure different from CdTe.

The percentage of Cd and Te "remaining" after annealing was calculated for all CdTe thicknesses and is shown in Fig. 7.9. To derive this percentage, the "Annealed" peak area from the previously described Cd and Te $3d_{3/2}$ fits (including all chemical

species) was divided by the "As-deposited" peak area. The error bars were estimated by considering effects such as possible variations in sample and x-ray source positioning, attenuation from surface adsorbates (i.e., C 1s intensity variation between "As-deposited" and "Annealed" samples), and variability in the fitting procedure.

A significantly greater amount of Te than Cd is retained at the surface of all annealed samples. Close to 15% of the original Te signal remains for the 4 and 8 nm CdTe thickness samples, while for Cd only ~1 % of the original signal remains. A small increase in the post-annealing Cd and Te intensity is seen for the 12 nm CdTe film, but the Cd:Te "retention" ratio is also near 1:15. As was already seen in the survey spectra of Fig. 7.1, the 24 nm CdTe "Annealed" sample shows a high Cd intensity – 25 % of the original Cd intensity is retained, while the Te intensity relative to the as-deposited sample is 44 %; the Cd:Te "retention" ratio is thus closer to ~1:2.

The comparatively high Te signal on the annealed 4, 8, and 12 nm CdTe samples suggests that their surfaces must be Te-rich (and Cd-poor). This agrees well with the combined evidence from the Te 3d detailed spectra, the Cd:Te ratios, and the AFM images, which suggest the presence of a Te-O layer at the "Annealed" sample surfaces. The increased surface Cd signal after annealing for the 24 nm thick CdTe film is evidence that this sample varies from the structure of the thinner CdTe film samples, which correlates with the different surface morphology seen from the AFM images shown in Fig. 7.2.

To further study the annealing process from the viewpoint of the chemical environment of Zn, Fig. 7.10 (a) shows the Zn $2p_{3/2}$ and Zn $L_3M_{4,5}M_{4,5}$ spectra of the two sputter-deposited ZnO references (before and after 20 minute annealing at 525 °C), and

all "As-deposited" and "Annealed" CdTe/ZnO samples. All spectra are normalized to peak maximum, except for the Zn LMM "As-deposited" 24 nm spectrum and the Zn $2p_{3/2}$ "As-deposited" 8, 12, and 24 nm spectra, all of which do not show a prominent peak.

The Zn $2p_{3/2}$ and Zn $L_3M_{4,5}M_{4,5}$ peak energies for the two ZnO samples (~1022 and 988 eV, respectively) are in good agreement with literature values for ZnO.[17,21,25,28]

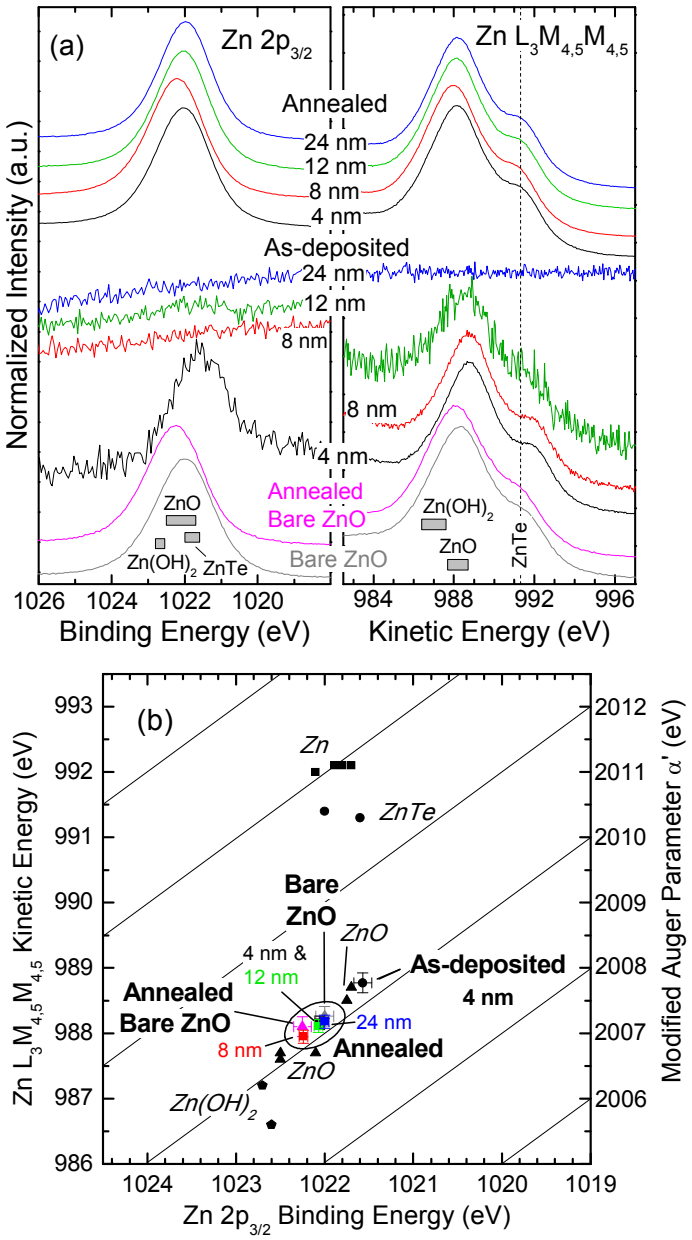

Fig. 7.10:
(a) Mg K_α-excited XPS and XAES spectra of the Zn $2p_{3/2}$ (left) and Zn $L_3M_{4,5}M_{4,5}$ (right) regions, taken on two bare ZnO references (bottom, before and after a 20 minute 525 °C annealing step), and the "As-deposited" and "Annealed" CdTe/ZnO samples (top). The range of energy positions reported for related references in literature [17, 21, 25, and 28] are indicated as grey boxes.

(b) Zn chemical state plot using the Zn $2p_{3/2}$ and Zn $L_3M_{4,5}M_{4,5}$ peak energies. Relevant references are also plotted (and labeled in italics), taken from Refs. 18, 22, 26, and 29.

The "Annealed Bare ZnO" sample peaks are shifted relative to the (non-annealed) "Bare ZnO"; 0.26 eV to higher BE (lower KE) for the 2p peak and 0.18 eV for the Auger peak. That the energy shift is not identical for both peaks suggests that this is not solely a charging or surface band-bending effect, but may also be attributable to a change in the ZnO structure, such as an annealing-induced enhanced crystallinity,[8] or a change in the chemical environment (e.g., the co-formation of $Zn(OH)_2$, see Fig. 7.11 for a detailed discussion).

The Zn $2p_{3/2}$ peak energy for the four "Annealed" CdTe/ZnO samples is in good agreement with most of the ZnO references. Similar to the Cd and Te 3d detailed spectra, the "Annealed 8 nm" sample shows a small shift towards higher BE (0.17 eV) relative to the other annealed spectra. The "As-deposited 4 nm" Zn $2p_{3/2}$ peak is at a lower BE relative to the ZnO reference peaks and closer to the literature values for ZnTe.[17,25] However, a much more dramatic shift of the $L_3M_{4,5}M_{4,5}$ spectra to a higher KE would be expected if ZnTe were present, as is displayed in the chemical state plot in Fig. 7.10 (b) (note that the shoulder at 992 eV is part of the ZnO LMM spectrum, as seen from the "Bare ZnO" spectra). The "As-deposited 4 nm" sample, the two bare ZnO samples, and all "Annealed" samples are plotted in close proximity to the ZnO literature values, showing the dominant Zn species present for all samples to be ZnO (as opposed to ZnTe or $Zn(OH)_2$).

To investigate the local chemical environment of oxygen on all sample surfaces, the normalized XPS O 1s spectra from all CdTe/ZnO layered samples are shown in Fig. 7.11, along with the "Annealed Bare ZnO" sample.

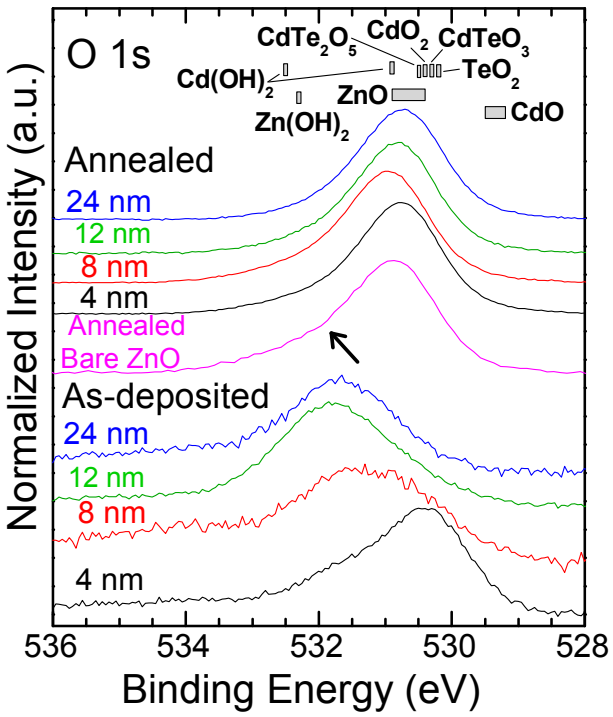

Fig. 7.11: XPS Mg K_α O 1s spectra from all "As-Deposited" and "Annealed" samples, as well as the "Annealed Bare ZnO" sample. Literature values of selected oxygen-containing compounds are represented by grey boxes and were taken from Refs. 22, 29, 30, and 31.

The "As-deposited" spectra show a low O 1s intensity from all samples prior to normalization (as shown in Fig. 7.1). The O 1s peak is at a higher BE for the thicker "As-deposited" samples relative to the "Annealed" samples due to a reduction in the signal coming from the ZnO substrate (at ~530 to 531 eV[21,28,29]) and a resulting spectral dominance of the surface-adsorbed oxides and hydroxides (at ~532 eV[30]). The O 1s peak for all "Annealed" samples is at a BE of ~530.8 eV, in good agreement with both the ZnO reference values and the O 1s of the "Annealed Bare ZnO" sample. Small shifts in the overall peak position are present in the "Annealed" spectra, comparable to those seen for the Zn 2p and LMM peaks (most prominent for the "Annealed 8 nm" sample).

The O 1s spectrum of the “Annealed Bare ZnO" sample shows an overall peak broadening relative to the annealed CdTe/ZnO samples, and added weight to *higher* BE (indicated by the arrow in Fig. 7.11). This shoulder to higher BE is also present in the “Annealed” CdTe/ZnO samples, but is less prominent and decreases with increasing original CdTe layer thickness. This shoulder is tentatively attributed to the presence of $Zn(OH)_2$ bonds, which has been shown previously to occur at ZnO surfaces and to degrade readily into ZnO and H_2O with heat and/or photon irradiation.[29,31,32]

7.4 Conclusion

We have used a combination of photoelectron spectroscopy, energy-dispersive x-ray analysis, and atomic force microscopy to investigate sputter-deposited CdTe/ZnO thin-films of varying CdTe thickness (4 to 24 nm) before and after annealing at 525 °C. We find a strong reduction in Cd and Te signal after annealing and an increase in Zn and O signals. These changes are correlated with a modification of the surface morphology, namely the formation of Cd- and Te-rich islands on the surface and an exposure of the underlying ZnO after annealing. Detailed investigation of the 3d photoemission peaks and the MNN Auger transitions of Te and Cd show these elements to be in a mixed CdTe and oxidized chemical environment, with the majority species being that of an oxide. Other changes present are attributed to photoemission final state effects due to the nano-scale grain sizes. Investigation of the Zn 2p and Zn LMM transitions indicates the absence of Zn-Te bonds, while the presence of $Zn(OH)_2$ at the surface of the bare ZnO reference samples and a similar, but reduced, hydroxide signal on the annealed CdTe/ZnO samples is seen from investigation of the oxygen photoemission spectra.

Control of the interface between an active semiconductor and a transparent conductive oxide contact is of significant importance for nanocomposite systems, since charge transfer through this interface is a vital parameter. The formation of a barrier, such as the here-found Te-O-rich surface layer, can have a profound impact on the charge carrier dynamics and energies in the semiconductor nanoparticles. While the samples prepared and studied here are not identical to the nanocomposite system in that the CdTe is not embedded within the wide band gap matrix, we show the potential for oxide formation at the CdTe/ZnO interface after annealing, and hence such intermediate layers need to be taken into account for future optimization approaches of nanocomposite devices.

7.5 References

(1) Horsley, K.; Beal, R. J.; Wilks, R. G.; Blum, M.; Häming, M.; Hanks, D. A.; Weir, M. G.; Hofmann, T.; Weinhardt, L.; Bär, M.; Potter, B. G.; Heske, C. *J. Appl. Phys.* **2014**, *116*, 024312.

(2) Shih, G. H.; Allen, C. G.; Potter Jr., B. G. *Nanotechnology* **2012**, *23*, 075203.

(3) Chatterjee, S.; Goyal, A.; Shah, S. I. *Mater. Lett.* **2006**, *60*, 3541–3543.

(4) Leschkies, K. S.; Divakar, R.; Basu, J.; Enache-Pommer, E.; Boercker, J. E.; Carter, C. B.; Kortshagen, U. R.; Norris, D. J.; Aydil, E. S. *Nano Lett.* **2007**, *7*, 1793–1798.

(5) Uhrenfeldt, C.; Chevallier, J.; Larsen, A. N.; Nielsen, B. B. *J. Appl. Phys.* **2011**, *109*, 094314.

(6) Aga Jr., R. S.; Jowhar, D.; Ueda, A.; Pan, Z.; Collins, W. E.; Mu, R.; Singer, K. D.; Shen, J. *Appl. Phys. Lett.* **2007**, *91*, 232108.

(7) Aga Jr., R. S.; Jowhar, D.; Ewan, M.; Steigerwald, A.; Ueda, A.; Pan, Z.; Collins, W. E.; Mu, R. *J. Phys. Condens. Matter* **2008**, *20*, 385206.

(8) Potter Jr., B. G.; Beal, R. J.; Allen, C. G. *J. Appl. Phys.* **2012**, *111*, 034305.

(9) Beal, R. J.; Kana, J. B.; Potter Jr., B. G. *Appl. Phys. Lett.* **2012**, *101*, 031102.

(10) Okumu, J.; Dahmen, C.; Sprafke, A. N.; Luysberg, M.; Plessen, G. von; Wuttig, M. *J. Appl. Phys.* **2005**, *97*, 094305.

(11) Zuo, J. *Appl. Surf. Sci.* **2010**, *256*, 7096–7101.

(12) Shih, G. H.; Allen, C. G.; Potter Jr., B. G. *Sol. Energy Mater. Sol. Cells* **2010**, *94*, 797–802.

(13) Allen, C. G.; Shih, G. H.; Potter Jr., B. G. *Mater. Sci. Eng. B* **2010**, *175*, 150–158.

(14) Powell, C. J.; Jablonski, A. *NIST Electron Effective-Attenuation-Length Database, Version 1.3, SRD 82*; National Institute of Standards and Technology: Gaithersburg, MD, 2011.

(15) Bearden, J. A. *Rev. Mod. Phys.* **1967**, *39*, 78–124.

(16) Peters, S.; Peredkov, S.; Neeb, M.; Eberhardt, W.; Al-Hada, M. *Phys. Chem. Chem. Phys.* **2013**, *15*, 9575–9580.

(17) Wagner, C. D. In *Practical Surface Analysis*; Briggs, D.; Seah, M. P., Eds.; John Wiley & Sons, Ltd, 1990; Vol. 1: Auger and X-ray Photoelectron Spectroscopy, pp. 595–634.

(18) Pookpanratana, S.; Khan, F.; Zhang, Y.; Heske, C.; Weinhardt, L.; Bär, M.; Liu, X.; Paudel, N.; Compaan, A. In *2010 36th IEEE Photovoltaic Specialists Conference (PVSC)*; 2010; Vol. 36th, pp. 24–27.

(19) Christie, A. B.; Sutherland, I.; Walls, J. M. *Surf. Sci.* **1983**, *135*, 225–242.

(20) Farrow, R. F. C.; Dennis, P. N. J.; Bishop, H. E.; Smart, N. R.; Wotherspoon, J. T. M. *Thin Solid Films* **1982**, *88*, 87–92.

(21) Moulder, J. F.; Stickle, W. F.; Sobol, P. E.; Bomben, K. D. *Handbook of X-ray Photoelectron Spectroscopy*; Perkin-Elmer Corporation: Minnesota, 1992.

(22) Seah, M. P.; Dench, W. A. *Surf. Interface Anal.* **1979**, *1*.

(23) Weinhardt, L.; Gleim, T.; Fuchs, O.; Heske, C.; Umbach, E.; Bär, M.; Muffler, H.-J.; Fischer, C.-H.; Lux-Steiner, M. C.; Zubavichus, Y.; Niesen, T. P.; Karg, F. *Appl. Phys. Lett.* **2003**, *82*, 571–573.

(24) Fuggle, J. C.; Martensson, N. *J. Electron Spectrosc. Relat. Phenom.* **1980**, *21*, 275–281.

(25) Wagner, C. D.; Gale, L. H.; Raymond, R. H. *Anal. Chem.* **1979**, *51*, 466–482.

(26) Moretti, G. *Surf. Sci.* **2013**, *618*, 3–11.

(27) Ramírez-Bon, R.; Espinoza-Beltrán, F. J.; Arizpe-Chávez, H.; Zelaya-Angel, O.; Sánchez-Sinencio, F. *J. Appl. Phys.* **1996**, *79*, 7682–7687.

(28) Deroubaix, G.; Marcus, P. *Surf. Interface Anal.* **1992**, *18*, 39–46.

(29) Weinhardt, L.; Bär, M.; Muffler, H.-J.; Fischer, C.-H.; Lux-Steiner, M. C.; Niesen, T. P.; Karg, F.; Gleim, T.; Heske, C.; Umbach, E. *Thin Solid Films* **2003**, *431-432*, 272–276.

(30) NIST X-ray Photoelectron Spectroscopy (XPS) Database, Version 4.1 http://srdata.nist.gov/xps/ (accessed Mar 5, 2014).

(31) Reichardt, J.; Bär, M.; Grimm, A.; Kotschau, I.; Lauermann, I.; Sokoll, S.; Lux-Steiner, M. C.; Fischer, C.-H.; Heske, C.; Weinhardt, L.; Fuchs, O.; Jung, C.; Gudat, W.; Niesen, T. P.; Karg, F. *Appl. Phys. Lett.* **2005**, *86*.

(32) Bär, M.; Reichardt, J.; Grimm, A.; Kotschau, I.; Lauermann, I.; Rahne, K.; Sokoll, S.; Lux-Steiner, M. C.; Fischer, C.-H.; Weinhardt, L.; Umbach, E.; Heske, C.; Jung, C.; Niesen, T. P.; Visbeck, S. *J. Appl. Phys.* **2005**, *98*.

CHAPTER 8

SUMMARY AND FUTURE WORK

The chalcogenides $Cu(In,Ga)Se_2$ and CdTe are of interest for use in optoelectronic devices such as LEDs and solar cells. In these applications, the chemical structure and electronic properties of the interfaces these materials form, and as such the surfaces of these materials, are of great import to the success of the final device. A variety of spectroscopic (laboratory- and synchrotron-based) and microscopic techniques were utilized in this dissertation to learn about these chalcogenide-based materials, with the goal of improving the understanding of the chemical and electronic properties of the surfaces and interfaces formed by these compounds, and ultimately improving device properties such as power conversion efficiency.

Chapters 4 and 5 investigated $Cu(In,Ga)Se_2$-based absorbers used for application in photovoltaics. In Chapter 4, a CIGSe absorber and CdS/CIGSe stack, taken from the Nanosolar roll-to-roll, ambient-pressure production line, were studied. X-ray Photoelectron Spectroscopy (XPS) showed a low level of Cu and In oxidation, and a strong Na signal at the bare absorber surface. From the CdS/CIGSe stack, evidence for possible S/Se intermixing at the CdS/CIGSe interface was seen. Ultra-violet Photoelectron Spectroscopy (UPS) and Inverse Photoemission Spectroscopy (IPES) were taken from both samples as well, and showed surface band gaps similar to other high-efficiency absorber and buffer layers deposited by more conventional methods (i.e., in vacuum, and on non-flexible substrates). Overall, a surprising low level of contamination

and strong comparisons with traditionally deposited, high efficiency CIGSe absorbers and CdS buffer layers was demonstrated.

Chapter 5 presented an in-depth study of a novel $CuInSe_2$ absorber grown at the University of Luxembourg. Here, the CISe sample was grown with a Cu-rich bulk stoichiometry, followed by a KCN etch to remove metallic $Cu_{2-x}Se$ phase at the surface, and a final, short deposition of In and Se to produce a Cu-poor surface. Comparison to a Cu-rich sample and a standard Cu-poor sample (grown similar to the NREL 3-stage process) showed the novel sample surface to be the most Cu-deficient. Despite having a significantly lower surface Cu/In ratio of 0.11 ± 0.05, as determined from XPS, the surface band gap of the novel absorber (1.48 ± 0.15 eV) was similar to that of the standard Cu-poor sample (1.54 ± 0.15 eV), and matched well to previously studied, high-efficiency CISe absorbers. Further investigation of the novel sample using Hard X-ray Photoelectron Spectroscopy (HAXPES) and X-ray Emission Spectroscopy (XES) found that the sample continued to be Cu-deficient relative to both the Cu-poor and Cu-rich reference samples, even as the surface sensitivity of the measurement technique decreased. The near-surface bulk band gap determined from XES and X-ray Absorption Spectroscopy (XAS) gave comparable values, near 1.05 ± 0.20 eV, for all three samples. The lack of variation between the samples suggests that all samples achieve equivalent near-surface bulk band gaps. Thus, while the chemical composition of the novel absorber varied from both reference samples, the electronic structure at the surface and near-surface bulk closely mimics that of traditional-grown Cu-poor absorbers, by which the highest efficiencies are achieved. Due especially to the success thus far with this novel absorber, further investigation is warranted. For example, optical band gap information

and a study of the band alignment at the CISe/Mo interface would complete the band alignment picture of the full novel CISe absorber, similar to what has been done for CIGSe and CIGSSe.[1,2]

Chapter 6 and 7 detailed studies involving CdTe-based materials. Chapter 6 looked at the metal/CdTe back contact in (Au/Cu)/CdTe/CdS solar cell stacks after rapid thermal degradation, with the goal of better understanding the decreased efficiencies seen over time in CdTe-based solar cells, and the role of elements such as Cu and O at this interface. XPS showed a strong Cu signal at the surface of all samples, regardless of the sample treatment, which suggests an alloying of Cu with Au in the back contact, or the presence of pin-holes in the final Au layer. A small S signal was also present in the XPS spectra, suggesting the migration of S from the CdS layer into the CdTe layer and to the Au/Cu back contact, with and without stress treatment. XES of the S $L_{2,3}$ and Cl $L_{2,3}$ emission edges showed a correlation between the presence of Au- and Cu-S bonds and a lack of air exposure, and evidence for Cu-Cl bonds for samples stressed under illumination. This showed that S and Cl are present at the back contact/CdTe interface and active in forming bonds with the back contact metals used, somewhat dependently of the stress treatment and environment. While Cu, O, and Cl have been suggested to play a role in the degradation of this interface previously,[3] it is feasible from the results shown here that Cl and also S may be involved in the degradation process. Further study, perhaps involving the direct investigation with XES of the Cu and Au bonding environment at the back contact/CdTe interface, could further clarify the bonds they are participating in. Comparing the bonding environments seen and the solar cell efficiencies

achieved after various stress treatments would also help to identify their role in degradation.

The CdTe/ZnO interface, as seen in nanocomposite materials, was studied in detail using a combination of spectroscopic and microscopic techniques, and was presented in Chapter 7. In previous work on layered CdTe/ZnO nanocomposite films, annealing produced an increase in crystallinity with no change to the absorption edge. It was the goal of this study to focus on the effects of annealing on the chemistry and structure of the CdTe/ZnO interface more specifically. Thin films of CdTe (4 to 24 nm) were sputter deposited onto 100 nm ZnO/Si substrates, and sibling samples of each thickness were annealed at 525 °C for 20 minutes. Comparison of the "As-deposited" and "Annealed" samples with XPS showed a strong reduction in Cd and Te signal intensity, and increase in Zn and O signal intensity after the annealing treatment. Investigation with AFM, SEM, and EDX revealed the presence of Cd- and Te-rich islands on the sample surface, and an exposure of the underlying ZnO. The chemical environment of Cd and Te remaining on the "Annealed" sample was analyzed through the XPS detailed spectra of the 3d photoemission peaks and MNN Auger transitions. Fitting the spectra and plotting the energies on a modified Auger parameter plot showed the majority of the Cd and Te to be in an oxidized environment after annealing, with some CdTe-like bonding remaining. A shift of the data points in the modified auger parameter plot was also seen, suggesting final-state effects due to the nano-scale grain sizes. The results overall showed a breaking up of the CdTe layer with annealing, and the possibility of an oxide barrier forming between the wide band gap ZnO matrix and the CdTe nanoparticles, which

would have a large impact on the charge carrier dynamics and final properties for this nanocomposite material.

8.1 References

(1) Bär, M.; Nishiwaki, S.; Weinhardt, L.; Pookpanratana, S.; Fuchs, O.; Blum, M.; Yang, W.; Denlinger, J. D.; Shafarman, W. N.; Heske, C. *Appl. Phys. Lett.* **2008**, *93*, 244103.

(2) Bär, M.; Nishiwaki, S.; Weinhardt, L.; Pookpanratana, S.; Shafarman, W. N.; Heske, C. *Appl. Phys. Lett.* **2008**, *93*, 042110.

(3) Visoly-Fisher, I.; Dobson, K. D.; Nair, J.; Bezalel, E.; Hodes, G.; Cahen, D. *Adv. Funct. Mater.* **2003**, *13*, 289–299.

APPENDIX

LIST OF ABBREVIATIONS AND SYMBOLS

α'	Modified Auger Parameter
AFM	Atomic Force Microscopy
ALS	Advanced Light Source
AM 1.5	Air-mass 1.5
BE	binding energy
CB	conduction band
CBM	conduction band maximum
CdS	Cadmium Sulfide
CdTe	Cadmium Telluride
CIGSe	$Cu(In_{1-x}Ga_x)Se_2$
CISe	$CuInSe_2$
DAAD RISE	Deutscher Akademischer Austausch Dienst (German Academic Exchange Service) Research Internships in Science and Engineering
DI	de-ionized
EDX	Energy Dispersive X-ray Spectroscopy
E_F	Fermi level
E_g	band gap
E_{vac}	vacuum level
FAT	Fixed Analyzer Transmission
FTO	Fluorine-doped Tin Oxide
FWHM	full width at half maximum

HAXPES	Hard X-ray Photoelectron Spectroscopy
hν	photon energy
HV	high vacuum
HZB	Helmholtz-Zentrum Berlin für Materialien und Energie, GmbH
IMFP	Inelastic Mean Free Path
IPES	Inverse Photoemission Spectroscopy
KE	kinetic energy
LED	light-emitting diode
NREL	National Renewable Energy Laboratory
ODC	ordered defect chalcopyrite
PE	Pass Energy
PV	photovoltaic
PVD	Physical Vapor Deposition
SEM	Scanning Electron Microscopy
UHV	Ultra-high Vacuum
UPS	Ultra-violet Photoelectron Spectroscopy
UT	University of Toledo
VB	valence band
VBM	valence band maximum
XAS	X-ray Absorption Spectroscopy
XES	X-ray Emission Spectroscopy
XPS	X-ray Photoelectron Spectroscopy
ZnO	Zinc Oxide

VITA

Graduate College
University of Nevada, Las Vegas

Kimberly A. Horsley

Degrees:

Bachelor of Science, Biology, 2009
Bachelor of Arts, Chemistry, 2009
University of Nevada, Las Vegas

Honors and Awards:

1. Southern Nevada ACS poster contest, 2nd place – 2013
2. Graduate and Professional Student Association Research Forum, 1st place – 2013
3. GPSA Conference Travel and Attendance Scholarship – 2013
4. Outstanding Graduate Student Teaching Award – 2013
5. DAAD-RISE Professional Internship – 2011
6. NSF-EPSCoR Undergraduate Research Opportunity – 2008

Publications:

1. **K. Horsley**, R.J. Beal, R.G. Wilks, M. Blum, M. Häming, D.A. Hanks, M.G. Weir, T. Hofmann, L. Weinhardt, M. Bär, B.G. Potter, Jr., and C. Heske, "Impact of annealing on the chemical structure and morphology of the thin-film CdTe/ZnO interface", J. Appl. Phys. 116, 024312 (2014).
2. **K. Horsley**, R.G. Wilks, D. A. Hanks, S. Pookpanratana, M. Blum, W. Yang, N. Paudel, A. Compaan, M. Bar, L. Weinhardt, and C. Heske, Proceedings 38th IEEE Photovoltaic Specialists Conference (2012), Austin, TX, pp. 000400–000405.
3. D. A. Hanks, M. G. Weir, **K. Horsley**, T. Hofmann, L. Weinhardt, M. Bär, K. Barricklow, P. Kobyakov, W. Sampath, C. Heske, "Photoemission Study of CdTe Surfaces After Low-Energy Ion Treatments", Proceedings 38th IEEE Photovoltaic Specialists Conference (2012), Austin, TX, pp. 000396-000399.
4. **K. Horsley**, S. Pookpanratana, S. Krause, T. Hofmann, M. Blum, L. Weinhardt, M. Bar, K. George, J. Van Duren, D. Jackrel, and C. Heske, Proceedings 37th IEEE Photovoltaic Specialists Conference (2011), Seattle, WA, pp. 000374–000378.
5. G. Wang, Y. Ling, D.A. Wheeler, K. George, X. Yang, **K. Horsley**, C. Heske, J.Z. Zhang, and Y. Li, "Highly Photoactive a-Fe2O3 Films for Photoelectrochemical Water Splitting" Nano Letters 11, 3503 – 3509 (2011).
6. **Kimberly Horsley**, Lloyd R. Stark, and D. Nicholas McLetchie, "Does the silver moss Bryum argenteum exhibit sex-specific patterns in vegetative growth rate, asexual fitness or prezygotic reproductive investment?" Annals of Botany 107: 897-907, 2011.

Presentations:

1. **K. Horsley**, V. Depredurand, R. G. Wilks, M. G. Weir, S. L. Alexander, T. Hofmann, R. Felix, D. Gerlach, M. Blum, L. Weinhardt, M. Bär, S. Siebentritt, C. Heske, "Comparison of the Surface and Near-Surface Bulk Properties of Cu-poor and Cu-rich prepared $CuInSe_2$ Thin-Film Solar Cell Absorbers", Presented at 2013 Materials Research Society Spring Meeting and Exhibit, San Francisco, CA, April 1-5.

Posters:

1. **K. Horsley**, M. Mezher, D. Hanks, M. G. Weir, T. Hofmann, W. Yang, R. G. Wilks, M. Haeming, M. Blum, M. Baer, L. Weinhardt, K. Ramanathan, M. Contreras, R. Noufi, C. Heske, "Surface Spectroscopy for Chemical and Electronic Analysis of Thin-film Photovoltaic Materials", Presented at the 2nd DOE Thin-Film Workshop Poster Session at NREL, Golden CO, October 2013.
2. **K. Horsley**, R.G. Wilks, D. Hanks, S. Pookpanratana, M. Blum, W. Yang, N. Paudel, A. Compaan, M. Bär, L. Weinhardt, C. Heske, "Chemical Surface and Interface Properties of Differently Stressed (Au/Cu/)CdTe/CdS Thin-film Solar Cell Structures", Proceedings 38th IEEE PVSC, Austin, TX, June 3-8 2012.
3. **K. Horsley**, S. Pookpanratana, S. Krause, T. Hofmann, M. Blum, L. Weinhardt, M. Bär, K. George, J. Van Duren, D. Jackrel, C. Heske, "Electronic and Chemical Properties of Non-Vacuum Deposited Chalcopyrite Solar Cells", Proceedings, 37th IEEE PVSC, Seattle, WA, June 20-24, 2011.

Dissertation Title:

Spectroscopic Investigation of the Chemical and Electronic Properties of Chalcogenide Materials for Thin-Film Optoelectronic Devices

Dissertation Examination Committee:

Chairperson, Clemens Heske, Dr. rer. nat.
Committee Member, Kathy Robins, Ph. D.
Committee Member, Dong-Chan Lee, Ph. D.
Graduate Faculty Representative, Rama Venkat, Ph. D.